

International Journal of

# **Rotating Machinery**

Special Issue  
Industrial Compressor

Guest Editors: Ryoichi S. Amano, Abraham Engeda, Ashwani K. Gupta, Bengt Sunden,  
and Cheng Xu



---

# **Industrial Compressor**

International Journal of Rotating Machinery

---

## **Industrial Compressor**

Guest Editors: Ryoichi S. Amano, Abraham Engeda,  
Ashwani K. Gupta, Bengt Sunden, and Cheng Xu



---

Copyright © 2012 Hindawi Publishing Corporation. All rights reserved.

This is a focus issue published in “International Journal of Rotating Machinery.” All articles are open access articles distributed under the Creative Commons Attribution License, which permits unrestricted use, distribution, and reproduction in any medium, provided the original work is properly cited.

## Editorial Board

- S. Acharya, USA  
Abdollah A. Afjeh, USA  
Hyeong J. Ahn, Republic of Korea  
Ryoichi Samuel Amano, USA  
Forrest E. Ames, USA  
Luis San Andres, USA  
Jerome Antoni, France  
S. V. Apte, USA  
Hans Joerg Bauer, Germany  
Donald E. Bently, USA  
Dieter E. Bohn, Germany  
Gerard BOIS, France  
Christopher Earls Brennen, USA  
Mustafa Canakci, Turkey  
Giovanni Maria Carlomagno, Italy  
M. K. Chyu, USA  
Alessandro Corsini, Italy  
Ningsheng Feng, Australia  
David P. Fleming, USA  
Koji Fujimoto, Japan  
Luis Gato, Portugal  
Georges A. Gerolymos, France  
J Paul Gostelow, UK  
Chunill Hah, USA  
Eric J. Hahn, Australia  
Awatef Hamed, USA  
J.-C. Han, USA  
Hiroshi Hayami, Japan  
Tasawar Hayat, Pakistan  
Robert C. Hendricks, USA  
Hooshang Heshmat, USA  
Dimitrios T. Hountalas, Greece  
Zuohua Huang, China  
Norihiko Iki, Japan  
Tariq Iqbal, Canada  
Masaru Ishizuka, Japan  
Takuzo Iwatsubo, Japan  
David Japikse, USA  
Yasutomo Kaneko, Japan  
Kazuhiko Kawaike, Japan  
Funazaki Ken-ichi, Japan  
Tong Seop Kim, Republic of Korea  
Spyros A. Kinnas, USA  
R. G. Kirk, USA  
Ching-Pang Lee, USA  
Arthur W. Lees, UK  
Ricardo F. Martinez-Botas, UK  
Shigenao Maruyama, Japan  
H. Masjuki, Malaysia  
Eric Maslen, USA  
Fabian Mauss, Germany  
David U. Mba, UK  
Jiun-Jih Miau, Taiwan  
Akira Murata, Japan  
Agnes Muszynska, USA  
Vengalattore T. Nagaraj, USA  
M. Razi Nalim, USA  
E.Y.K. Ng, Singapore  
Osamu Nozaki, Japan  
Yutaka Ohta, Japan  
Takanari Okamura, Japan  
Yoji Okita, Japan  
Ion Paraschivoiu, Canada  
R. Payri, Spain  
Paolo Pennacchi, Italy  
Sergio Preidikman, USA  
Richard B. Rivir, USA  
Thomas Sattelmayer, Germany  
Jerzy T. Sawicki, USA  
Meinhard Taher Schobeiri, USA  
Enrico Sciubba, Italy  
Terrence W. Simon, USA  
ONKAR SINGH, India  
Seung Jin Song, Republic of Korea  
Toyotaka Sonoda, Japan  
Fengrui Sun, UK  
Ken-Ichiro Takeishi, Japan  
Hamid A. Toliyat, USA  
Wei Tong, USA  
Yoshinobu Tsujimoto, Japan  
Ting Wang, USA  
Toshinori Watanabe, Japan  
Bernhard Weigand, Germany  
Dave Wisler, USA  
Sigmar L. K. Wittig, Germany  
Kazuyuki Yamaguchi, Japan  
Yasuyuki Yokono, Japan  
Saburo Yuasa, Japan

# Contents

---

**Industrial Compressor**, Ryoichi S. Amano, Abraham Engeda, Ashwani K. Gupta, Bengt Sunden, and Cheng Xu

Volume 2012, Article ID 370425, 1 pages

**Meridional Considerations of the Centrifugal Compressor Development**, C. Xu and R. S. Amano

Volume 2012, Article ID 518381, 11 pages

**Empirical Design Considerations for Industrial Centrifugal Compressors**, Cheng Xu and Ryoichi S. Amano

Volume 2012, Article ID 184061, 15 pages

**Performance Improvement of a Centrifugal Compressor by Passive Means**, N. Sitaram and S. M. Swamy

Volume 2012, Article ID 727259, 9 pages

**A Novel Approach to Evaluate the Benefits of Casing Treatment in Axial Compressors**, Guillaume Legras, Isabelle Trbinjac, Nicolas Gourdain, Xavier Ottavy, and Lionel Castillon

Volume 2012, Article ID 975407, 19 pages

**Reciprocating Compressor 1D Thermofluid Dynamic Simulation: Problems and Comparison with Experimental Data**, A. Gimelli, A. Rapicano, F. Barba, and O. Pennacchia

Volume 2012, Article ID 564275, 13 pages

## Editorial

# Industrial Compressor

**Ryoichi S. Amano,<sup>1</sup> Abraham Engeda,<sup>2</sup> Ashwani K. Gupta,<sup>3</sup> Bengt Sunden,<sup>4</sup> and Cheng Xu<sup>5</sup>**

<sup>1</sup> Department of Mechanical Engineering, University of Wisconsin, Milwaukee, WI 53201, USA

<sup>2</sup> Department of Mechanical Engineering, Michigan State University, East Lansing, MI 53201, USA

<sup>3</sup> Department of Mechanical Engineering, University of Maryland, College Park, MD 20742, USA

<sup>4</sup> Department of Energy Sciences, Lund University, Lund, Sweden

<sup>5</sup> GE Aviation, Cincinnati, OH, USA

Correspondence should be addressed to Ryoichi S. Amano, amano@uwm.edu

Received 13 September 2012; Accepted 13 September 2012

Copyright © 2012 Ryoichi S. Amano et al. This is an open access article distributed under the Creative Commons Attribution License, which permits unrestricted use, distribution, and reproduction in any medium, provided the original work is properly cited.

This issue consists of five papers that deal with comprehensive studies on research and development of industrial compressors. Contributed papers deal with compressors used for low- and medium-pressure services in ethylene plants, lube oil plants, refineries, refrigeration, and air compression, as well as those used for high-pressure services, such as those used in ammonia, urea, and methanol synthesis, refinery recycle, and natural gas compression and injection. Some also deal with pipeline compressors that are of low- and medium-pressure ratios used in wide range of applications, while other compressors are used in recycle services such as those used in methanol plants, ethylene oxide plants.

Papers presented this special issue cover topics extending from design experience to detailed design feature studies and include cover broad range of compressors: axial compressor, centrifugal compressor, and reciprocating compressor. There are many interesting topics and studies. It is expected that the knowledge and experiences presented in both academic and industrial readers will benefit from this special issue.

The papers included here are: “A novel approach to evaluate the benefits of casing treatment in axial compressors” by G. Legras et al., “Performance improvement of a centrifugal compressor by passive means” by N. Sitaram and S. M. Swanmy, “Meridional considerations of the centrifugal compressor development” by C. Xu and R. S. Amano, “Reciprocating compressor 1D thermofluid dynamic simulation: problems and comparison with experimental data” by A. Gimelli et al., and “Empirical design considerations for industrial centrifugal compressors” by C. Xu and R. S. Amano. It is expected that the information provided here on the specific types

of compressors will provide useful information to wide readership from academia and industry.

Ryoichi S. Amano  
Abraham Engeda  
Ashwani K. Gupta  
Bengt Sunden  
Cheng Xu

## Research Article

# Meridional Considerations of the Centrifugal Compressor Development

**C. Xu and R. S. Amano**

*Department of Mechanical Engineering, University of Wisconsin, Milwaukee, WI 53211, USA*

Correspondence should be addressed to R. S. Amano, amano@uwm.edu

Received 29 January 2012; Accepted 4 September 2012

Academic Editor: A. Engeda

Copyright © 2012 C. Xu and R. S. Amano. This is an open access article distributed under the Creative Commons Attribution License, which permits unrestricted use, distribution, and reproduction in any medium, provided the original work is properly cited.

Centrifugal compressor developments are interested in using optimization procedures that enable compressor high efficiency and wide operating ranges. Recently, high pressure ratio and efficiency of the centrifugal compressors require impeller design to pay attention to both the blade angle distribution and the meridional profile. The geometry of the blades and the meridional profile are very important contributions of compressor performance and structure reliability. This paper presents some recent studies of meridional impacts of the compressor. Studies indicated that the meridional profiles of the impeller impact the overall compressor efficiency and pressure ratio at the same rotational speed. Proper meridional profiles can improve the compressor efficiency and increase the overall pressure ratio at the same blade back curvature.

## 1. Introduction

High single-stage pressure ratio and high performance are greatly desired in the design of the centrifugal compressors. High boost pressure of aircraft engine and diesel engines, and equipment cost in the oil and gas fields require high pressure ratio and improved thermal efficiency single-stage centrifugal compressors. The manufacturers of marine turbochargers also have been competing for the development of high pressure compressors. The demands for a high pressure ratio for centrifugal compressors need special consideration during the compressor design. If the centrifugal single-stage compressor ratio is over 4.5, the flow of the impeller exit normally has a supersonic zone. This makes the high pressure ratio centrifugal compressor design very challengeable.

The centrifugal compressor design has been an active research field for many years [1–4]. Unlike axial compressors, gas enters a centrifugal compressor axially and then turns in the radial direction out from the impeller with the action of the centrifugal force. The gas then is directed to a radial annular vane or vaneless diffuser and finally moves into a volute or collector to deliver the compressed gas to the next stage or send it to the next components [1–7]. Unlike an axial compressor or fan [8], the work input for a centrifugal

compressor is almost independent of the nature of the flow. A centrifugal compressor can be designed with much higher De Haller number than an axial compressor can achieve. Therefore, it is possible for a centrifugal compressor to have a much higher stage pressure ratio than an axial one. In addition, centrifugal compressors show very reasonable performance at low flow gas compression.

The development of computer technologies and advancements in turbomachinery technology have made optimizing the centrifugal compressor design possible and easier than ever before. Turbomachinery design normally starts with a mean line program at each individual operating point on a map and then through-flow calculation is performed; finally, the impeller, diffuser, and volute are designed. It is also important to optimize off-design performance.

Recently, multidiscipline optimizations have drawn more attention. Due to the complications of the engineering system and of multidisciplines, it is still challenging. He and Wang [9] developed a process for an adjoined approach to concurrent blading aerodynamic and aero-elastic design optimizations at earlier stages of the design process. A non-linear harmonic phase solution method is adopted to solve the unsteady Reynolds-averaged Navier-Stokes (RANS)

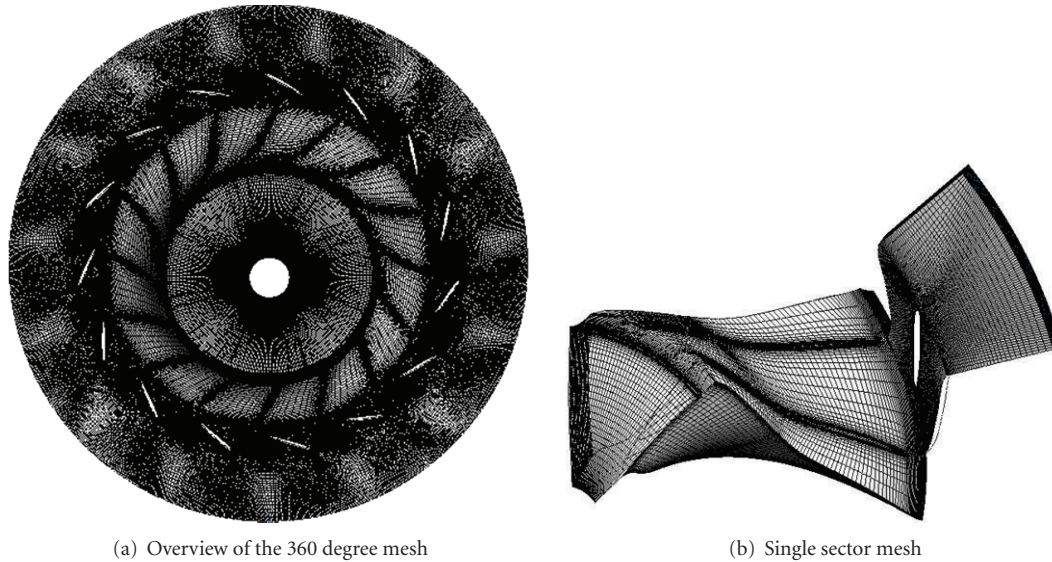


FIGURE 1: Calculation meshes.

equations to enhanced interactions between the blades and the surrounding working fluid. Thus, a blade flutter stability and forced response are possible to obtain. Ghisu et al. [10] recently developed a system for the integrated design optimization of gas turbine engines; postponing the setting of the interface constraints to a point facilitates better exploration of the available design space and better exploitation of the tradeoffs between different disciplines and modules. Verstraete et al. [11] developed a multidisciplinary optimization system and used it to design a small radial compressor impeller. The method only discussed the aerodynamic performance and stress interactions. However, the impeller reliability not only relied on the stress but also on the vibrations, that is, low-cycle fatigue (LCF) and high-cycle fatigue (HCF).

In this study, a recently developed turbomachinery viscous aerodynamic and structure optimal method [4, 12–18] was used to fully optimize a centrifugal compressor design. The main focus of this study lies in emphasizing the importance of the meridional shape related to a centrifugal compressor aerodynamic performance. The designs reported here all met the structure requirements for different meridional shapes. The results showed that the meridional shape is very important for obtaining an optimized impeller design.

To demonstrate the meridional impacts on the compressor performance, a compressor with an inlet flow of  $34 \text{ Nm}^3/\text{min}$  was used in analyses. The design point is with the conditions of the polytropic head and the flow coefficients of  $\varphi = 0.68$ , and  $\phi = 0.195$ , respectively. The design total pressure ratio is about 4.45. The impeller inducer average Mach number is about 0.85 and the average exit Mach number is about 1.08. Therefore, the compressor has a significant supersonic range. The design considered a transonic range and efforts to reduce the shock loss. The diffuser vane was designed by few patent features and was not changed during the impeller optimization [19].

The compressor design employs the present design process that includes a viscous aerodynamic design and structure optimization for achieving efficiency and stability targets. The compressor developed in this study consists of three major parts: an impeller, a low solidity diffuser, and a volute. In this study, particular attention was paid to the impeller meridional design to illustrate the importance.

## 2. CFD Calculations and Validations

The commercial computational fluid dynamics (CFD) code ANSYS CFX-11.0 [20] was used for the calculations. The mesh independent studies found out that the mesh sizes as shown in Figures 1 and 2 were sufficient to keep the identical performance even as the mesh continued to refine. The calculation nodes for the 360 degree wheel are about 2 million and the diffuser nodes are about 6 million. The single sector wheel nodes are about 250 k and the diffuser is about 400 k. The mesh near wall has been set as the  $y^+$  value smaller than 2.5. The fluid models use ideal gas and heat transfer calculations with total energy to include the viscous work term in the heat transfer calculation, along with the  $k-\epsilon$  turbulence model. An existing compressor stage was calculated and compared with the test results to validate the CFD process and the mesh independent status [21]. The mesh structures are shown in Figures 1 and 2. Three different calculations were performed, that is, 360 degree mixing plane vane and rotor interface, 360 degree frozen rotor vane and rotor interface, and single sector frozen rotor vane and rotor interface. The test runs for the frozen rotor interface showed that the vane and wheel blade relative location affects the calculated performance results. Several different rotor and vane locations were run for a single slide of the rotor and the vane. We found that the relative location between the vane and the wheel blade, as shown in Figure 1(b), provided the performance results most close to the experiments. It

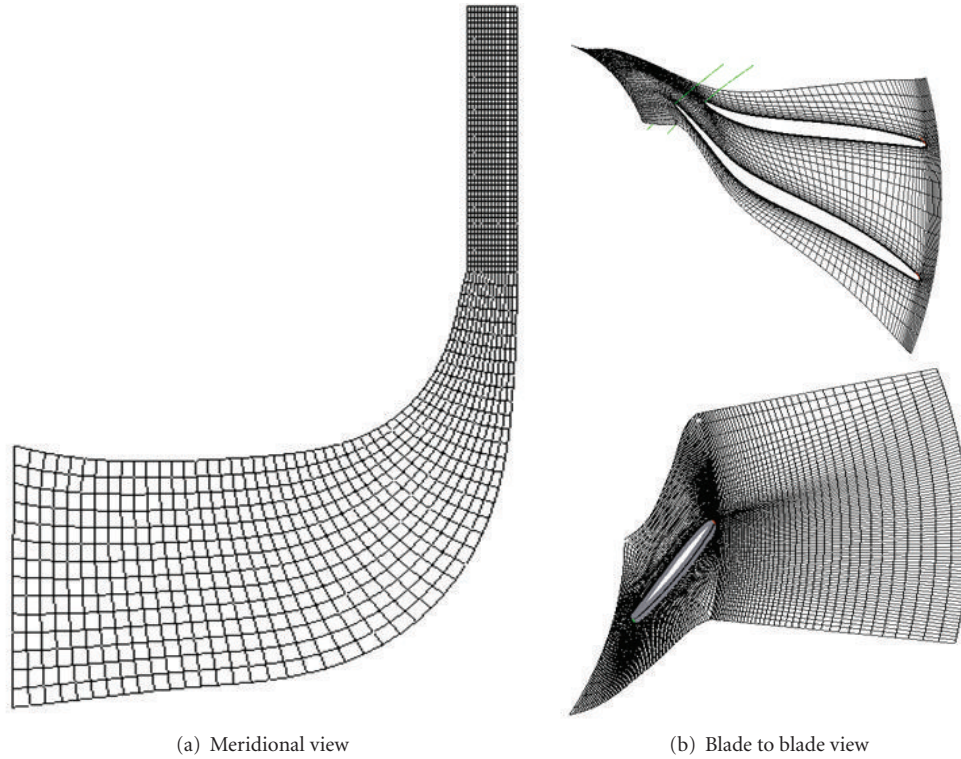


FIGURE 2: Mesh in meridional view and blade to blade view.

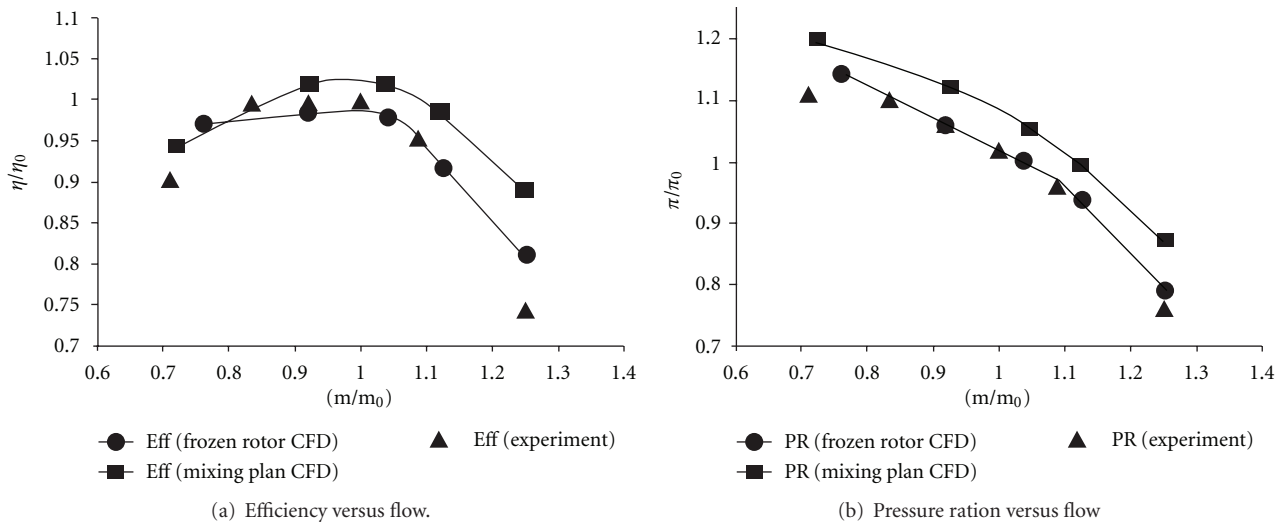


FIGURE 3: Computational results compared with experiments.

is implied that the frozen rotor calculation from this wheel and vane location is close to the unsteady time average results. During the calculations, we found that the calculated performance results were almost identical for the 360 degree frozen rotor compared with the single sector frozen rotor vane, as shown in Figure 1(b). The CFD results with volute loss corrections are shown in Figure 3, where it is clearly

shown that both the frozen rotor and the mixing plane calculations provided a good indication of experiments. The frozen rotor with a single sector of the blade and vane provided the results very close to the experiments. All the analyses in the study of meridional shape impacting the performance were performed with the single sector with a frozen rotor interface.

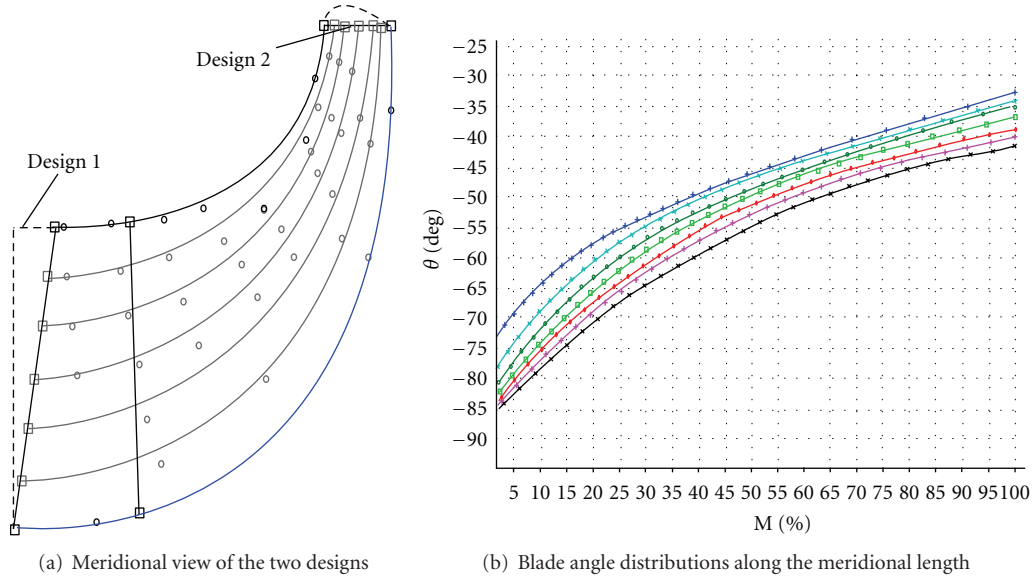


FIGURE 4: Geometry of Design 1 and Design 2.

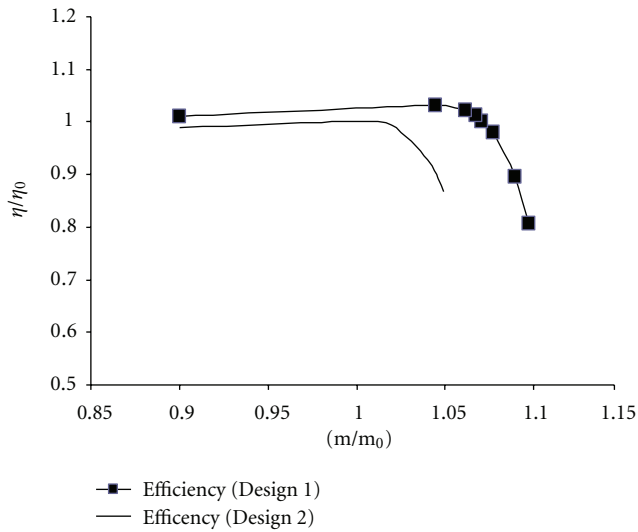


FIGURE 5: Calculated performance curve.

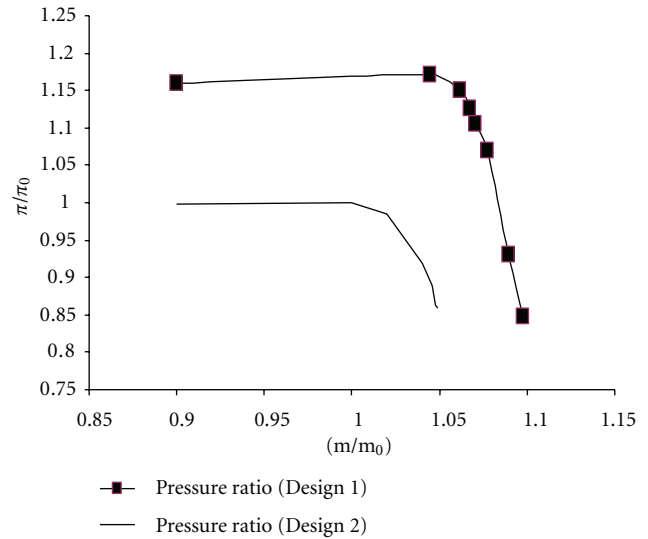


FIGURE 6: Calculated pressure ratio.

### 3. Results and Discussion

In this study, the focus is to study the meridional shape impact on the centrifugal compressor performance. During the study, the impeller blade angle changes with the percentage of the meridional distance being maintained the same, while the meridional shape was changed, as shown in Figure 4. The vane design was kept the same for both Design 1 and Design 2 to demonstrate the impeller impact on the overall stage performance. Figure 4(a) highlighted the difference between the two meridional shapes. Design 1 is a newly proposed meridional shape with a vertical inlet and an exit with a clipped, smooth-curved shape. Design 2 is the traditional meridional design with an inlet tip cut back and a flat discharge. Figure 4(b) shows the blade angle  $\beta$  distribution along the nondimensional meridional length.

Both designs have the identical  $\beta$  distributions. During the calculations, a similar mesh size was used for all the studies as presented in the previous section to ensure that the results were mesh-independent.

Calculations indicated that Design 1 had a relative higher efficiency and wider operating range, as shown in Figure 5. This is because the shroud section has a more general distribution of the blade loading. Also, both the shroud and the hub side have a similar pressure raise along the meridional direction, which reduced the flow mixing loss between the shroud and the hub at the impeller exist. The design intention was to make a uniform distribution of the impeller exit static pressure. The analysis also indicates that, Design 1 has a higher pressure ratio compared with Design 2, as shown in Figure 6. Design 1 shows about a 15% higher

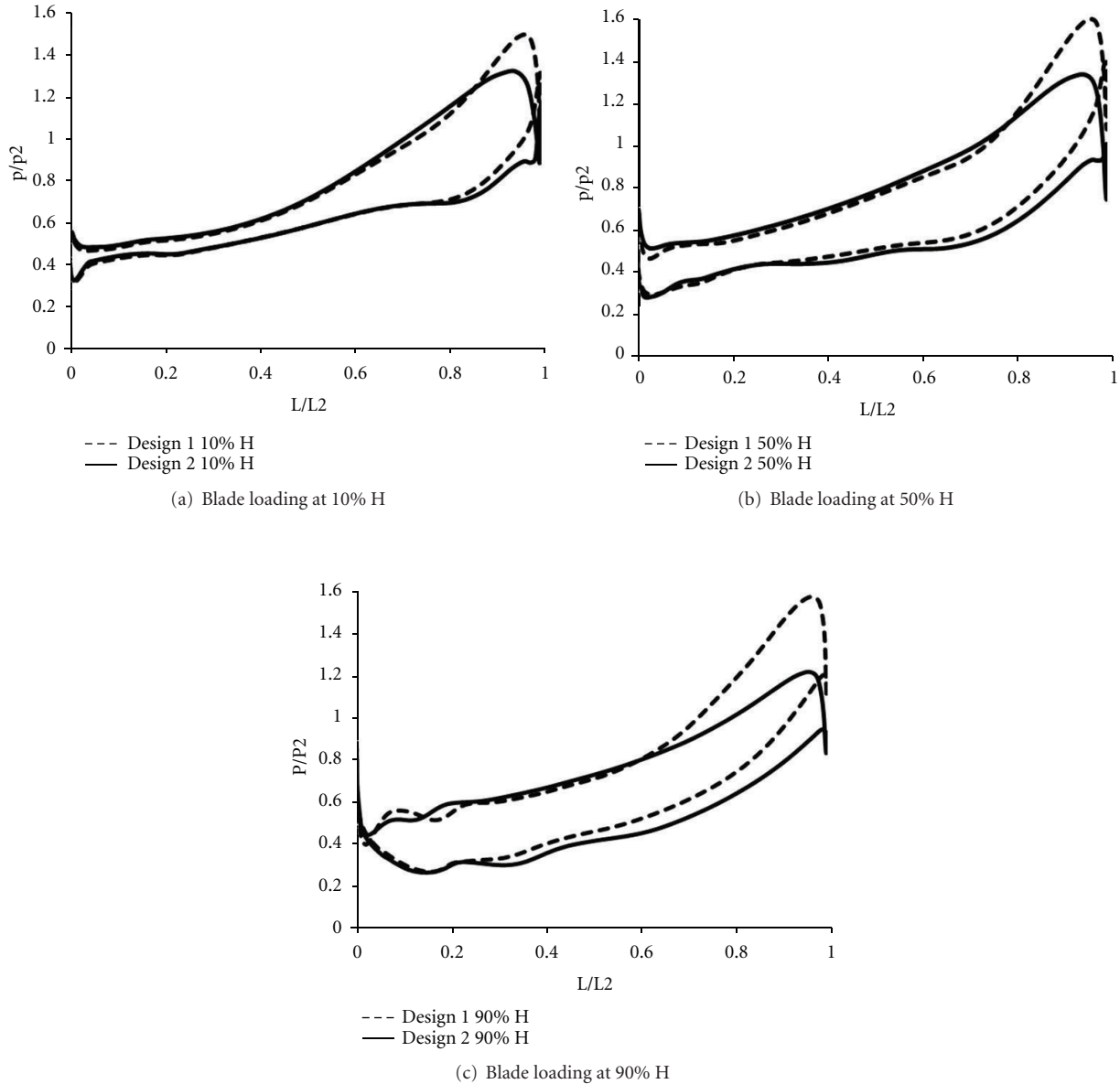


FIGURE 7: Blade loading at different blade height locations.

pressure ratio compared with Design 2. This is because in Design 1 the exit shroud has a larger diameter. The increase of the exit diameter raises the pressure ratio. The increase of the shroud impeller exit diameter also increases the overall flow capacity, as shown in both Figures 5 and 6. However, the calculations show that the surge flow does not change too much. This is because Design 1 has a better flow control that delayed the flow separation and surge.

Figure 7 shows the blade loading ( $p/p_2$ ) distributions along different spanwise locations. For all the blade spanwise locations, Design 1 shows a higher loading than Design 2 at the impeller exit. The loading profiles indicate that the two designs have a similar loading below 80% meridional direction. For Design 1, the shroud loaded more than for Design 2. Figure 7 also shows that the shroud static pressure is close

to the hub static pressure for Design 1. However, the loading plots of Design 2 show that the shroud static pressure is lower than that for the hub side. The results indicate that the flow at the exit has a higher mixing loss.

Figure 8 shows the Mach number distributions for the impeller and the vane at different spanwise locations for both Design 1 and Design 2 near the peak efficiency flow condition. It can be seen also that the Mach number at the inlet of Design 1 is slightly higher than that for Design 2. This is because Design 1 has a higher mass flow rate at the design point. The larger inlet mass flow also increases the vaned diffuser inlet Mach number for Design 1. It can be seen that for the tip and midsections, separation zones (very low Mach number zone) are smaller for Design 1 than for Design 2. The small separation zones reduce loss and improve efficiency.

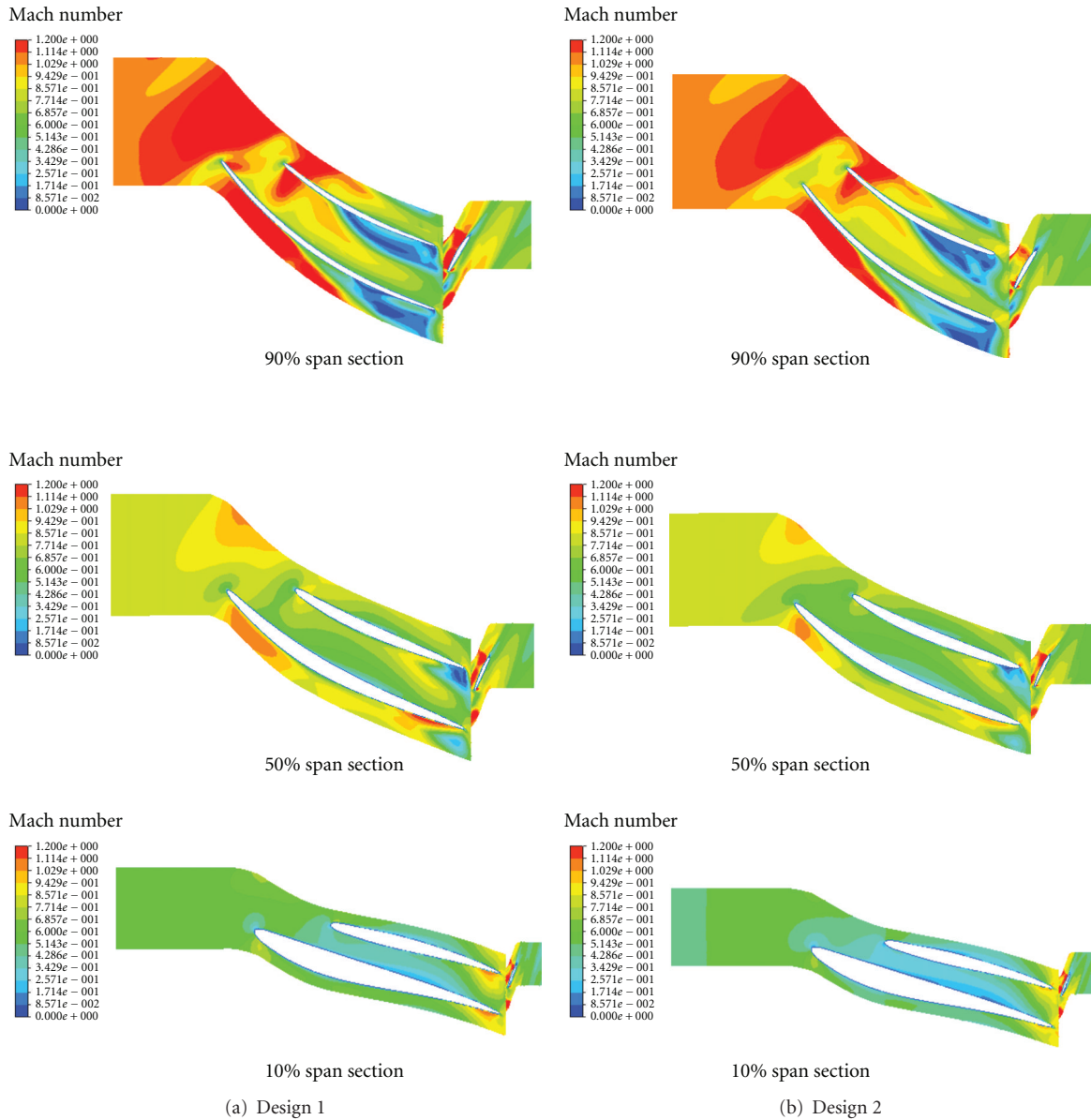


FIGURE 8: Mach number distributions near peak efficiency in blade to blade sections.

It is also shown that the incidents at different spanwise locations for Design 1 are smaller than those for Design 2.

Figure 9 shows the entropy contour plots for both Design 1 and Design 2 near the peak efficiency points at different spanwise locations. The high entropy area at the tip section for Design 1 is smaller than that in Design 2. However, the high entropy zone for the midspan and the hub section is similar for both designs. It can be seen that the meridional shape for Design 1 has improved the tip range of the flow. This is probably the main reason for the meridional design for Design 1 to improve the overall stage performance. Figure 10 shows the entropy generation inside the tip clearance for both Design 1 and Design 2. It can be seen that the entropy generation patterns are similar at the tip sections for both designs. Design 1 indicates a lower

entropy generation at the tip area than for Design 2. Design 1 can improve the tip clearance flow and has less secondary flow loss. Figure 11 shows the entropy generation along the meridional mid-plane. It can be seen that the shroud turning location has the highest entropy generations for both designs. Design 1 has lower entropy generation near the shroud tip area compared with Design 2. It can be seen that Design 1 has some advantages compared with Design 2.

Figures 12(a) and 12(b) show the Mach number distributions at a design point along the meridional plane for both designs. It can be seen that the Mach number distributions are very similar for both designs. It is shown that the flow field distributions for both designs are in a similar pattern. This is because the flow field was basically determined by the blade  $\beta$  angle distribution. However, a similar level of

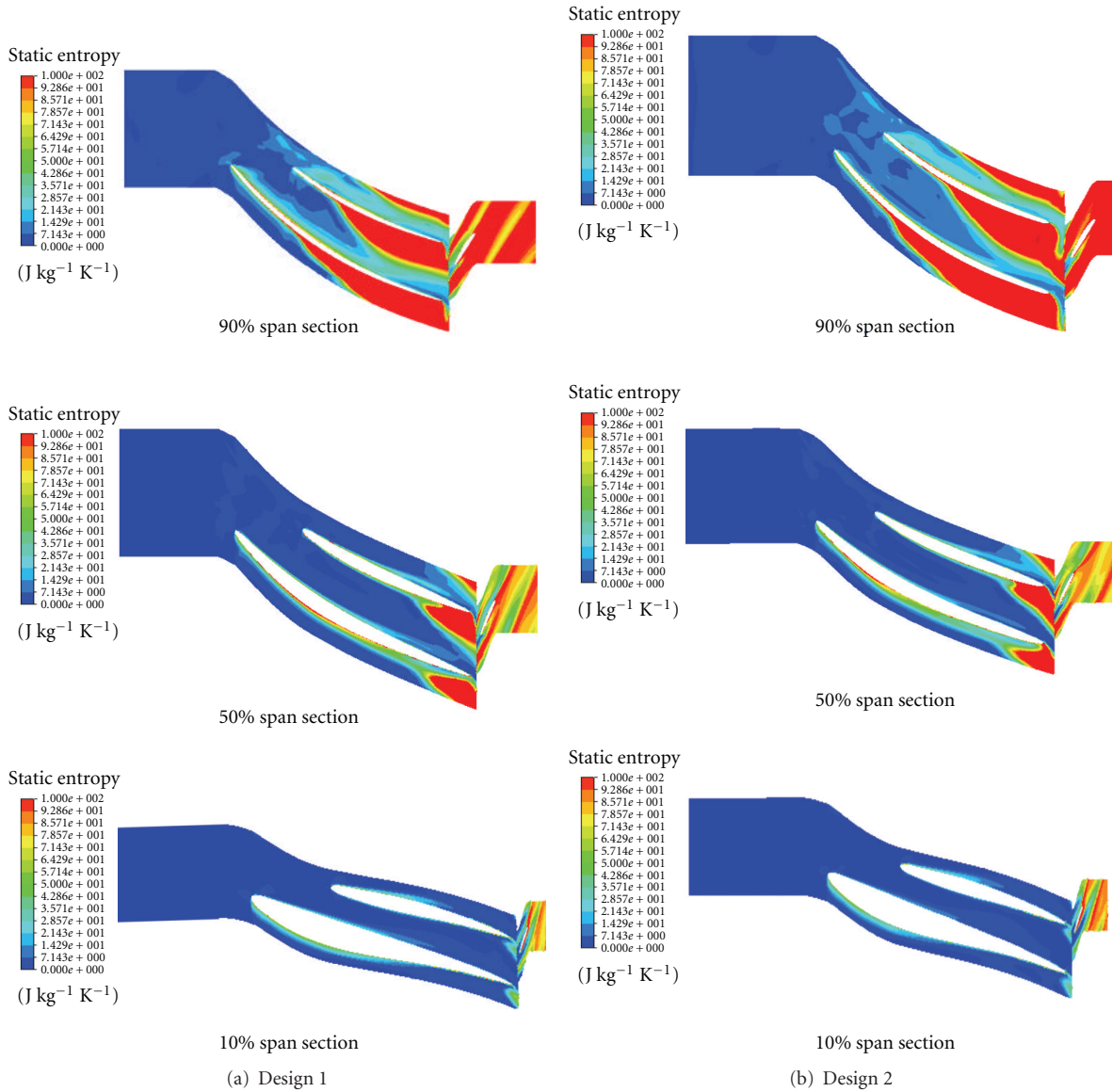


FIGURE 9: Entropy generation along the blade to blade sections.

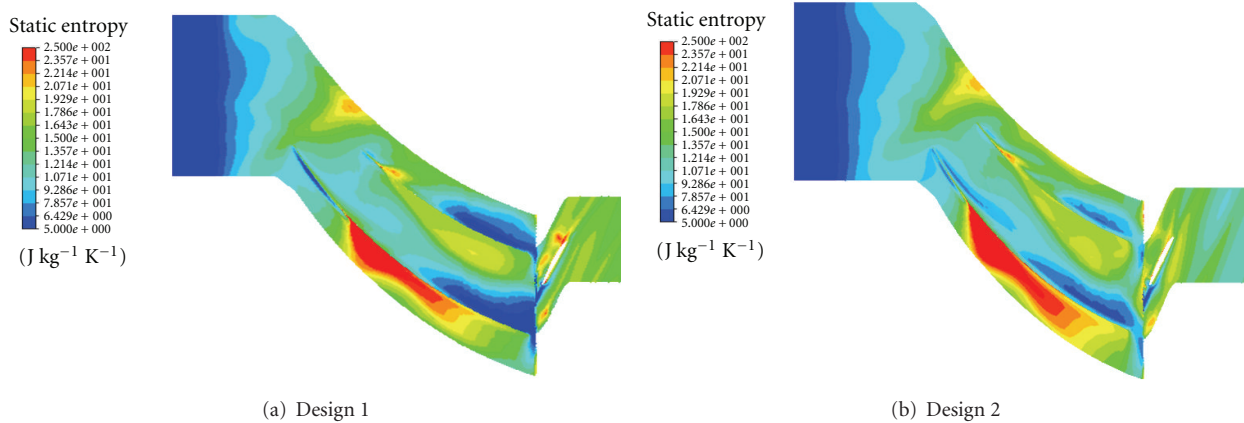


FIGURE 10: Entropy generation inside of the tip clearance (99% span).

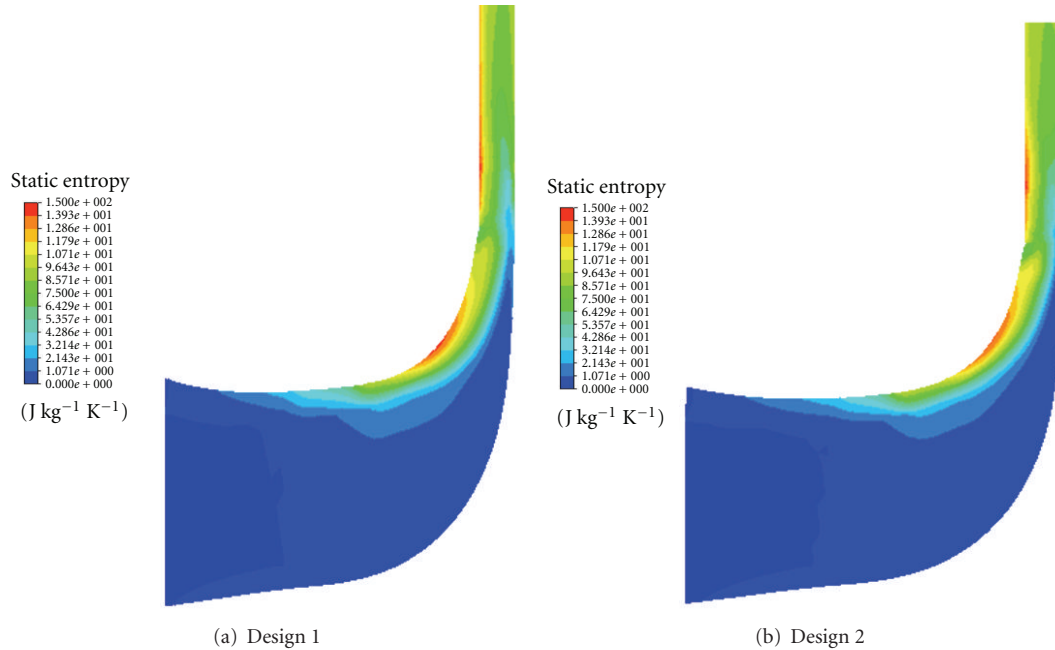


FIGURE 11: Entropy generation along the meridional plane.

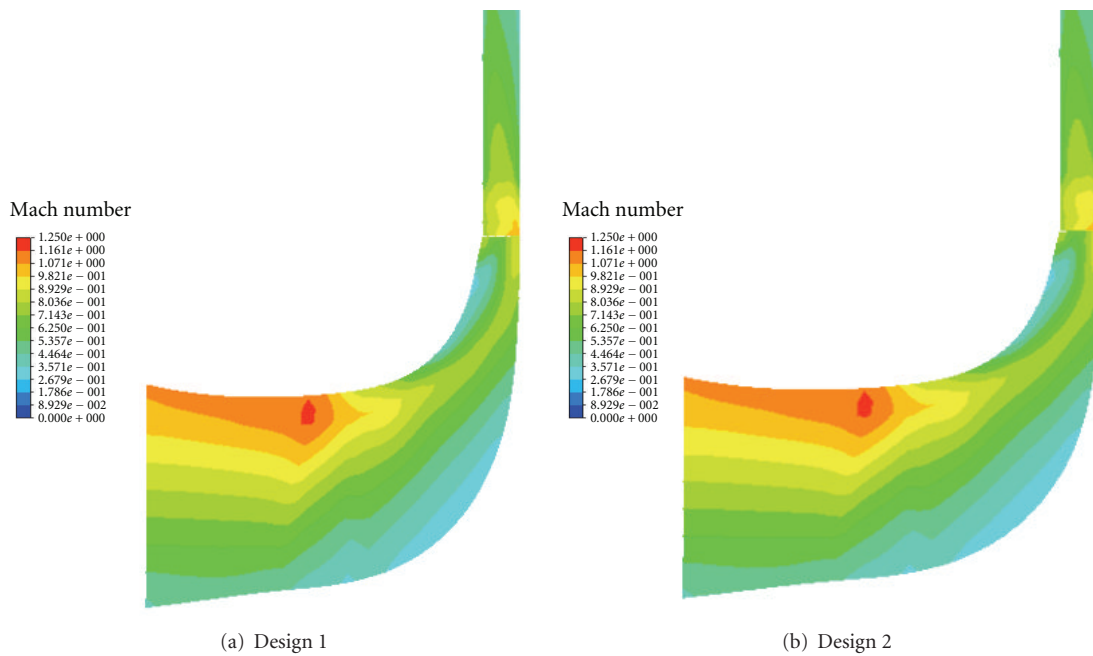


FIGURE 12: Mach number distributions at design point along the meridional plane.

Mach numbers for both designs have different level of static pressure, as shown in Figure 7 and also in Figures 13(a) and 13(b) due to the difference of the mass flow rate. Figures 13(a) and 13(b) also indicate that the static pressure has similar patterns but Design 1 has a little higher impeller exit pressure compared with Design 2. Figures 12 and 13 show that the meridional mid-plane flow structures are mainly determined by blade  $\beta$  angle distributions and the hub and shroud contour shape.

Figure 14 shows the analyses for the clearance sensitivities for both Design 1 and Design 2. Both the nondimensional compressor efficiency and the pressure ratio used the design clearance (about 5.3% B2) as a denominator. It can be seen that for both the pressure ratio and the compressor efficiency, Design 1 is less sensitive than Design 2. The analyses also indicated that the pressure ratios are more sensitive than the stage efficiency. This is because Design 1 has smaller losses near the shroud, as shown in Figure 9.

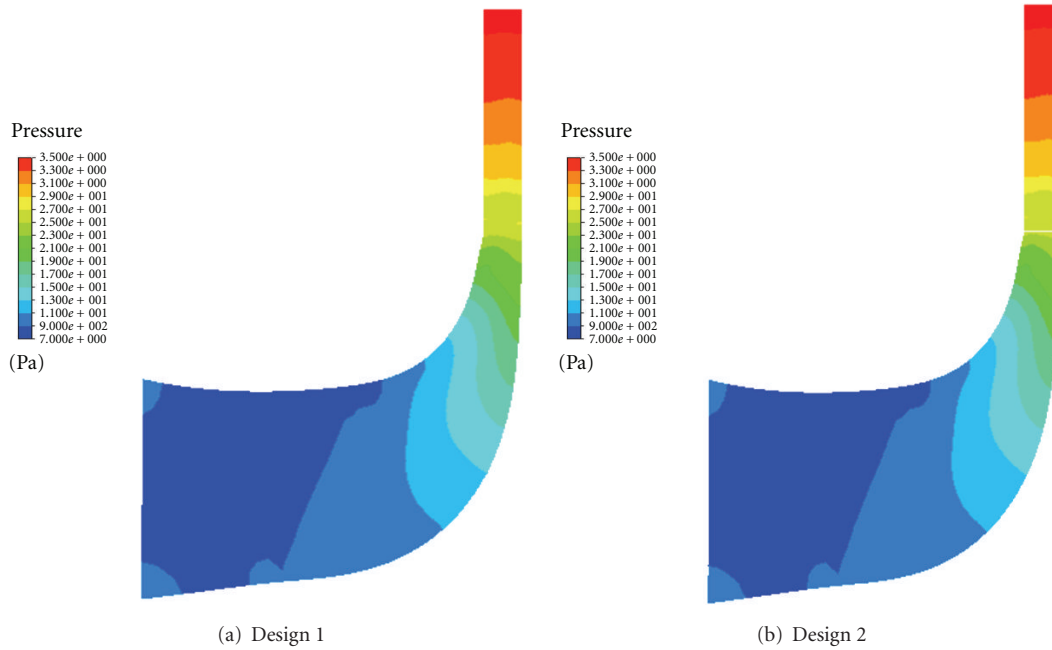


FIGURE 13: Static pressure distributions at design point along the meridional plane.

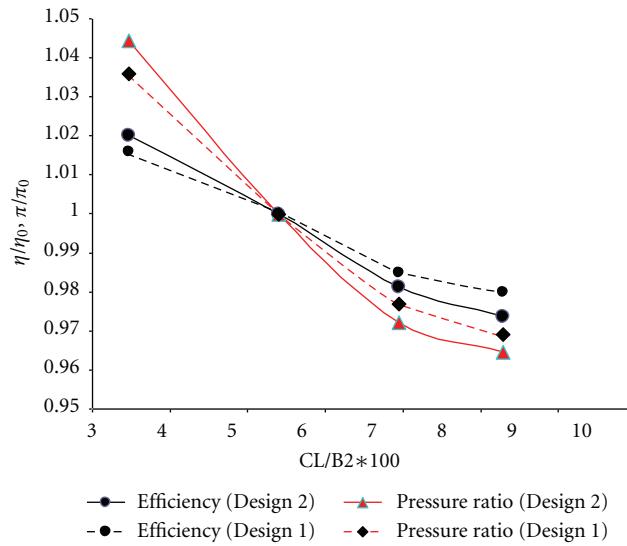


FIGURE 14: Clearance sensitivity.

### 4. Conclusions

This research provides an important study of the meridional features of the centrifugal impeller design. Very little information has been available that provides insights into the importance of the compressor meridional plane at the inlet and the exit of the impeller in the open literature. This study shows that a proper design for the inlet and the exit of the meridional plane can improve the compressor’s overall efficiency and also can reduce the sensitivity of the tip clearance. This study further shows that the meridional plane of the inlet and the exit similar to Design 1 can improve

the flow field near the shroud and improve the overall impeller efficiency. This study also indicates that without changing the other components of the compressor stage, optimization of the impeller meridional shape can improve the compressor stage efficiency and the pressure ratio. This study also provides the upgrading possibilities for compressor manufacturers to make a slight change of the impeller inlet and the exit shape from the old design to improve the compressor’s performance. Finally, this study suggests that the impeller design not only needs to optimize the blade angle distributions, but also needs to optimize the meridional plane.

## Nomenclature

$B$ :	Impeller exit of diffuser width
$K$ :	Turbulence kinetic energy
$CL$ :	Clearance
$C$ :	Total velocity
$C_\theta$ :	Velocity component in rotating direction
$D2$ :	Impeller exit diameter
RMR:	$Mr1/Mr2$
$u$ :	Rotating velocity
$w$ :	Relative velocity
$D$ :	Diameter of impeller
$h$ :	Entropy
$H$ :	Blade height
$I$ :	$h + 0.5 C^2 - uC_\theta$
$i$ :	Point number
$M$ :	Distance along meridional curve or nondimensional meridional curve length
$m$ :	Mass flow
$M2$ :	Absolute Mach number at impeller exit
$Mr1$ :	Relative Mach number at impeller inlet
$Mr2$ :	Relative Mach number of the primary zone at impeller exit
$N$ :	Rotational speed
$P$ :	Control point
$p$ :	Diffuser leading edge pitch $= 2\pi r_3/Z$
$PR_s$ :	Pressure ratio at surge
$PR_d$ :	Pressure ratio at design point
$Q$ :	Volume metric flow
$SB$ :	$(Q_c - Q_s)/Q_c$
$SM$ :	$(PR_s - PR_d)/PR_d$
$t$ :	Parameter
$U$ :	Peripheral velocity
$W$ :	Relative velocity
$x, y$ :	Coordinates
$Z$ :	Number of vane or impeller blade.

## Subscripts

1:	Impeller inlet
2:	Impeller exit
3:	Diffuser inlet
$c$ :	Choke point
$s$ :	Surge point
$o$ :	Operation point
$p$ :	Polytropic
$r$ :	Radial direction.

## Greek

$\beta$ :	Blade angle from radial direction
$\phi$ :	Flow coefficient based on compressor inlet condition $= Q/(ND^3)$
$\eta$ :	Efficiency
$\sigma$ :	Solidity ( $= L/p$ )
$\varepsilon$ :	Turbulence eddy dissipation
$\varphi$ :	Polytropic head coefficient $= H/u_2^2$ .

## References

- [1] W. Jansen and A. M. Kirschner, "Impeller blade design method for centrifugal compressors," NASA SP304, Part II, 1974.
- [2] M. P. Boyce, *Centrifugal Compressor: A Basic Guide*, PennWell Corporation, Tulsa, Okla, USA, 2003.
- [3] D. Japikse, *Centrifugal Compressor Design and Performance*, Concepts ETI, White River, Vt, USA, 1996.
- [4] C. Xu and R. S. Amano, "On the development of turbomachine blade aerodynamic design system," *International Journal of Computational Methods in Engineering Science and Mechanics*, vol. 10, no. 3, pp. 186–196, 2009.
- [5] M. Zangeneh, D. Vogt, and C. Roduner, "Improving a vaned diffuser for a given centrifugal impeller by 3D inverse design," in *Proceedings of the ASME TURBO EXPO*, pp. 1111–1122, Amsterdam, Netherlands, June 2002.
- [6] N. K. Amineni and A. Engeda, "Pressure recovery in low solidity vaned diffusers for centrifugal compressors," 97-GT-472, 1997.
- [7] Y. Senoo, H. Hayami, and H. Ueki, "Low-solidity tandem-cascade diffusers for wide-flow-range centrifugal blowers," 83-GT-3, 1983.
- [8] C. Xu, R. S. Amano, and E. K. Lee, "Investigation of an axial fan—blade stress and vibration due to aerodynamic pressure field and centrifugal effects," *JSME International Journal, Series B*, vol. 47, no. 1, pp. 75–90, 2004.
- [9] L. He and D. X. Wang, "Concurrent blade aerodynamic-aeroelastic design optimization using adjoint method," *Journal of Turbomachinery*, vol. 133, no. 1, Article ID 011021, 10 pages, 2011.
- [10] T. Ghisu, G. T. Parks, J. P. Jarrett, and P. J. Clarkson, "An integrated system for the aerodynamic design of compression systems-part II: application," *Journal of Turbomachinery*, vol. 133, no. 1, Article ID 011012, 8 pages, 2011.
- [11] T. Verstraete, Z. Alsalihi, and R. A. Van den, "Multidisciplinary optimization of a radial compressor for microgas turbine applications," *Journal of Turbomachinery*, vol. 132, no. 3, 7 pages, 2010.
- [12] C. Xu and R. S. Amano, "A study on turbomachinery blade design and optimization procedure," *International Journal for Numerical Methods in Fluids*. In press.
- [13] C. R. Weber and M. E. Koronowski, "Meanline performance prediction of volutes in Centrifugal compressors," in *Proceedings of the ASME 31st Gas Turbine Conference and Exhibit*, Dusseldorf, Germany, 1987.
- [14] J. S. Arora, *Introduction to Optimum Design*, MCGraw-Hill, New York, NY, USA, 1998.
- [15] D. Bonaiuti, A. Arnone, M. Ermini, and L. Baldassarre, "Analysis and Optimization of transonic centrifugal Compressor Impellers Using the Design of Experiments Technique," G T-2002-30619.
- [16] M. J. Harry, *The Nature of Six Sigma Quality*, Motorola University Press, Schaumburg, Ill, USA, 1997.
- [17] C. Xu and R. S. Amano, "A hybrid numerical procedure for cascade flow analysis," *Numerical Heat Transfer, Part B*, vol. 37, no. 2, pp. 141–164, 2000.
- [18] C. Xu and R. S. Amano, "Computational analysis of pitch-width effects on the secondary flows of turbine blades," *Computational Mechanics*, vol. 34, no. 2, pp. 111–120, 2004.
- [19] C. Xu and D. Valentine, "Diffuser for a centrifugal compressor," US patent # 7581925, 1997.

- [20] ANSYS, "Ansys multiphysics, Ver 11.0," ANSYS, 2007.
- [21] C. Xu and M. Muller, "Development and design of a centrifugal compressor volute," *International Journal of Rotating Machinery*, vol. 2005, no. 3, pp. 190–196, 2005.

## Research Article

# Empirical Design Considerations for Industrial Centrifugal Compressors

**Cheng Xu and Ryoichi S. Amano**

*Department of Mechanical Engineering, University of Wisconsin-Milwaukee, Milwaukee, WI 53212, USA*

Correspondence should be addressed to Ryoichi S. Amano, amano@uwm.edu

Received 22 February 2012; Revised 29 April 2012; Accepted 30 April 2012

Academic Editor: Ashwani K. Gupta

Copyright © 2012 C. Xu and R. S. Amano. This is an open access article distributed under the Creative Commons Attribution License, which permits unrestricted use, distribution, and reproduction in any medium, provided the original work is properly cited.

Computational Fluid Dynamics (CFD) has been extensively used in centrifugal compressor design. CFD provides further optimization opportunities for the compressor design rather than designing the centrifugal compressor. The experience-based design process still plays an important role for new compressor developments. The wide variety of design subjects represents a very complex design world for centrifugal compressor designers. Therefore, some basic information for centrifugal design is still very important. The impeller is the key part of the centrifugal stage. Designing a highly efficiency impeller with a wide operation range can ensure overall stage design success. This paper provides some empirical information for designing industrial centrifugal compressors with a focus on the impeller. A ported shroud compressor basic design guideline is also discussed for improving the compressor range.

## 1. Introduction

New compressor designs always must meet the customers' needs with the shortest time to market, low cost, and improved performance. To push the design to state of the art aerodynamic performance, the structure design also needs to meet a suitable performance life of the compressors. Mechanical integrity is one of the important parts of the centrifugal compressor design. Mechanical constraints are usually negative factors for aerodynamic design, for example, mechanical constraints require thick blade for reliability but hurt impeller efficiency. The purposes of the mechanical analyses are to provide all compressor components within a reasonable time duration to sustain the aerodynamic and centrifugal force, and eigen frequencies do not match critical excitation frequencies [1]. The safety factors of the mechanical design had been reduced dramatically compared with "old fashioned" design. Due to the nature of the Finite Element Analysis (FEA) tools and material property improvements, the safety factor of a modern industrial compressor design normally is set to 7 to 12%. The mechanical requirements need structure designers to have better practice to allow more freedom to aerodynamic designers and to keep all the components at the lowest weight and the lowest cost.

Design of a long lifetime single component of compressors is not a goal for designers. Emphasis on improving efficiency has been a primary issue, but this also is not as important as in the past. The development cost and development time is also a key factor that needs to be considered for a modern compressor design. Industrial compressor design expects a state-of-the-art performance compressor without making a second build for less cost and short development time. For achieving this goal, compressor design engineers need to have multidiscipline knowledge of centrifugal compressor design. Detailed design considerations can reduce the time to perform the advance design studies and laboratory investigations. The wide variety of design subjects represents a very complex design world for compressor designers. One purpose of this paper is to provide information in an aerodynamic point of view to understand the overall design before starting the detailed design process of a centrifugal compressor. The paper also summarizes important aspects of the centrifugal compressor design for industrial compressor designers and scientists.

The compressor market and business model has changed in the last few decades. Industrial compressor design now requires designing for success in the marketplace, not just for scientific experiments. In the past, compressor designers

developed a new compressor in the development group and passed the design to manufacturing. The manufacturing group would evaluate how to make it at the lowest cost, and some designs were rejected because they could not meet the market requirements. The new development model requires the compressor designer to design for market, manufacturing, and end users. New business concepts have been proposed [2, 3] in which the design also considers an integrated system of manufacturers and end users. The new compressor developments become a complex system task. Minimizing manufacturing cost of the compressor design is not enough. The compressor design must consider all aspects of the manufacturing and end users. If surplus is defined as the total profit of manufacturing, end users, and aftermarket, the compressor's new development will focus on the design for maximum surplus. Therefore, in the compressor design stage, many choices of design options need to be considered before the final design, and discussions must consider the surplus value. It is essential that design engineers begin to perform a compressor design with full understanding of all aspects of the design considerations [4–8].

To reduce manufacturing cost, many high volume compressor manufacturers, for example turbocharger, often use the flow cut for different applications. The flow cut uses the same defined blade geometry for multiple flows and a similar or lower pressure ratio. This is different from scaling, in that the impeller blade and any diffuser vane geometry maintain the same definition. A brief introduction of the flow cut is also discussed in this paper.

With the development of computational science and computer hardware, design engineers rely on quality models to establish the physical relationships among diverse thermodynamic, geometric, and fluid dynamic parameters that govern turbomachinery performance [9–26]. Although CFD has helped to design many successful industrial compressors and has become an important tool in industrial compressor design, multidomain optimisation is still very time consuming. Most CFD optimisations still focus on the component [22]. When the compressor inlet flow is reduced, the compressor experiences an unsteady flow phenomena surge and rotating stall. These instabilities can cause noise nuisance and critical operating conditions with strong dynamical loading on the blades. Therefore, they cannot be tolerated during compressor operation. With the reduction of the compressor inlet flow, a rotating stall occurs in the impeller, or diffuser or scroll. If the compressor inlet flow continues to reduce, the rotating stall eventually will drive the compressor into a surge [27–32]. A rotating stall is an unsteady and three-dimensional flow phenomenon. CFD simulation is still a big challenge. The flow range of a centrifugal compressor can be extended by allowing gas to bleed from a ring of holes or a circular groove port around the compressor casing at a point slightly downstream of the compressor inlet. This type of the compressor called ported shroud compressor. Ported shroud forces a simulation of impeller stall to occur continuously, allowing some air to escape at port location inhibits the onset of surge and widens the operating range. The flow inside port is unsteady and complicated when compressor stalls. CFD guides ported shroud design is still very

time consuming and less reliable. Some design practices for a ported shroud impeller casing [33] are discussed for improving the compressor operational range.

## 2. Industrial Centrifugal Compressor

Centrifugal compressors are widely used in automotive, marine turbocharging, oil and gas, aerospace, and distributed power applications because of their compact design and high stage pressure ratio. With different types of applications, the structural characteristics of the compressors have two basic types, that is, horizontal split and vertical split, as shown in Figure 1. Horizontal split type compressors are applied for low-to-medium pressure service, as shown in Figure 1(a). This type of casing is split along the rotor shaft and bolted at the split line. The bearing and seal sections allow easy disassembly and assembly via the inspection cover, without having to remove the upper casing. A vertical split compressor is easy to access the gears, bearings, seals, and be repaired on site. However, due to the large crossing area in the splitting surface, it is difficult to prevent gas and lubricant oil leakage. A vertical split compressor is applied for medium- and high-pressure service, as shown in Figure 1(b). This type of compressor consists of an inner casing and an outer casing. The inner casing forms a single unit with the head, bearing, and seal and is fixed to the outer casing by shearing. The nozzle can be attached to the top, bottom, or side in accordance with client specifications. Both bearings and seals can be inspected without removing the inner casing. However, the manufacturing cost and installation cost may be higher than for a vertical split compressor. It is also not easy to access the gear, bearings, and seal. For combining the advantages of both split types, a hybrid split has become popular. For some applications, the gearbox can be a vertical split, and the compressor stage can use a horizontal split, as shown in Figure 1(c).

## 3. Impeller Design Methodologies

The impeller is a key component to influence overall performance of a centrifugal compressor [5]. The efficiency of centrifugal compressors has increased dramatically, especially low-pressure ratio centrifugal compressors. A major challenge for a centrifugal compressor design is to keep a high efficiency level at a state of the art and to increase the compressor operating range [27–33]. Increasing the compressor operating range without sacrificing compressor peak efficiency is difficult to achieve. Aerodynamic engineers not only need to understand the surge physics but also need to apply design experience to the design. Another important objective for impeller design is to reduce the manufacturing cost. Manufacturing cost could be reduced when designs for manufacturability are effectively considered. The impeller should meet requirements to be easily withdrawn from a casting mold without destruction and disassembly of the mold for a casting impeller. This requires the lean angle of the blade to change linearly with the impeller radius and axial direction, as shown in Figure 2. All these considerations

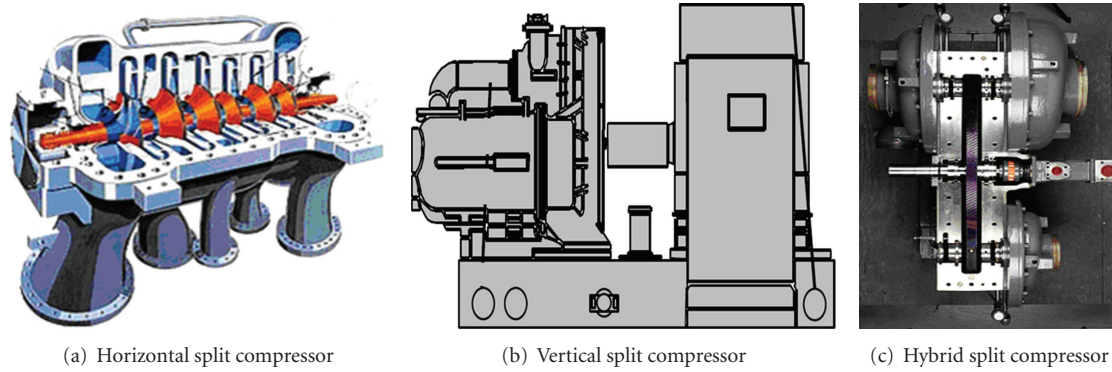


FIGURE 1: Compressor split types.

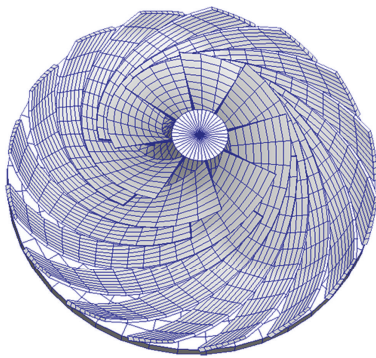


FIGURE 2: Impeller for manufacturing.

for design will help the final design to meet the compressor design target with fewer design iterations.

Different designers may have different methodologies for impeller developments. What kind of area distributions, curvatures, velocity, or pressure profile will lead to a good design is strongly dependent on the designers' practice and experience. Two totally different design philosophies could produce similar performance. For example, two impellers designed by Garret and Pratt Whitney [7], as shown in Figure 3, had different shapes with similar performance at the design point. The impeller designed by the author also presented different features, which also provide a good performance. It is shown that, if design follows basic design guideline, a wide range of solutions to the design can be used.

The authors' design, as shown in Figure 3, is an example of a recently developed single-stage centrifugal compressor. At the design point, the total to static stage pressure ratio was about 3.7, and the flow coefficient was about 0.12. The running clearance at the impeller tip was 4.5% of the impeller exit blade width. Six builds were assembled and tested based on the ASME PTC-10 test procedure [34]. The compressor performance obtained from an average of six build tests is shown in Figure 4. The differences of test results for different builds for adiabatic efficiency and head coefficient were within  $\pm 0.5\%$  and  $\pm 0.75\%$ , respectively. The test uncertainties for total pressure (in psi), static pressure (in psi), and temperature (in Fahrenheit) were  $\pm 0.25\%$ ,  $\pm 0.2\%$  and

$\pm 0.5\%$ , respectively, based on uncertainty analysis [14]. Test results showed that the compressor performance was encouraging at both the design and the off-design point. The design met the low-cost target and allows large manufacturing tolerances. The insensitivity of the impeller surface finish and large tip clearance makes it easy to assemble.

#### 4. Impeller Geometry

The initial design of a centrifugal compressor always begins with requirements from customers or marketing analysis. Designers select basic configurations and provide basic performance to customers or marketing by using their experience data. Aerodynamic designers also need to provide an estimation for the compressor's basic geometry to engineers in other disciplines. For example, rotor-dynamic engineers and bearing designers rely on the impeller geometry information to perform their work. Although the basic geometry design is not intended to yield optimization of the impeller, it can accelerate the overall design process and reduce the development cost.

Before aerodynamic designers determine the basic impeller geometry, the rotational speed of the impeller needs to be selected. If there are no special requirements for rotational speed, we normally optimize rotational speed based on the Balje's charts [35, 36] by using optimal specific speed. Although Balje's charts are not very accurate tools, they are sufficient enough to provide the initial estimate for impeller geometries.

During the initial design, the important information needed for bearing designers and rotor-dynamic engineers is impeller weight. Aerodynamic designers can estimate impeller sizes based on the required gas flow, pressure ratio, and impeller rotational speed. Our design practices showed that the weight of the impeller is the function of the impeller diameter. Figure 5 summarizes the relationship between the impeller diameter and the weight for sixteen ASTM A564 stainless-steel unshrouded impellers. The impeller weight mainly is determined by the impeller disk; the blades only contribute a very small portion of the weight. Therefore, we plotted impeller weight and diameter relation in one figure

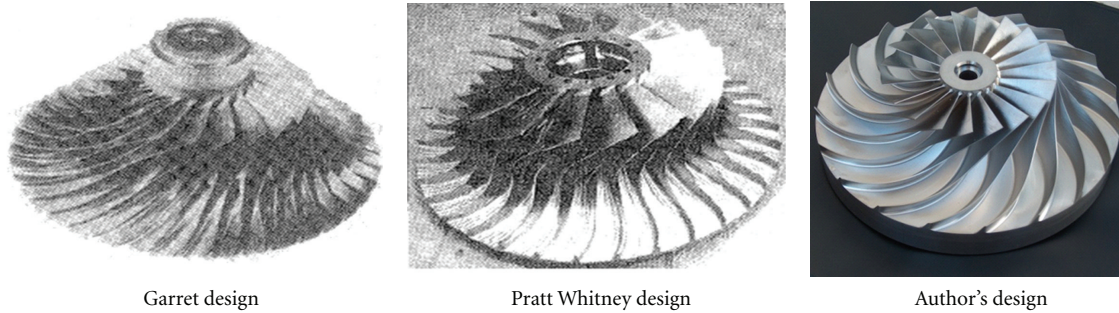


FIGURE 3: Different impeller designs.

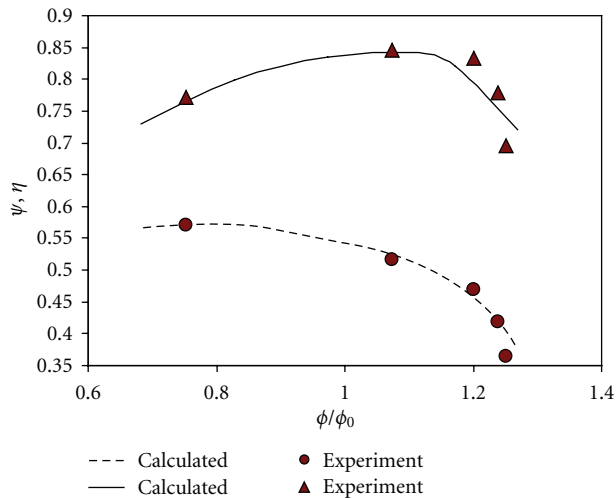


FIGURE 4: Single stage compressor efficiency and head coefficient versus flow coefficient (upper curve is the adiabatic efficiency, and lower curve is head coefficient).

for all designed unshrouded impellers with different blade counts and with or without splitters.

In an initial stage of compressor design, selections of the impeller inlet, the outlet velocity vectors, and the choice of blade numbers are the key initial design decisions. Velocity vectors may be obtained through a mean-line program. The experience data show that both the inlet blade numbers and the exit blade numbers are a function of stage pressure ratio. Relationships between the numbers of blades and the stage pressure ratio are shown in Figures 6 and 7 for with and without splitter impellers, respectively. In general, high-stage pressure causes a blade-loading increase, and the impeller needs more blades to distribute loading. Variations of the numbers of blades at a similar pressure ratio were due to the size of the impellers. For a smaller-sized impeller, manufacturing capabilities may limit the number of blades. Impeller sizes plotted in Figures 6 and 7 are in the range from 2 inches to 45 inches. The machine performance requirements and manufacturing feasibilities are factors to determine whether to use splitters or not.

The inlet blade height is determined by the design inlet flow rate and the impeller hub radius. The inlet hub radius is

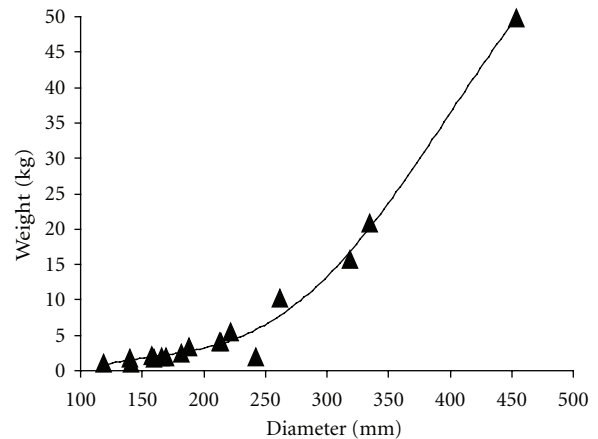


FIGURE 5: Impeller weight with diameter.

determined by the attachment of the impeller. For overhung impellers, the inlet hub radius normally is selected in a range between 10% and 20% of the impeller tip radius. For the shaft and bolt through the impeller, selections of the inlet hub radius are based on stress requirements.

The blade thickness at the inlet and the discharge was determined mainly by tensile and bending root stresses at the leading edge and the blade exit. FEA calculations and stress tests showed that blade root stresses are mainly caused by the centrifugal force. The blade high was a key factor to impact the blade root stresses. The mean-line thickness at the inlet and the exit was determined by the blade heights at the inlet and the exit, as shown in Figures 8 and 9. Experience showed that the blade thickness changed linearly with the blade height.

The three-dimensional features of the impeller blade are dependent on the engineers' experience and on stress limitations. The modern impeller is normally a three-dimensional design. The wrap angle, lean angle, and back sweep angle use a larger value than those in the past. The large wrap angle can reduce the camber of the blade but increase the frictions of the fluid. A large lean angle permits blade design at all blade sections with the desired shape. Leaning the blades creates a back-sweep and retains purely radial fibers, which are beneficial for bending moments. Experience showed that impellers with a back sweep generally have high efficiency.

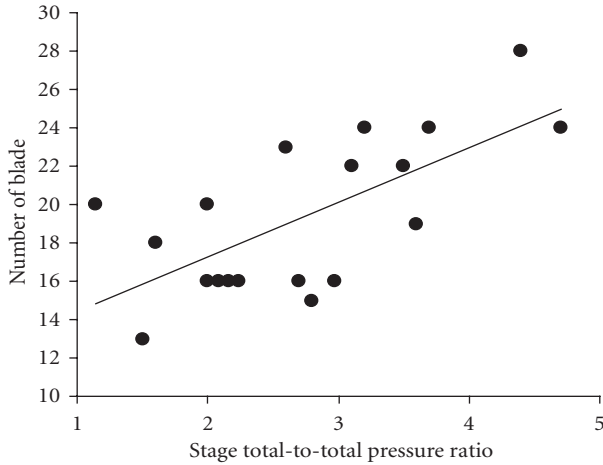


FIGURE 6: The number of blades at the inlet versus stage pressure ratio.

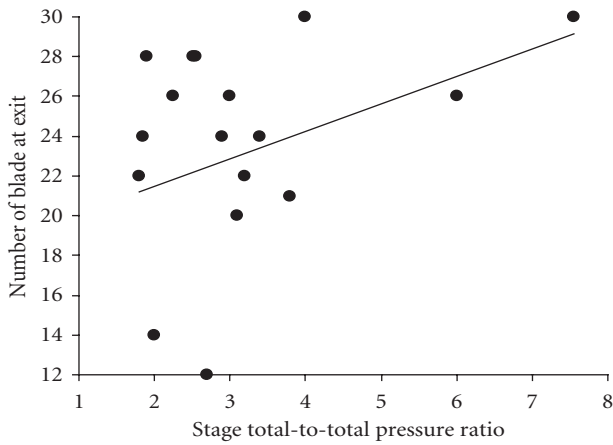


FIGURE 7: The number of blades at the exit versus stage pressure ratio for split impellers.

### 5. Reynolds Number and Surface Finish

The Reynolds number or the Ross by number has significant impacts on the impeller maximum surplus value. Fundamental fluid dynamics theory [37, 38] shows that the flow inside a pipe for a different Reynolds number represents different flow patterns. This is also true for flow inside impeller blades. Experience showed that if there is a flat velocity profile at the inlet between two impeller blades or diffuser vanes, the flow development along the flow channel presents different profiles with different Reynolds numbers. For low Reynolds number flows, the exit velocity profile is almost parabolic and only with a small portion of a flat profile. For high Reynolds number flows, the exit velocity profiles have large flat profiles.

The peak meridional velocities for high Reynolds number flows are normally located at the hub pressure sides of the blade due to potential flow effects. Low Reynolds number flow regions are located near the suction side of the blades. The viscous jet and wake interaction causes flow separations.

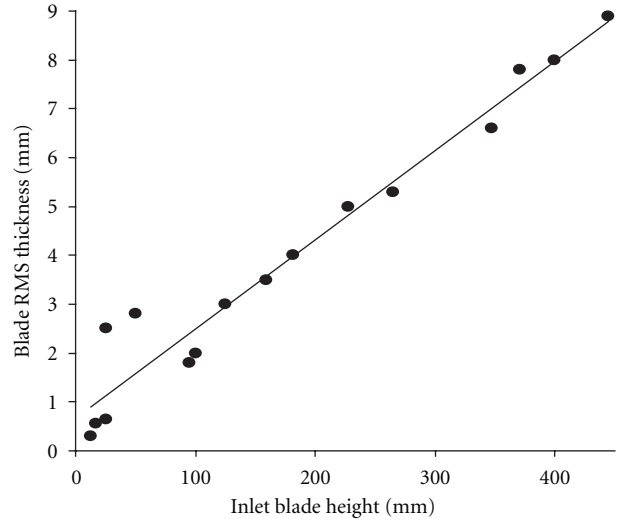


FIGURE 8: Relationship between impeller inlet RMS thickness and inlet width.

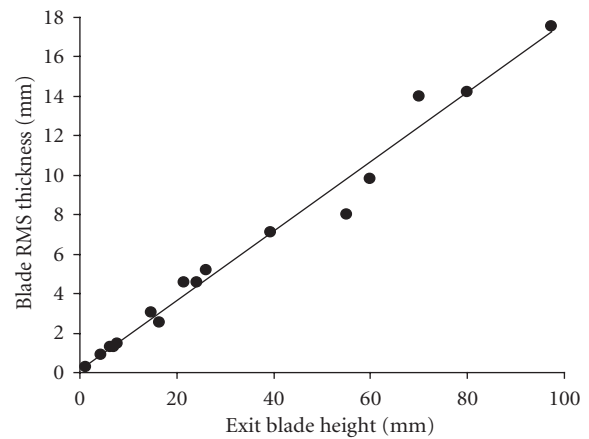


FIGURE 9: Relationship of impeller exit RMS thickness and tip width.

The Reynolds number also strongly influences secondary flow patterns. Increasing the Reynolds number increases the strength of the clockwise secondary passage flow circulation. Reducing pressure on the suction velocity gradient increases the flow circulation of the counter clockwise secondary flow. The optimum design should try to offset each other to minimize the secondary flow losses.

The machining and casting of centrifugal compressor impellers and other components result in an inherent surface roughness. The sizes and forms of roughness depend on the manufacturing process. The levels of the surface finish represent the manufacturing cost. It is very important to balance manufacturing cost and performance. Surface finish requirements for different designs have different requirements. A detailed discussion on surface finish and Reynolds number can be found in reference [39, 40]. Loss due to the

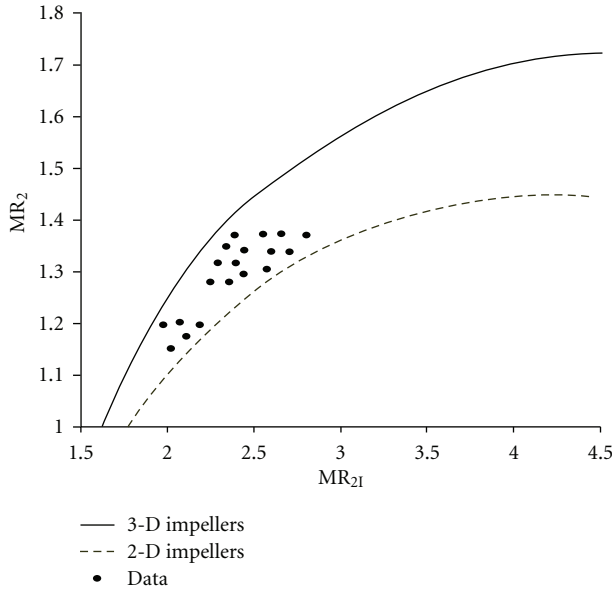


FIGURE 10: Relationship of  $MR_2$  versus  $MR_{21}$ .

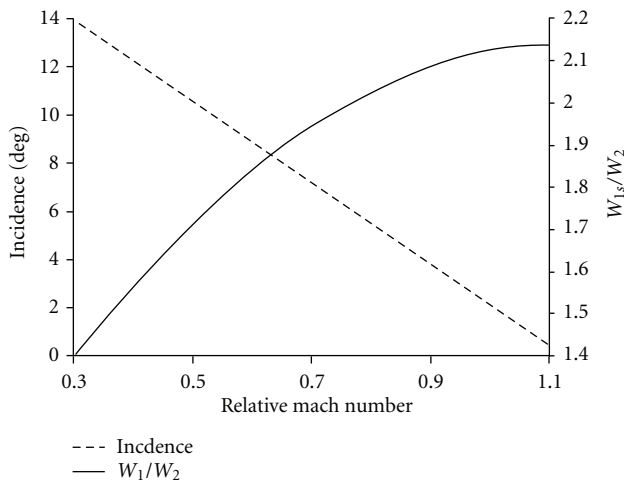


FIGURE 11: Stall incidence and relative velocity ratio versus Mach number.

surface finish can be represented as wall friction. Wall friction is the function of Reynolds number and can be written as

$$\frac{1}{\sqrt{f}} = 1.74 - 2 \log_{10} \left( \frac{k}{B_2} + \frac{18.7}{\text{Re} \sqrt{f}} \right). \quad (1)$$

This equation can be solved by using a simple computer program or spreadsheet.

## 6. Impeller Aerodynamic Design

One important guideline for impeller aerodynamic design is to set a reasonable diffusion ratio. The diffusion of the impeller can be represented by velocity ratio, diffusion factor, and relative Mach number ratio. The ratio of the relative Mach

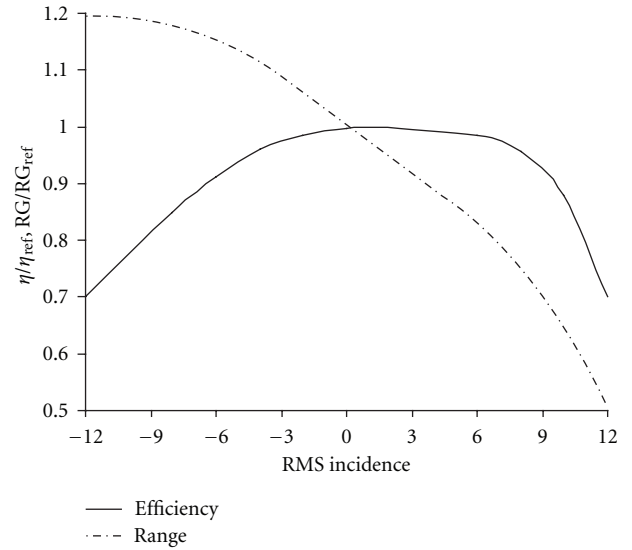


FIGURE 12: Incidence versus efficiency and range.

number was used in this discussion because it can avoid the one-dimensional assumption at the inlet.  $MR_2$  is defined as the ratio of the relative Mach number at the impeller inlet to the average Mach number at the impeller exit. Figure 10 shows the upper and lower boundaries for maximum deceleration likely to be achieved for two-dimensional and three-dimensional impellers [8]. The experience data fell inside the theory boundaries, and the Mach number ratio  $MR_2$  fell between 1.15 and 1.4, giving a good overall performance. The upper boundary of  $MR_2$  of 1.4 for an industrial compressor and 1.7 for jet engine impellers are reasonable expectations. Our experience also indicated that a large diffusion might cause a large loss. The ratio of the Mach number can be selected within a large range. An important factor to impact the selection of diffusion level is the inlet Mach number. Figure 11 is a relationship between the relative velocity ratio, the incidence, and the inlet relative Mach number for a typical industrial impeller. It can be seen that diffusion is not an absolute parameter, which influences the stall of the compressor. It is worthwhile to point out that this test impeller was stalled first at the inducer. The inducer shroud velocity represented the rotational speed.

Traditionally, the impeller inlet incidence is set to zero at the design condition. Modern impeller designs need not only to consider maximum efficiency at the design point, but also to consider the manufacturing cost and the off-design performance for the whole operating range [8]. Inlet blade angles are not necessary the same as the inlet relative flow angles. Experience data in Figure 11 shows that changes of the inlet flow incidence impact both the efficiency and the operating range of the impeller. Figure 12 shows that little negative incidences could raise the impeller operating range. However, when the negative incidence increased to a certain level, the operating range did not enlarge and efficiency dropped significantly. The impeller design should avoid this situation.

Estimations of the impeller exit width are critical for both the primary performance estimation and the basic dimension setup. The major impacts of the impeller blade exit width are the flow capacity and the pressure ratio of the stage. It is difficult to calculate the impeller exit width accurately in a simple way. The Rodgers diffusion factor equation [41] provided a good estimated value for the impeller exit width ( $B_2$ ). If the mean meridional blade length can be estimated as

$$L = \frac{2\pi(r_2 - r_1)}{4}, \quad (2)$$

then the impeller exit width can be estimated as

$$B_2 = \frac{10(D_2 - D_{s1})}{1 + (W_2/W_1)} \left[ DF - 1 + \frac{W_2}{W_1} - \frac{\pi D_2 C_{r2}}{2LzW_1} \right] - \frac{(D_{s1} - D_{h1})}{2}. \quad (3)$$

Secondary flows inside the impeller are caused by an imbalance of the static pressure and the kinetic energy. One of the typical secondary flows, the horseshoe vortex, has been well documented. It is shown that the strength of the secondary flows is governed by the vortex starting conditions. The further development of the vortex is determined by the conservation of angular momentum. The impeller meridional blade profiles influence the secondary flow loss level and the laminar viscous dissipation function can estimate the secondary flow loss due to the blade profiles [8]. We have

$$\Delta H_l = N \int \mu \left[ 2 \left( \frac{\partial u}{\partial x} \right)^2 + 2 \left( \frac{\partial v}{\partial y} \right)^2 + \left( \frac{\partial u}{\partial y} + \frac{\partial v}{\partial x} \right)^2 \right] dV. \quad (4)$$

Tip clearance cannot be avoided for unshrouded impellers. Bearing clearances and manufacturing tolerances of the impeller and the intake ring control the minimum impeller tip clearance. The minimum tip clearance is normally defined at the maximum rotational speed with hot weather conditions for most motor-driven compressors. For compressors installed in the same shaft with a gas turbine, the minimum compressor tip clearance was estimated when the compressor was operating at maximum rotational speed with hot weather and with the machine overall net axial thrust load towards the compressor. The tip clearance increases quadratically with the impeller rotational speed if other operating conditions do not change. The tip clearance impacts the overall compressor performance because it increases the magnitude of the secondary flow inside the impeller blades and produces strong tip vortices. The tip clearance flow transports a low momentum fluid from the suction side to the pressure side of blades. The circumferential center of the secondary flow is dependent on the size of the tip clearance. Secondary vortices are located near the shroud side for small clearance, whereas secondary vortices may spread to the center and even the hub of the flow channel for a large tip clearance impeller. The clearance distribution affects the wake formation and the location at the impeller exit.

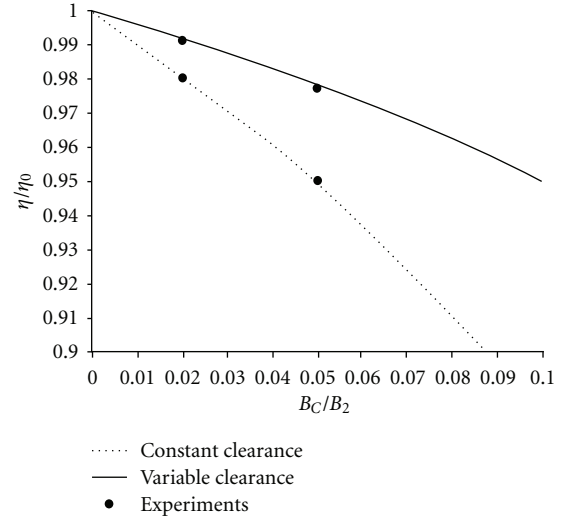


FIGURE 13: Compressor efficiency change versus clearance.

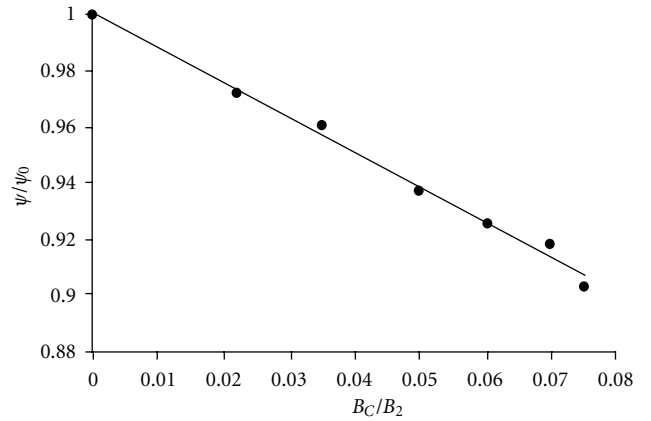


FIGURE 14: Head coefficient change with tip clearance.

A large clearance at the leading edge results in a low-energy center close to the suction side of the blade. Reducing the clearance at the leading edge, the wake moves towards the pressure side of the blade. The tip clearance setting depends on the compressor's maximum surplus value. There are several methods to reduce the tip clearance losses. Figure 13 shows that variable clearance could significantly improve the stage efficiency of compressors. The tip clearance changes the compressor stage head and capacity. Test data indicated that the head coefficient almost changed linearly with the tip clearance, as shown in Figure 14, and the flow coefficient followed a secondary order curve with clearance, as shown in Figure 15.

With the manufacturing technology improvement and design system improvement [42, 43], modern impellers always are designed in a three-dimensional shape. It is very important to understand the impact of the three-dimensional feature on performance and structure. Lean is one of the critical three-dimensional features. In general, both negative and positive lean improves the peak efficiency. One of the design examples for lean effects is shown in Figure 16.

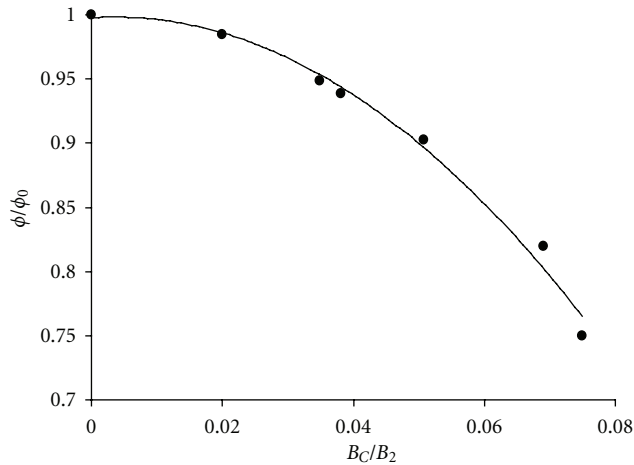


FIGURE 15: Flow coefficient change with tip clearance.

Negative lean has the best peak efficiency, while positive lean has a wide operating range. It can be seen from Von Mises stress contour plots in Figures 17 and 18 that the Von Mises stress is the highest for a negative four-degree lean on a suction surface, and the stress is the lowest for a four-degree lean. However, the pressure side stress contours show the lowest leading edge stress area for a negative four-degree lean design compared with other cases. The negative lean has maximum stress for both the leading edge and the trailing edge while the positive lean has the lowest maximum stress in all locations. The highest stress areas for the positive lean are less than the negative lean and no lean cases. The bore stress and back face stresses are similar because the blade thickness distribution is similar. It can be seen that a small positive lean can reduce the peak stress.

## 7. Impeller Flow Cut

For large volume low-cost compressors, for example, automobile turbochargers, the impeller flow cut is always used for meeting different flow and pressure ratio requirements with minimum manufacturing cost. A flow cut is defined as a change to the impeller blade height or a change to the shroud contour while following the same hub contour and blade angle definition as the original impeller design. This allows a single manufacturing method to be used for the base impeller, plus a machining operation to adjust the blade height and the flow capacity of the impeller. Achieving the objectives for high efficiency and end users' cost of a compressor installation are always in conflict with each other. The flow cut of a compressor stage is one of the important activities of centrifugal compressor manufacturers to achieve a certain performance level with minimum cost. A theoretical equation provides the basic information, but the empirical performance effects on the compressor stage are very important to the compressor manufacturers. Figure 19 shows the original impeller (Figure 19(a)), the shroud contour cut (Figure 19(b)), and a diameter cut (Figure 19(c)). Modern impeller design normally has a bigger back sweep angle, as

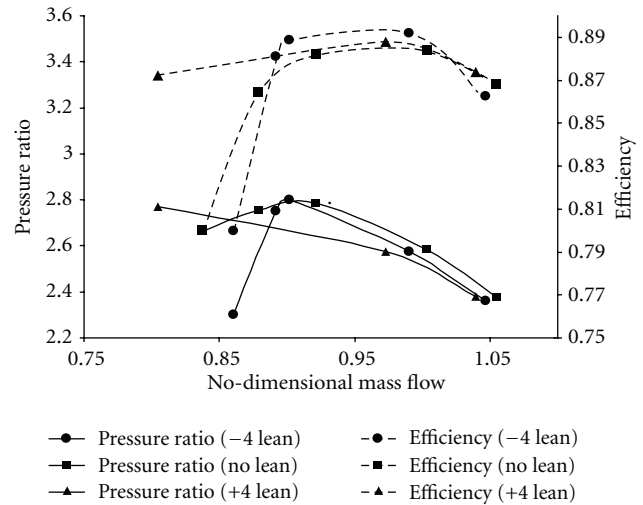


FIGURE 16: Compressor performance for a lean blade.

shown in Figures 2 and 3. The diameter cut, as shown in Figure 19(c), affects the impeller performance at a significant level. Therefore, the diameter cut is less popular than the shroud contour cut.

Here we present some test experience for both the shroud and the diameter contour cut. The shroud contour cut (or extend) is defined as the percentage of the local blade height. Most of time, manufacturers extend or trim the shroud contour the same percentage of the impeller inlet and exit blade heights. For large industrial compressors (choke flow larger than 1000 ICFM (0.472 m<sup>3</sup>/s)), the flow changes normally near linear to the contour change. The major impacts of the flow cuts on the compressor performance are the compressor stage efficiency and the surge flow or the operating range (RG). Figure 20 is the head coefficient at surge point changes with the impeller contours, where the surge point defined here is the operation point at which the compressor stage adiabatic efficiency is 55%. It is shown that the head coefficient at the surge increased as the contour increased. This may be because when the contour increases, the cold tip clearance remains the same during the tests for all the contours. For a larger contour, the tip clearance percentage relative to the impeller exit blade height is smaller, and the surge margin improves. This may be for the same reason. When the contour increases a little, the stage efficiency increases until the design penalty away from the design point is larger than the clearance loss reduction, the compressor efficiency starts to drop, as shown in Figure 21. Test results also suggest that an increased contour, a broader range of high efficiency exists. Testing also indicates that the point of peak efficiency is not proportional to the change in the area of the impeller inducer and the exit geometry. It is interesting to see that the flow corresponding to the peak efficiency increases as the impeller contour increased, as shown in Figure 22. It is important to make the flow cut to ensure the peak efficiency at the operating flow.

Although the diameter cut is less popular than the shroud contour cut, understanding fundamental information and

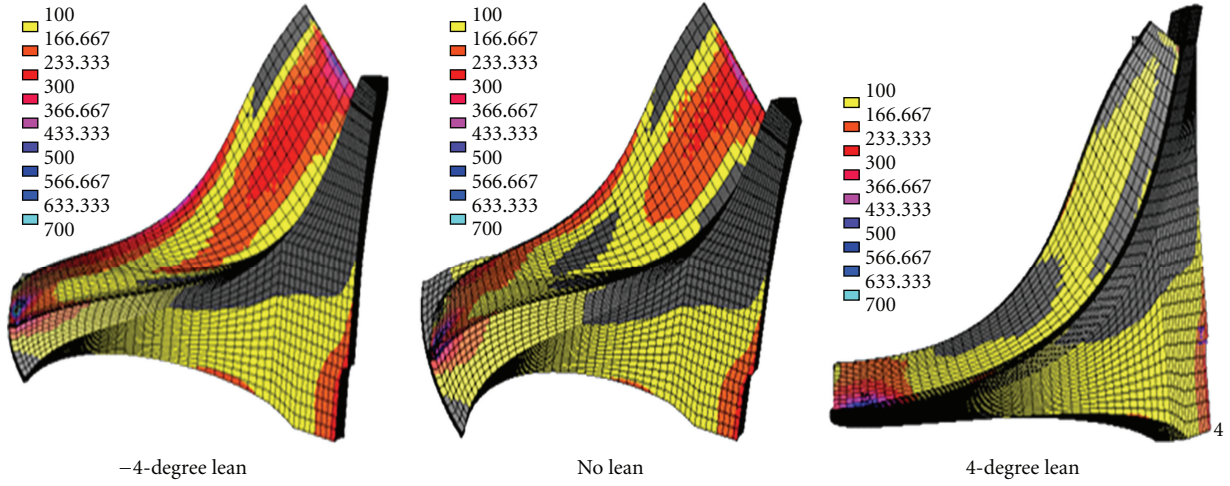


FIGURE 17: Von Mises stress at the suction side of the wheel.

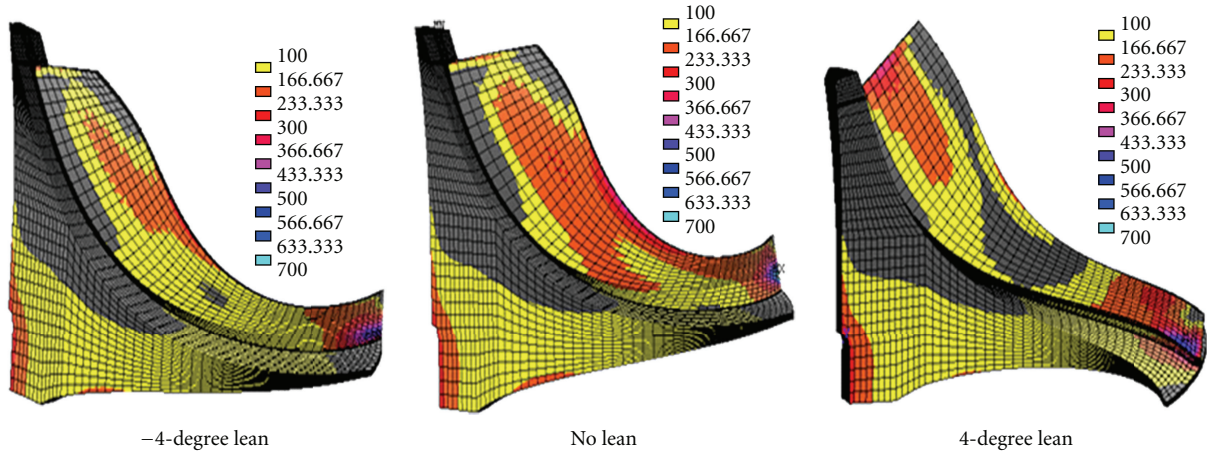


FIGURE 18: Von Mises stress at the pressure side of the wheel.

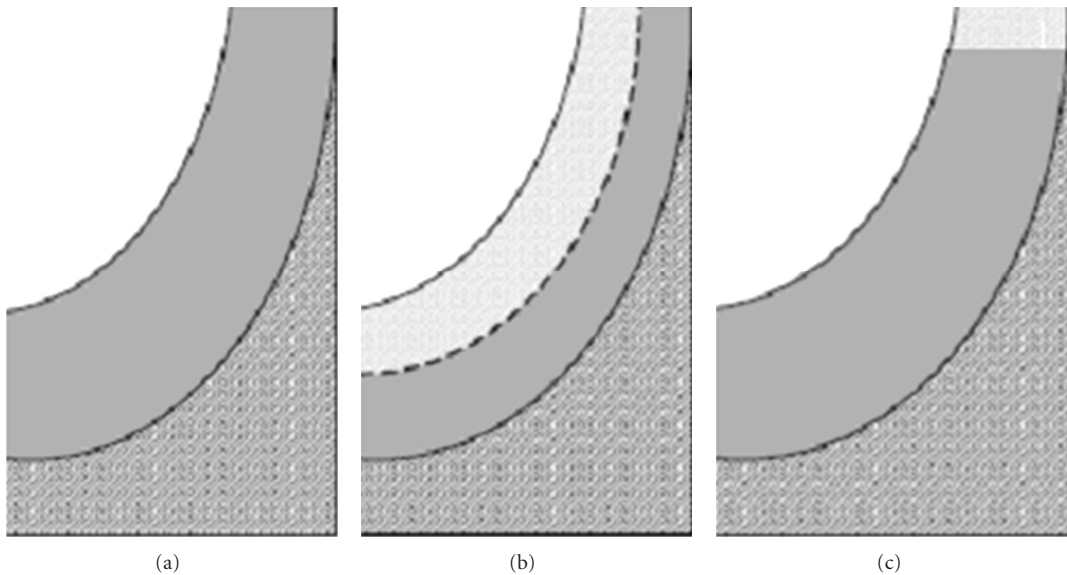


FIGURE 19: Flow cut of the impeller.

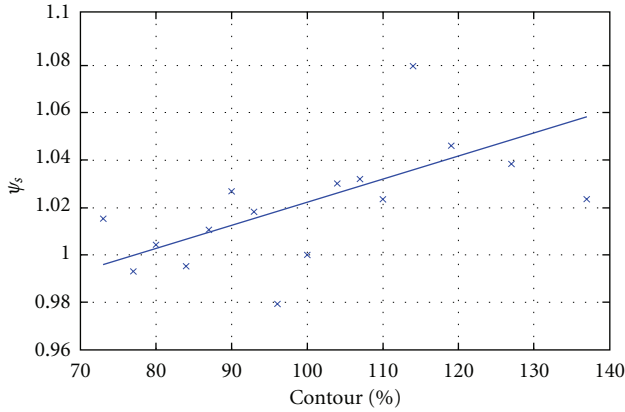


FIGURE 20: Head coefficient at the surge as a function of the contour.

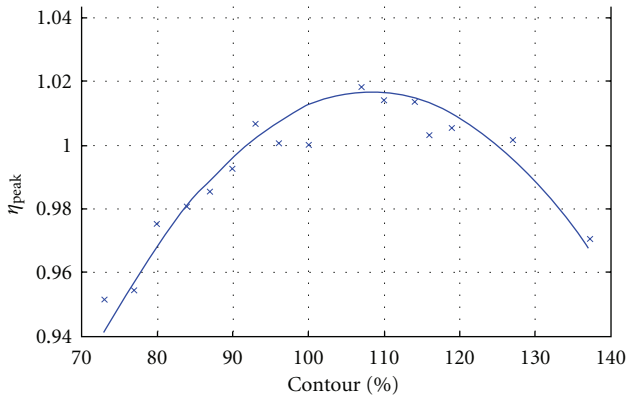


FIGURE 21: Peak efficiency change with flow cuts.

basic compressor characteristics for the diameter cut is also very helpful. Figure 23 is the medium back-curvature impeller compressor (about 25 degree back-curvature) characteristics of a diameter cut. It can be seen that the diameter cut not only affect the peak efficiency but also affect the peak efficiency location. The impeller peak efficiency of a small diameter impeller is located in the lower pressure ratio operating point. It also can be seen that the compressor operating range is reduced after the diameter cut. It is interesting to notice that the surge boundary slope increases with the diameter decrease.

## 8. Ported Shroud Impeller Casing

A compressor surge is a system-unstable phenomenon that is influenced by all components of the compressor. The physics of surge and stall are still not fully understood. We still cannot find any tool that can capture all features of the surge and stall, as shown in Figure 24. Many theoretical studies [27, 30, 31, 44] have focused on a better understanding of the surge and stall, but none can be used as a design tool yet. More theoretical work and experimental studies need to be done in order to incorporate stall in the design system. Designs for a wide operating range were mainly dependent on engineers'

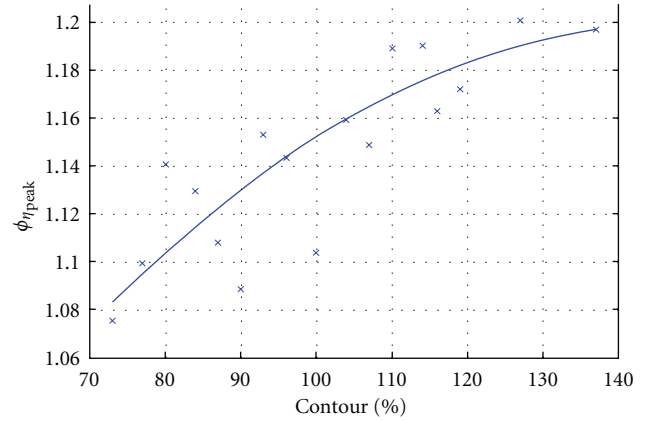


FIGURE 22: Flow coefficient at the peak efficiency versus the flow contours.

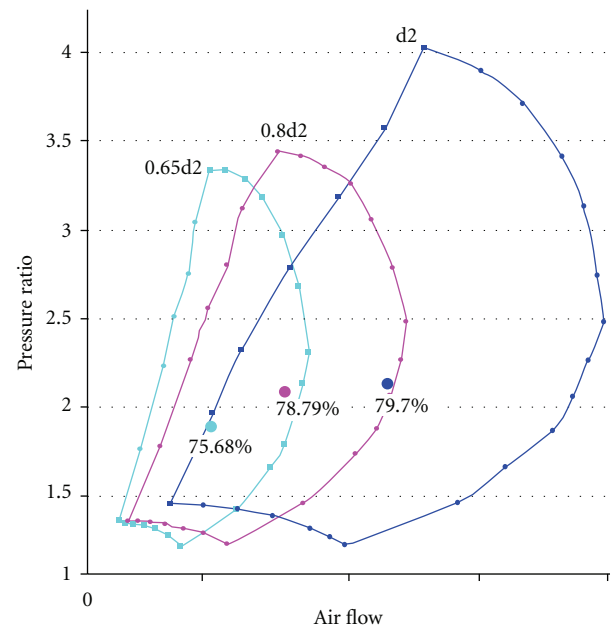


FIGURE 23: Performance characteristics of an impeller diameter cut.

and manufacturers' experience and their understanding of the stall and surge. Rotating stall and surge are violent limit cycle-type oscillations in compressors, which result when perturbations (in flow velocity, pressure, etc.) become unstable. Originally treated separately, these two phenomena are now recognized to be coupled oscillation modes of the compression system—surge that is the zeroth order or planar oscillation mode, while a rotating stall is the limit cycle resulting from higher-order, rotating-wave disturbances, as shown in Figure 24. The compressor normally starts with a stall and then eventually become a surge, as shown in Figure 25. During the surge, the compressor can experience a reversing flow. System resistance releases after the flow reversal, and the flow starts flowing into the system. This surge cycle continues, as shown in Figure 25. The pressure variation rate with the mass flow rate variation is much larger

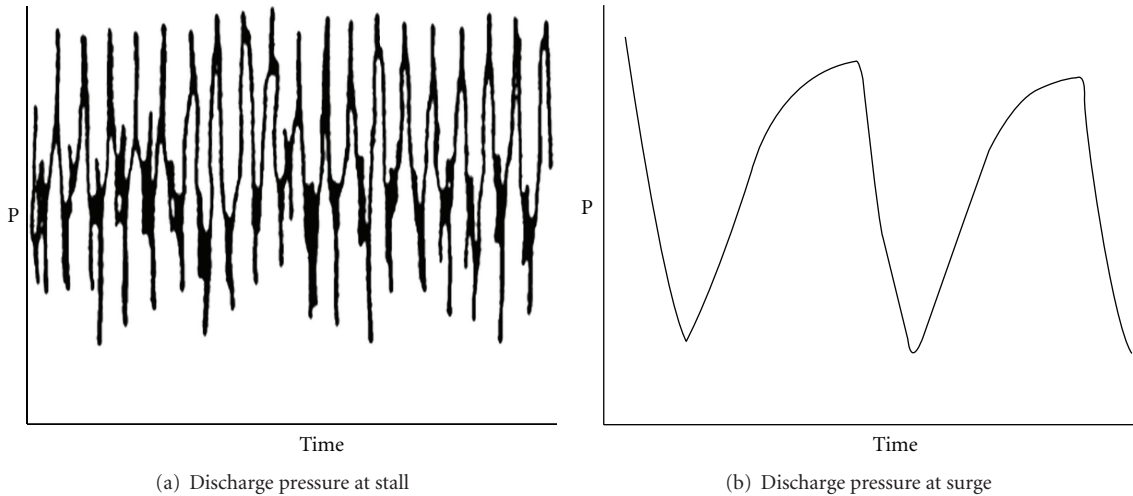


FIGURE 24: Stall and surge pressure variation with time.

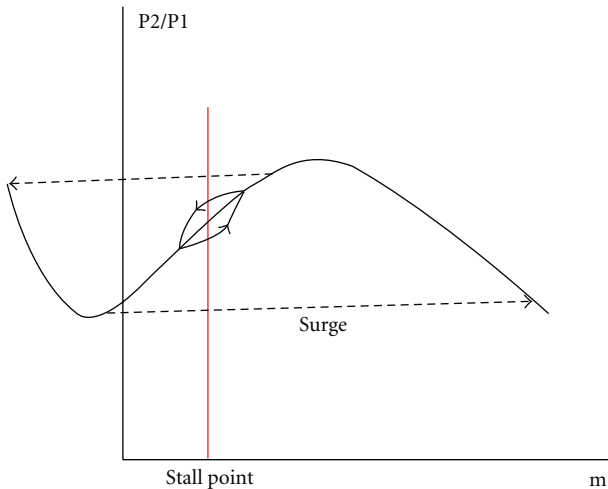


FIGURE 25: Surge of the centrifugal compressor.

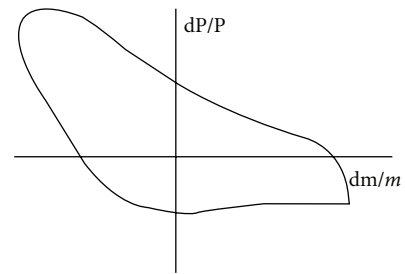


FIGURE 26: Variation of mass flow rate versus pressure fluctuations.

than the near choke, as shown in Figure 26. To extend the surge margin, it is important to optimize the impeller, the vaned diffuser, the vaneless diffuser, and the volute design. The surge control can extend the surge margin further. The simplest the way is to have a bypass surge relief valve. When the centrifugal compressor pressure rises beyond a certain level, the valve bypasses the flow from the discharge to the inlet to prevent surge. A wise valve choice can help engineers pay for the rest of an advanced surge-control system without exceeding the budget. The valve needs to have a fast stroking speed when open, high capacity, low noise, and a very stable throttling control. For example, the oil and gas industry often chooses high-performance rotary valves.

Casing treatments are other popular methods to extend the centrifugal compressor range. One of the key casing treatments is a ported shroud casing, as shown in Figure 27. The ported shroud design is entirely passive, having no moving parts, control valves, and so forth. The ported slot can be

vertical to the inlet flow or angled, as shown in Figures 27(a) and 27(b). There are vanes or ribs to support the stationary shroud in the leading edge inducer region. The vanes or ribs are not only a support structure but also an aerodynamic device to the flow inside the port, bleeding out with minimum losses. The ported shroud passage provides the bleed path when the compressor is near the surge, as shown in Figure 28(a) and also a secondary air inlet to the impeller when the compressor needs more air, as shown in Figure 28(b). The vanes or ribs in the passage are tangentially slanted in the direction of the impeller rotation, to preferentially augment the airflow into the impeller at high speed, while in part-speed discouraging the airflow out of the impeller through the secondary inlet. The advantage of the ported shroud can increase in the part-load surge margin and increase the choke flow at full load, as shown in Figure 29. It can be seen that for a ported shroud compressor, at a lower mass flow the pressure ratio increases. This is because the separation and reverse flow were reduced near the inducer compared with an unported case. When the compressor is near choke, the impeller can bypass the impeller throat and draw an extra flow from the port, as shown in Figure 28(b). Figure 30 shows that the flow passed the port at different impeller mass flow conditions when the port width and location were optimized to have the best surge margin for a gas width equal to  $bg$ .

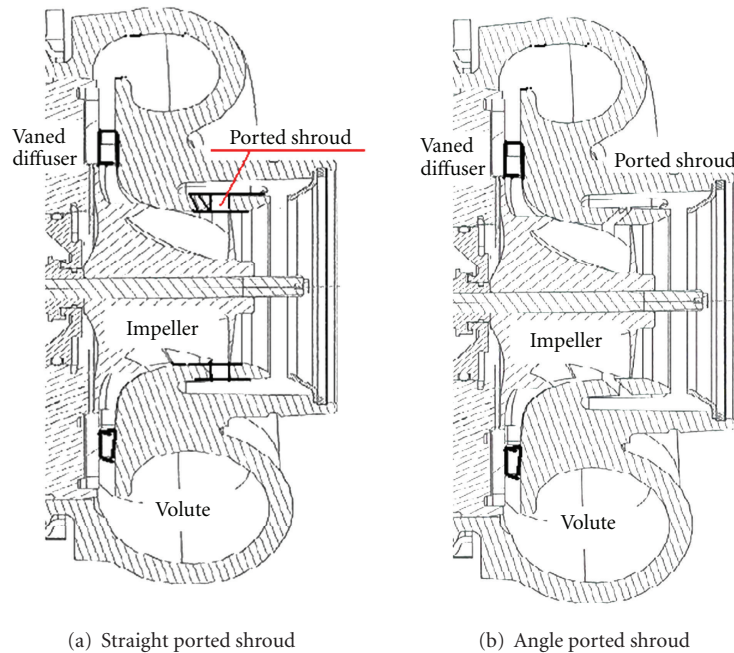


FIGURE 27: Ported shroud compressor.

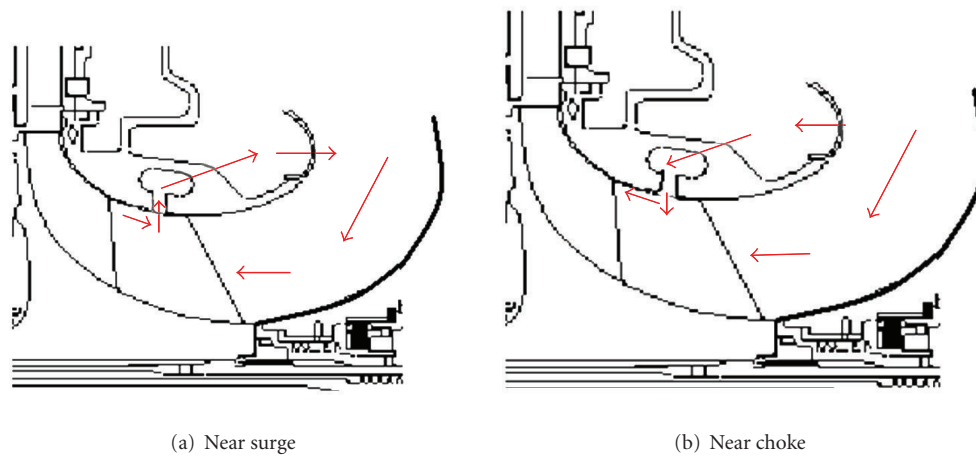


FIGURE 28: Ported shroud flows.

It can be seen that the port recirculation flow increases when the compressor mass flow reduces. The port can pass as much as 40% of the impeller design flow. It can be seen from Figure 30 that the port recirculation flow reduces when the port width reduces. Figure 31 is the port width affecting the compressor performance for a ported compressor with the port location at 16% of the shroud meridional length from the impeller inducer. It can be seen that when the port location is fixed, the port width increases from 0 to  $0.6b_2$ , and both the surge margin and choke margin increase. The compressor adiabatic efficiency remains almost unchanged until the port width is larger than  $0.1b_2$ . The efficiency drops almost negligibly up to a port width larger than  $0.2b_2$ . Figure 31 also shows that the angle port (70 degree

with axial direction) has an advantage compared with a straight port. The port design goal is to improve the surge and choke margin without greatly affecting the compressor performance. In some applications, for example, the automobile and aviation industry, the surge margin, and choke margins are both defined by certain efficiency levels. If the efficiency is too low, the system cannot perform properly. For those applications, the ported shroud applications are very popular. The ported shroud not only can extend the operational margin but also can improve the efficiency near the choke and surge. For those applications, the compressor map for a ported shroud demonstrated more advantages than an unported compressor, as shown in Figure 32.

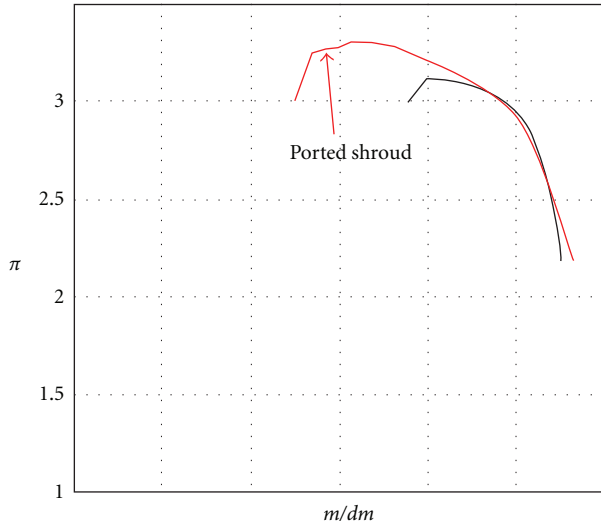


FIGURE 29: Compressor characteristic with and without ported shroud.

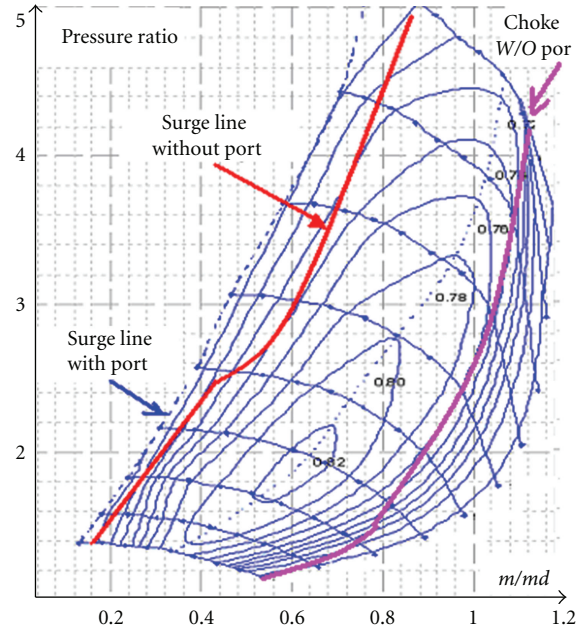


FIGURE 32: Ported shroud compressor map.

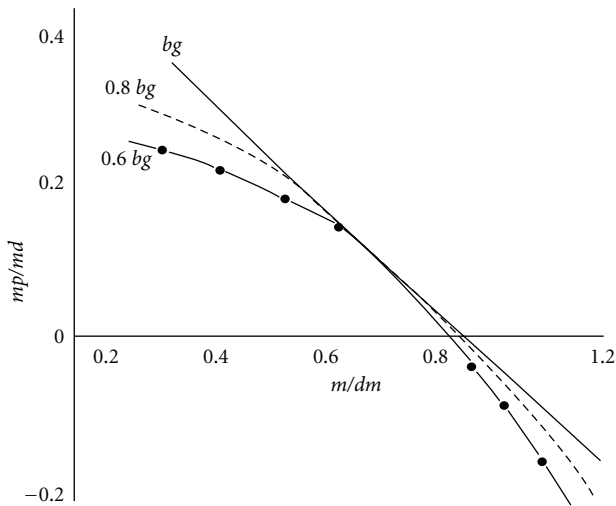


FIGURE 30: Flow inside bleed out from the port.

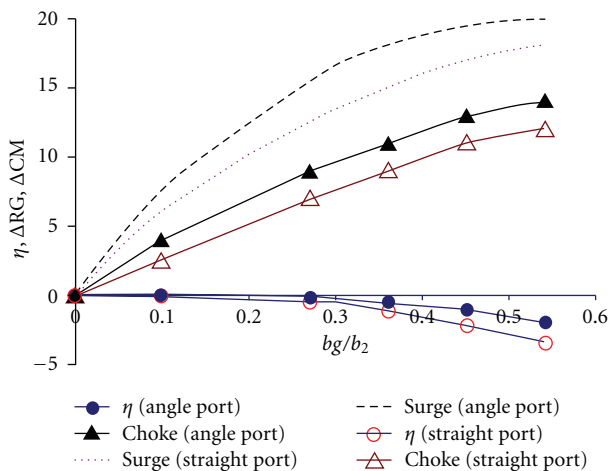


FIGURE 31: The compressor performance versus port width.

### 9. Conclusions

This paper provides several empirical consideration points in designing centrifugal compressors, focusing on the impeller design.

- (1) The different structure split compressors are discussed.
- (2) In an initial stage of compressor design, selections of the impeller inlet and the outlet velocity vectors and choice of blade numbers are the key initial design decisions.
- (3) Leaning the blades creates a back sweep and retains purely radial fibers, which are beneficial for bending moments. Experience showed that impellers with a back sweep generally have high efficiency. But lean blade design needs to consider the impacts of the impeller structure.
- (4) The velocity profile through the impeller blades largely depends on the flow Reynolds number. For low Reynolds number flows, the exit velocity profiles are almost parabolic and only with a small portion of the flat profile. For high Reynolds number flows, the exit velocity profiles have large flat profiles.
- (5) The tip clearance affects the overall compressor performance because it increases the magnitude of the secondary flow inside the impeller blades and produces strong tip vortices.
- (6) The tip clearance setting depends on the compressor's maximum surplus value. There are several methods to reduce the tip clearance losses. A variable tip clearance is one of the potential designs.

- (7) Compressor impeller flow cuts are widely used by compressor manufacturers. Some performance impacts need to be considered for doing the flow cut.
- (8) The ported shroud compressor has advantages for the compressor performance. Many new ported shroud structures have been proposed by many compressor manufactures [24]. But some fundamentals discussed in this paper can help designers to make the right decisions.

## Nomenclature

$B_2, b_2$ : Impeller tip width (m)  
 $C_1$ : Inlet axial velocity (m/s)  
 $C_p$ : Pressure coefficient =  $p/(0.5\rho d_2 U_2^2)$   
 CM: Choke margin  
 DF: Diffusion factor  
 $D_s$ : Specific diameter  
 dm: Flow fluctuations (kg/s)  
 dp: Pressure fluctuations (pa)  
 F: Function  
 f: Friction factor  
 H: Head (m)  
 ICFM: Cubic foot per minute at inlet  
 K: Sand grain roughness ( $\mu\text{m}$ )  
 L: Blade meridional length (m)  
 m: Mass flow rate (kg/s)  
 N: Rotational speed (RPS)  
 r: RMS radius (m)  
 Re: Reynolds number  
 ICFM: Compressor inlet flow in ft/min.  
 M: Mach number  
 MR: Mach number ratio  
 Mu: Head coefficient =  $H/(D_2 N)^2$   
 Q: Volume metric flow rate ( $\text{m}^3/\text{s}$ )  
 RG: Operating range =  $(Q_c - Q_s)/Q_c$   
 RMS: Root mean square  
 u, v: Velocities (m/s)  
 V: Velocity vector  
 W: RMS-relative velocity (m/s)  
 x, y: Cartesian coordinates.

## Greek Symbols

$\mu$ : Viscosity ( $\text{pa}\cdot\text{s}$ )  
 $\varphi$ : Flow coefficient =  $Q/(ND^3)$   
 $\eta$ : Adiabatic efficiency (total to static) =  $(\pi^{(\gamma-1/\gamma)} - 1)/(T_2/T_{01} - 1)$   
 $\Psi$ : Head coefficient =  $h/u_2^2$   
 $\pi$ : Pressure ratio  
 $\gamma$ : Specific heat ratio.

## Subscripts

1, 2: Impeller inlet and exit  
 C: Chock or clearance

l: Loss  
 0: Zero clearance  
 ref: Reference  
 S: Surge.

## References

- [1] M. P. Singh and J. J. Vargo, "Reliability evaluation of shrouded blading using the SAFE interference diagram," *Journal of Engineering for Gas Turbines and Power*, vol. 111, no. 4, pp. 601–609, 1989.
- [2] D. P. Kenny, The history and future of the centrifugal compressor in aviation gas turbine, SAE/SP-804/602, 1984.
- [3] P. D. Collopy, "Surplus value in propulsion system design optimization," AIAA-97-3159, 1997.
- [4] D. Japikse, "Decisive factors in advanced centrifugal compressor design and development," in *Proceedings of the International Mechanical Engineering Congress & Exposition (IMEchE '00)*, November 2000.
- [5] C. Xu and R. S. Amano, "Development of a low flow coefficient single stage centrifugal compressor," *International Journal of Computational Methods in Engineering Science and Mechanics*, vol. 10, no. 4, pp. 282–289, 2009.
- [6] C. Rodgers and L. Sapiro, "Design considerations for high-pressure ratio centrifugal compressor," 72-GT-71, 1972.
- [7] R. H. Aungier, *Centrifugal Compressors—A Strategy for Aerodynamic Design and Analysis*, ASME Press, New York, NY, USA, 2002.
- [8] C. Xu, "Design experience and considerations for centrifugal compressor development," *Proceedings of the Institution of Mechanical Engineers, Part G*, vol. 221, no. 2, pp. 273–287, 2007.
- [9] C. Xu and R. S. Amano, "A hybrid numerical procedure for cascade flow analysis," *Numerical Heat Transfer, Part B*, vol. 37, no. 2, pp. 141–164, 2000.
- [10] C. Xu and R. S. Amano, "Flux-splitting finite volume method for turbine flow and heat transfer analysis," *Computational Mechanics*, vol. 27, no. 2, pp. 119–127, 2001.
- [11] C. Xu and R. S. Amano, "Computational analysis of pitch-width effects on the secondary flows of turbine blades," *Computational Mechanics*, vol. 34, no. 2, pp. 111–120, 2004.
- [12] C. Xu and R. S. Amano, "Numerical prediction of swept blade aerodynamic effects," in *Proceedings of ASME Turbo & Expo*, pp. 1–9, Vienna, Austria, June 2004, GT2004-53008.
- [13] C. Xu and R. S. Amano, "Computational analysis of swept compressor rotor blades," *International Journal of Computational Methods in Engineering Science and Mechanics*, vol. 9, no. 6, pp. 374–382, 2008.
- [14] C. Xu and R. S. Amano, "The development of a centrifugal compressor impeller," *International Journal of Computational Methods in Engineering Science and Mechanics*, vol. 10, no. 4, pp. 290–301, 2009.
- [15] C. Xu and R. S. Amano, "Computational analysis of scroll tongue shapes to compressor performance by using different turbulence models," *International Journal of Computational Methods in Engineering Science and Mechanics*, vol. 11, no. 2, pp. 85–99, 2010.
- [16] C. Xu and R. S. Amano, "Study of the flow in centrifugal compressor," *The International Journal of Fluid Machinery and Systems*, vol. 3, no. 3, pp. 260–270, 2010.

- [17] H. Krain, B. Hoffmann, and H. Pak, "Aerodynamics of a centrifugal compressor impeller with transonic inlet conditions," in *Proceedings of the International Gas Turbine and Aeroengine Congress and Exposition*, June 1995, 95-GT-79.
- [18] H. Krain, "Flow in centrifugal compressor," von Karman Institute for Fluid Dynamics, Ls 17, 1984-07, 1984.
- [19] D. Japikse, *Centrifugal Compressor Design and Performance*, Concepts Eti, Wilder, Vt, USA, 1996.
- [20] C. Xu and R. S. Amano, "On the development of turbomachine blade aerodynamic design system," *International Journal of Computational Methods in Engineering Science and Mechanics*, vol. 10, no. 3, pp. 186–196, 2009.
- [21] E. Benini and A. Toffolo, "Centrifugal compressor of a 100 kW microturbine: part 2—numerical study of impeller-diffuser interaction," in *Proceedings of the ASME Turbo Expo*, pp. 699–705, June 2003, GT-2003-38153.
- [22] E. Benini and A. Toffolo, "Centrifugal compressor of a 100 kW microturbine: part 3—optimization of diffuser apparatus," in *Proceedings of the ASME Turbo Expo*, pp. 707–714, June 2003, GT-2003-38154.
- [23] J. Hoffren, T. Siikonen, and S. Laine, "Conservative multiblock Navier-Stokes solver for arbitrarily deforming geometries," *Journal of Aircraft*, vol. 32, no. 6, pp. 1342–1350, 1995.
- [24] T. Siikonen, "An application of Roe's flux-difference splitting for k- $\epsilon$  turbulence model," *International Journal for Numerical Methods in Fluids*, vol. 21, no. 11, pp. 1017–1039, 1995.
- [25] M. M. Rai, "A relaxation approach to patched-grid calculations with the euler equations," *Journal of Computational Physics*, vol. 66, no. 1, pp. 99–131, 1986.
- [26] S. Niazi, A. Stein, and L. N. Sankar, "Development and application of a CFD solver to the simulation of centrifugal compressors," AIAA paper 98-0934, 1998.
- [27] W. Jansen, "Rotating stall in a radial vaneless diffuser," *ASME Journal of Basic Engineering*, vol. 86, pp. 750–758, 1964.
- [28] Y. Senoo and Y. Kinoshita, "Influence of inlet flow conditions and geometries of centrifugal vaneless diffusers on critical flow angle for reverse flow," *ASME Journal of Fluids Engineering*, vol. 99, no. 1, pp. 98–103, 1977.
- [29] H. S. Dou and S. Mizuki, "Analysis of the flow in vaneless diffusers with large width-to-radius ratios," *ASME Journal of Turbomachinery*, vol. 120, no. 1, pp. 193–201, 1998.
- [30] S. Ljevar, H. C. de Lange, and A. A. van Steenhoven, "Two-dimensional rotating stall analysis in a wide vaneless diffuser," *International Journal of Rotating Machinery*, vol. 2006, Article ID 56420, 11 pages, 2006.
- [31] K. Iwakiri, M. Furukawa, S. Ibaraki, and I. Tomita, "Unsteady and three-dimensional flow phenomena in a transonic centrifugal compressor impeller at rotating stall," in *Proceedings of the ASME Turbo Expo*, pp. 1611–1622, June 2009, GT2009-59516.
- [32] E. M. Greitzer, "Review—axial compressor stall phenomena," *ASME Journal of Fluids Engineering*, vol. 102, no. 2, pp. 134–151, 1980.
- [33] M. T. Barton, M. L. Mansour, J. S. Liu, and D. L. Palmer, "Numerical optimization of a vaned shroud design for increased operability margin in modern centrifugal compressors," *ASME Journal of Turbomachinery*, vol. 128, no. 4, pp. 627–631, 2006.
- [34] ASME, Performance Test Code on Compressors and Exhausters, PTC 10-97, 1997.
- [35] R. S. Amano and B. Sunden, *Thermal Engineering in Power Systems*, WIT Press, 2008.
- [36] O. E. Balje, *Turbomachines*, John Wiley & Sons, New York, NY, USA, 1981.
- [37] K. Brun and R. Kurz, "Analysis of secondary flows in centrifugal impellers," *International Journal of Rotating Machinery*, vol. 2005, no. 1, pp. 45–52, 2005.
- [38] R. L. Street, G. Z. Watters, and J. K. Vennard, *Elementary Fluid Mechanics*, John Wiley & Sons, New York, NY, USA, 1996.
- [39] T. Wright, "Comments on compressor efficiency scaling with Reynolds number and relative roughness," in *Proceedings of the American Society of Mechanical Engineers*, June 1989, 89-GT-31.
- [40] P. R. N. Childs and M. B. Noronha, "The impact of machining techniques on centrifugal compressor impeller performance," in *Proceedings of the International Gas Turbine & Aeroengine Congress & Exposition*, June 1997, 97-GT-456.
- [41] C. Rodgers, "A diffusion factor correlation for centrifugal impeller stalling," 78-GT-61, 1978.
- [42] C. Xu and R. S. Amano, "A turbo machinery blade design and optimization procedure," GT-2002-30541, 2002.
- [43] D. P. Kenny, "The history and future of the centrifugal compressor in aviation gas turbine," SAE/SP-804/602, 1984.
- [44] R. van den Braembussche, "Rotating stall in centrifugal compressors," VKI Preprint 1987-16, 1987.

## Research Article

# Performance Improvement of a Centrifugal Compressor by Passive Means

**N. Sitaram<sup>1</sup> and S. M. Swamy<sup>1,2</sup>**

<sup>1</sup> *Thermal Turbomachines Laboratory, Department of Mechanical Engineering, Indian Institute of Technology Madras, Chennai 600 036, India*

<sup>2</sup> *Department of Mechanical Engineering, GNITS, Shaikpet, Hyderabad 500 008, India*

Correspondence should be addressed to N. Sitaram, nsitaram@iitm.ac.in

Received 14 January 2012; Revised 15 April 2012; Accepted 15 April 2012

Academic Editor: Ashwani K. Gupta

Copyright © 2012 N. Sitaram and S. M. Swamy. This is an open access article distributed under the Creative Commons Attribution License, which permits unrestricted use, distribution, and reproduction in any medium, provided the original work is properly cited.

The present experimental investigation deals with performance improvement of a low-speed centrifugal compressor by inexpensive passive means such as turbulence generator placed at different positions and partial shroud near the rotor blade tip. The experiments are carried out at three values of tip clearance, namely 2.2%, 5.1%, and 7.9% of rotor blade height at the exit. Performance tests are carried out for a total of 13 configurations. From these measurements, partial shroud is found to give the best performance. The improvement in the compressor performance may be due to the reduction of tip leakage flows by the small extension of partial shroud (2 mm on the pressure surface side). Although there is nominal change in performance due to turbulence generator (TG), TG has beneficial effect of increased operating range.

## 1. Introduction

The centrifugal compressors have a wide range of applications especially for power plants for small aircraft and helicopters, in process industries, compression of gases and vapours, and refrigeration, because they can provide high-pressure ratios and large operating ranges with relatively high efficiencies. Centrifugal compressors are used primarily for their suitability for handling small volume flows, but other advantages include a shorter length than an equivalent axial flow compressor, less susceptibility to loss of performance by buildup of deposits on the blade surfaces, and their suitability to operate over a wide range of mass flow. The efficiency of a centrifugal compressor is lower than that of an axial flow compressor. Efficiency is probably the most important performance parameter for turbomachines. The conditions of flow in the tip region of rotor blades are very complex due to strong interaction of the leakage flow with the boundary layers and secondary flows. The tip leakage flow thus would have dominant effect on the performance of a compressor. A comprehensive review of tip clearance effects in centrifugal compressors is given by Pampreen [1]. Senoo

and Ishida [2] gave analytical expression to quantify the tip clearance effects in centrifugal blowers. Senoo [3] gave a comprehensive review of mechanics of tip leakage flows in axial and centrifugal compressors. Ishida et al. [4] had tested centrifugal blowers with different shapes (square, round, and E-type, i.e., with an extension on the pressure surface side) and found that E-type tip provided improved performance. The concept of partial shrouded rotor in a small high-speed high-pressure ratio centrifugal compressor was computationally investigated by Tang et al. [5]. They found that the leakage flow was reduced in the partially shrouded rotor. Recently, Akturk and Camci [6] measured three-dimensional mean flow near the tip of a ducted axial fan rotor using a stereoscopic particle image velocimeter. A number of novel tip treatments based on custom-designed pressure side extensions were tested to mitigate tip leakage flow. The chordwise location and the width of the extension in the circumferential direction are systematically varied. Tip platform extensions near the rotor blade trailing edge were found to show the best tip treatment performance. They [7, 8] further carried out computational and experimental investigations on additional tip treatments. Kameier and

TABLE 1: Design details of the rotor.

Total pressure rise, $\Delta p$	300 mm WG
Volume flow rate, $V$	1.12 m <sup>3</sup> /s
Speed of rotation, $N$	2000 rpm
Shape number, $N_{sh}$	0.092
No. of rotor blades, $Z$	16
Inducer hub diameter, $d_{1h}$	160 mm
Inducer tip diameter, $d_{1t}$	300 mm
Rotor tip diameter, $d_2$	500 mm
Blade height at the exit, $h_2$	32.5 mm
Blade thickness	3 mm
Blade angle at inducer tip, $\beta_{1t}$	35°
Blade angle at inducer hub, $\beta_{1h}$	53°
Blade angle at exit, $\beta_2$	
(a) At hub: 75°	
(b) At mean section: 90°	
(c) At tip: 105°	
All the angles are measured w. r. t. tangential direction	

Neise [9] had used Velcro tape in the radial clearance of an axial compressor to improve its aerodynamic and acoustic performance. Sitaram and Thakar [10] had applied this technique in a low aspect ratio axial fan and found that its performance was improved, even though the Velcro tape was placed upstream of the rotor. Any simple passive means to improve the efficiency and operating range of centrifugal compressors is very useful. The present investigation is undertaken with the objective of testing the efficacy of inexpensive passive means, such as turbulence generator (TG) and partial shrouds (PSs) to achieve increased operating range and efficiency of a centrifugal compressor. These passive devices are tested individually and in combination to arrive at the best combination.

## 2. Experimental Facility, Passive Means, and Instrumentation

**2.1. Experimental Facility.** The present experimental investigations are carried out on a low-speed centrifugal compressor setup available in Thermal Turbomachines Laboratory, Department of Mechanical Engineering, Indian Institute of Technology Madras. A schematic layout of the experimental setup is shown in Figure 1. The experimental set up consists of essentially a centrifugal rotor driven by a 5 kW D.C. motor with a rated speed of 2000 rpm. The D.C. motor is directly coupled to the shaft carrying the rotor.

The main components of the compressor are suction duct, rotor, vaneless diffuser formed by the front and rear walls of the casing and volute casing of circular cross-section, and a delivery duct with a throttle at its outlet and nozzle at the inlet. The major design details of the compressor are given in Table 1.

**2.2. Passive Means.** Two inexpensive passive means, namely, turbulence generator and partial shrouds, are used in the

TABLE 2: Configurations tested.

$\tau$ (%)	2.2%	5.1%	7.9%
Basic configuration (without passive device)	Config. 1	Config. 9	Config. 12
With TG only	Config. 3	Config. 10	Config. 11
With PS only	Config. 6	Config. 7	Config. 14
With TG + PS	Config. 5	Config. 8	Config. 15
With TG* only	Config. 2	—	—
With TG** + TG	Config. 4	—	—
With TG*** only	—	—	Config. 13

TG: turbulence generator on the casing at 15 mm upstream of inducer tip leading edge.

TG\*: turbulence generator on the casing at 30 mm upstream of inducer tip leading edge.

TG\*\*: turbulence generator on the hub at 30 mm upstream of inducer hub leading edge.

TG\*\*\*: turbulence generator on the casing at 400 mm dia.

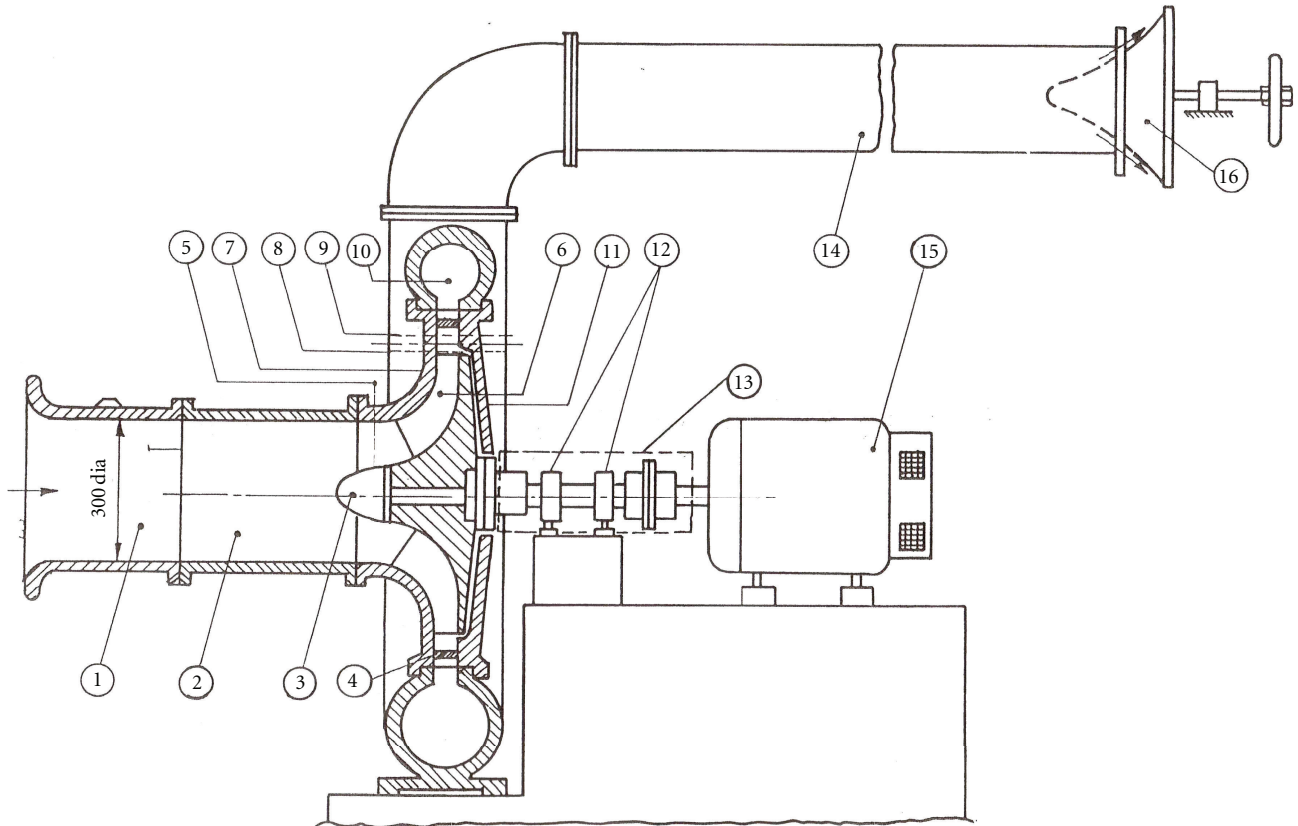
PS: partial shrouds on the tip of the blade.

present investigation. The details of the passive means are given below.

**Turbulence Generator.** Turbulence generator is used in the experiment as a tripping device for the generation of turbulent boundary layers. A turbulence generator (TG) is attached to the inside of the suction duct upstream of the rotor. The turbulence generator (TG) is made of Velcro tape. The Velcro tape is attached to the inside of the suction duct. The axial width of Vecro tape is 10 mm, the length is 942.5 mm, and the thickness is 2 mm. A mild steel ring of 16 mm axial width, 3 mm thickness, and 930 mm length was used to fix the Velcro tape to the suction duct. A layer of Araldite of very small thickness was used between the tape and the casing wall to attach the tape. The ring exerted uniform circumferential pressure all around the tape. The extra Araldite came out of the gap between the suction duct wall and the Velcro tape and removed. It was observed that the time taken for the Araldite to harden was minimized and the thickness of hardened Araldite was more or less uniform. Also, there was no sag of Velcro tape, and there was no gap between Velcro tape and suction duct.

**Partial Shrouds.** The partial shrouds were made of stainless steel shims of 0.1 mm thickness. The stainless steel shim was cut to the shape of rectangle pieces of 50 mm  $\times$  5 mm size. These rectangle pieces were pasted on the tip of the blades using an extremely thin layer of Araldite.

Various configurations were obtained by combining TG and PS. Performance of the configurations with these configurations was measured and compared at three values of tip clearance, namely, 2.2%, 5.1%, and 7.9% of rotor blade height at the exit. The details of the configurations tested are given in Table 2 and shown in Figure 2. The blade-to-blade view showing the partial shroud on the rotor blade tip is also shown in Figure 2.



- |                                 |                                 |
|---------------------------------|---------------------------------|
| (1) Inlet nozzle                | (9) Position of probe at exit 2 |
| (2) Suction duct                | (10) Volute casing              |
| (3) Bullet nose                 | (11) Diffuser hub               |
| (4) Spacers                     | (12) Bearing housings           |
| (5) Position of inlet probe     | (13) Bearing housing cover      |
| (6) Rotor                       | (14) Delivery duct              |
| (7) Diffuser shroud             | (15) D. C. motor                |
| (8) Position of probe at exit 1 | (16) Throttle                   |

FIGURE 1: Schematic diagram of centrifugal compressor setup.

**2.3. Instrumentation.** The performance of the compressor was determined by the change in the static pressure across the compressor. The static pressures on the suction duct and delivery duct were measured using a scanning box (Model FC091-3) and micromanometer (Model FCO12) manufactured by M/s Furness Control Ltd., Bexhill, UK. The scanning box contained 20 valves, which are numbered sequentially. The pressures to be measured were connected to the numbered inputs. Pressure inputs were read in sequence by using the micromanometer. The micromanometer is a sensitive differential pressure measuring unit, capable of reading air pressures from 0.01 mm to 2000 mm WG. It

would respond to pressure inputs up to 50 Hz. But the time constant potentiometer can be used to average the pressure fluctuations.

The speed of the centrifugal compressor was measured using a noncontact type digital tachometer. Four interconnected static pressure tappings on the inlet bell mouth casing wall at the throat section were used to determine the inlet velocity. Knowing the bellmouth area, the volume flow was calculated using a suitable value of coefficient of discharge for the bellmouth. A D.C. motor with a separate exciter is used to drive the rotor of the centrifugal compressor. The input power was measured by means of voltmeters



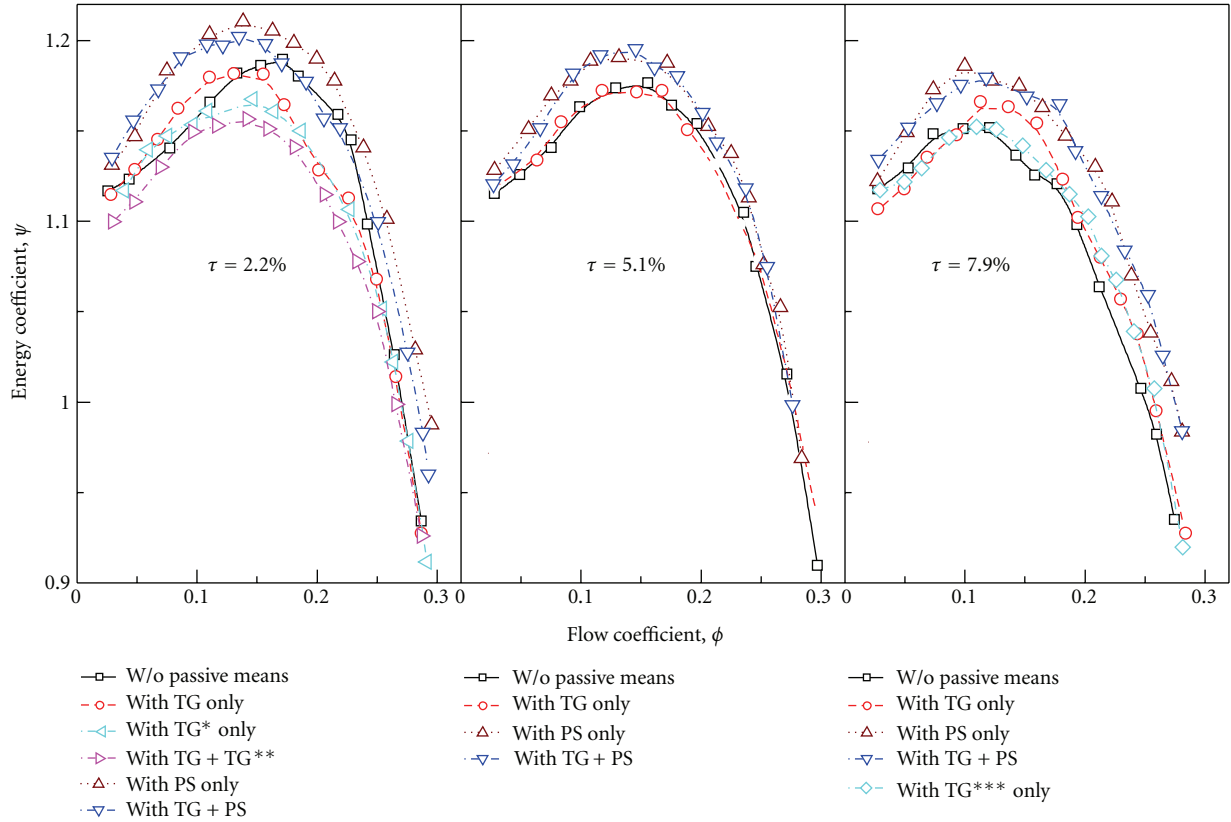


FIGURE 3: Performance characteristics of the centrifugal compressor ( $\psi$  versus  $\phi$ ): effect of configuration.

of clearance of 7.9%, appreciable increase in  $\psi$  is achieved, with a small increase in stable operating range. The effect of TG\*\*\* placed in the clearance at a diameter of 400 mm is negligible. TG had shown beneficial effects on the performance of axial rotors [9, 10]. The low momentum fluid in the casing wall boundary layer is energized by the TG. In centrifugal rotors, although the low momentum fluid is energized by TG, the boundary layer travels through a highly curved channel. So TG may not have substantial impact on the performance. However, at the higher value of tip clearance, some beneficial effects are observed.

The effect of the partial shroud is to improve the compressor performance, in terms of increased  $\psi$  and  $\eta$ , at the three values of tip clearance tested. The value of  $\phi$  where  $\psi_{\max}$  occurs is reduced, thereby increasing stable operating range. Although performance is measured up to the maximum volume flow, for the sake of clarity of presentation, performance curves for all  $\psi$  versus  $\phi$  curves are limited to  $\phi = 0.30$ . However, for  $\eta$  versus  $\phi$  curves (Figure 4), complete range of performance is presented, that is, up to the maximum value of  $\phi$  of 0.40. The values of  $\psi_{\max}$  and  $\phi$  where  $\psi_{\max}$  occurs for all configurations are given in Table 3. The trends of performance curves  $\eta$  versus  $\phi$  are similar to those of  $\psi$  versus  $\phi$  curves. Configurations with PS clearly show higher efficiencies as much as 5%. Because of the extension of the partial shroud, the tip leakage flow has to travel a longer distance before interacting with the main

flow. The contraction coefficient across the tip clearance reduces, reducing the tip leakage flow and losses. Hence, both performance and efficiency of the rotor with partial shroud are improved compared to those for the rotor without partial shroud. The tip leakage flow is stronger near the exit of the rotor, due to higher loading. Hence, partial shroud on the rotor in this region has substantial effects. The present experiments are carried out with one configuration of partial shroud. There is further scope to experiment with length and width of the partial shroud to arrive at the best partial shroud.

The most important performance parameters showing the effect of configuration are presented in Table 3. It can be concluded that partial shroud has beneficial effects on the performance of the compressor, whereas the effect of TG is nominal, except at higher value of tip clearance. In the present experiments, partial shroud with a very small extension of 2 mm on the pressure surface side of the rotor blade is provided. The possible reason for the improvement in the compressor performance due to this small extension may be the reduction of tip leakage flows, due to reduction of contraction coefficient.

It must be emphasized here that the performance presented above includes not only losses in the rotor but also losses in the diffuser, volute, and downstream duct with  $90^\circ$  bends.

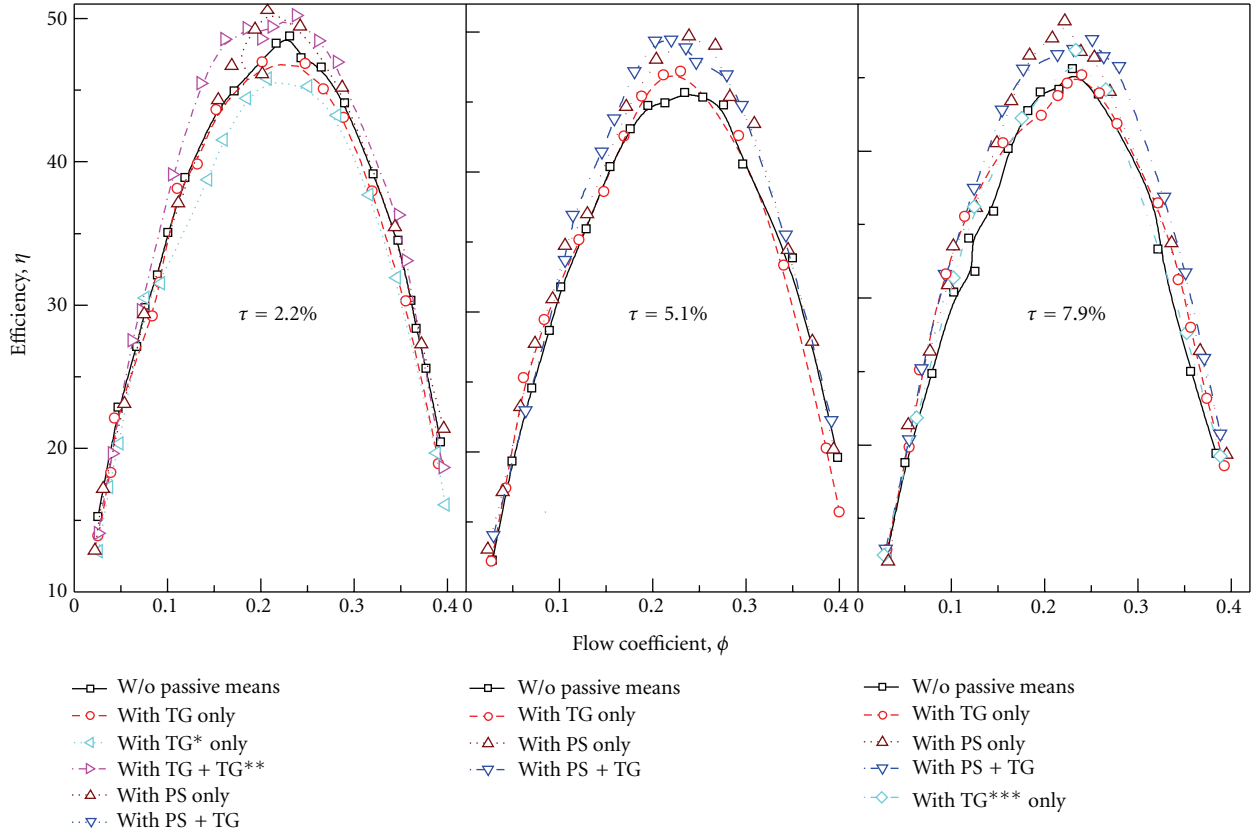


FIGURE 4: Performance characteristics of the centrifugal compressor ( $\eta$  versus  $\phi$ ): effect of configuration.

TABLE 3: Effect of configuration on performance.

$\tau$ (%)	Details of configuration	$\psi_{\max}$	$\phi$ at $\psi_{\max}$	$\eta$ at $\psi_{\max}$	$\eta_{\max}$	$\phi$ at $\eta_{\max}$
2.2	Without passive means	1.188	0.169	44.5	47.1	0.217
2.2	TG* only	1.173	0.124	39.0	48.2	0.262
2.2	TG only	1.191	0.132	38.8	47.6	0.250
2.2	TG + TG**	1.156	0.143	37.8	45.7	0.217
2.2	TG + PS	1.205	0.135	40.0	50.0	0.207
2.2	PS only	1.204	0.139	44.8	49.7	0.237
5.1	Without passive means	1.173	0.156	39.9	45.4	0.237
5.1	TG only	1.172	0.121	34.7	48.0	0.250
5.1	PS only	1.186	0.109	34.6	49.4	0.241
5.1	TG + PS	1.192	0.146	40.9	49.3	0.237
7.9	Without passive means	1.153	0.121	31.9	45.5	0.230
7.9	TG only	1.167	0.113	35.2	44.9	0.241
7.9	PS only	1.185	0.101	33.5	48.6	0.222
7.9	TG + PS	1.170	0.128	33.9	46.8	0.248
7.9	TG***	1.157	0.124	38.5	45.2	0.225

3.2. *Effect of Tip Clearance.* In order to determine the effect of tip clearance on the performance of the compressor with and without passive means, the performance curves in terms of  $\psi$  versus  $\phi$  and  $\eta$  versus  $\phi$  are replotted for the four configurations, namely, without passive means, with TG only, with PS only, and with TG + PS for the three values of tip clearances tested, that is,  $\tau = 2.2\%$ ,  $5.1\%$ , and  $7.9\%$ .

The  $\psi$  versus  $\phi$  curve (Figure 5) shows that the operating range of the compressor is increased, for the basic configuration, as the tip clearance is increased. Similar results are observed in a low-speed radial tipped centrifugal compressor [11] and a high-speed centrifugal compressor [12]. The effect of passive means (i.e., TG, PS, and TG + PS) is to reduce this trend. For both configurations, TG and TG + PS,  $\psi_{\max}$  occurs

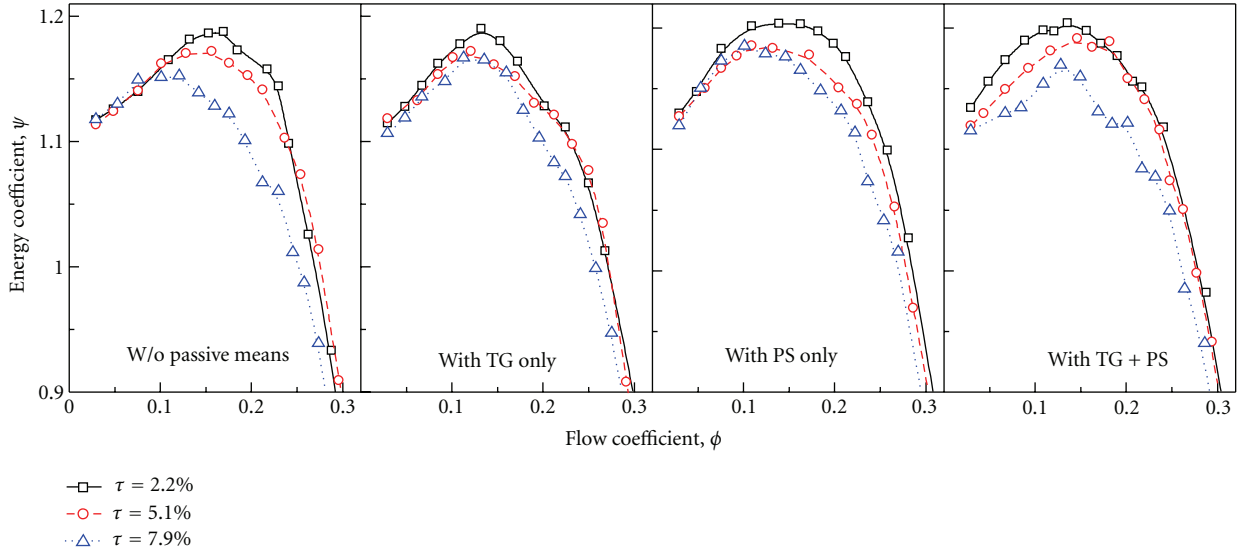


FIGURE 5: Performance characteristics of the centrifugal compressor ( $\psi$  versus  $\phi$ ): effect of tip clearance.

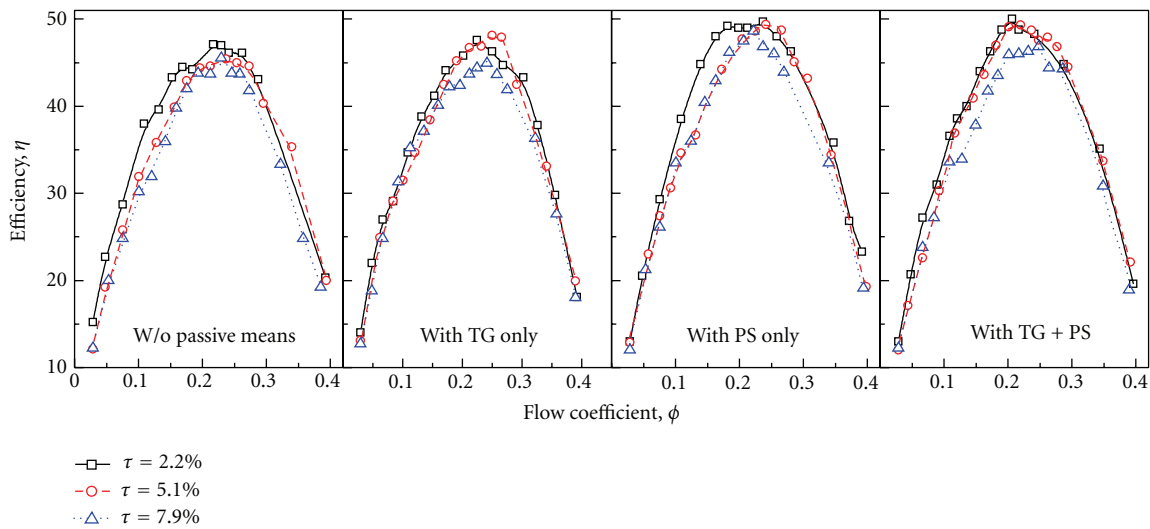


FIGURE 6: Performance characteristics of the centrifugal compressor ( $\eta$  versus  $\phi$ ): effect of tip clearance.

at nearly the same flow coefficient for the three clearances tested. However, for configuration with PS, this benefit is not much pronounced. Thus, it can be concluded that TG has a beneficial effect of increased operating range, at lower value of tested clearance, although there is nominal change in  $\psi$  and  $\eta$ . The trends of  $\eta$  versus  $\phi$  curves (Figure 6) are similar to those of  $\psi$  versus  $\phi$  curves. Efficiency decreases with increase in tip clearance. The decrease in efficiency is as much as 5% for basic configuration, whereas it is smaller for other configurations with passive means.

The effect of tip clearance on the most important performance parameters is presented in Table 4 and Figure 7. From the figure, it is evident that both PS and TG + PS configurations give higher energy coefficient compared to basic and TG configurations. Although TG configuration

gives nearly the same value of energy coefficient (except at  $\tau = 7.9\%$ ) compared to the basic configuration, sensitivity of energy coefficient with tip clearance is reduced from  $\tau = 5.1\%$  onwards. Similar observation is made for TG + PS configuration compared with PS configuration. The value of  $\phi$  at maximum efficiency remains nearly constant with tip clearance. However, the value of  $\phi$  at maximum energy coefficient decreases with tip clearance. The value of  $\phi$  at maximum energy coefficient is maximum for basic configuration followed by TG + PS, TG, and PS configurations.

The efficiency at the maximum value of  $\psi$  is the lowest for basic configuration followed by TG, TG + PS, and PS configurations. However, the maximum efficiency is the highest for basic configuration followed by TG + PS, PS, and TG configurations.

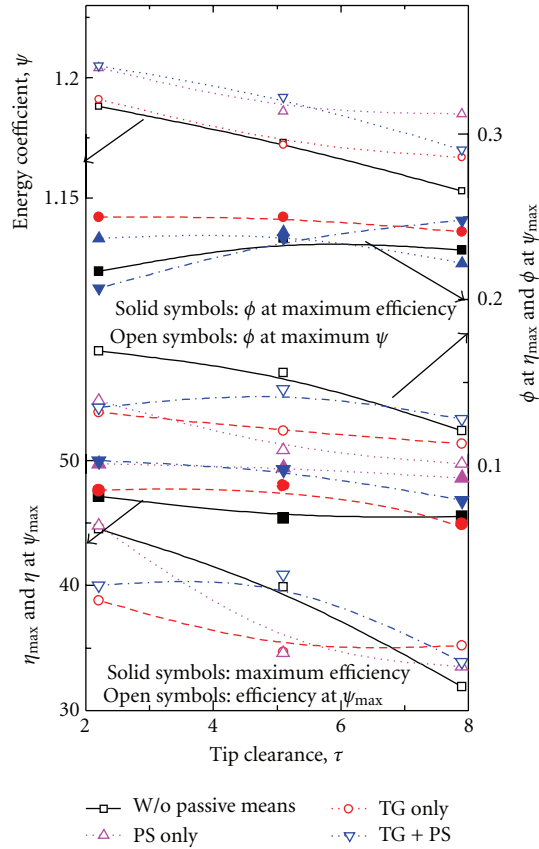


FIGURE 7: Effect of tip clearance on performance.

TABLE 4: Effect of tip clearance on  $\psi_{\max}$  and  $\eta_{\max}$ .

Details of configuration	$\tau$ (%)	$\psi_{\max}$	$\phi$ at $\psi_{\max}$	$\eta$ at $\psi_{\max}$	$\eta_{\max}$	$\phi$ at $\eta_{\max}$
Without passive means	2.2	1.188	0.169	44.5	47.1	0.217
	5.1	1.173	0.156	39.9	45.4	0.237
	7.9	1.153	0.121	31.9	45.5	0.230
TG only	2.2	1.191	0.132	38.8	47.6	0.250
	5.1	1.172	0.121	34.7	48.0	0.250
	7.9	1.167	0.113	35.2	44.9	0.241
PS only	2.2	1.204	0.139	44.8	49.7	0.237
	5.1	1.186	0.109	36.6	49.4	0.241
	7.9	1.185	0.101	33.5	48.6	0.222
TG + PS	2.2	1.205	0.135	40.0	50.0	0.207
	5.1	1.192	0.146	40.9	49.3	0.237
	7.9	1.170	0.128	33.9	46.8	0.248

#### 4. Conclusions

The following major conclusions are drawn from the present investigation.

- (1) Configurations with partial shroud (PS) show higher energy coefficient and efficiency compared to other configurations. Partial shrouds have beneficial effects on increasing energy coefficient and efficiency of compressor.
- (2) Other configurations, namely, TG and TG + PS, also have beneficial effects on the performance of the compressor. However, configurations TG\*, TG + TG\*\*, and TG\*\*\* have detrimental effects on the performance of the compressor.
- (3) Configuration 12 (basic configuration at  $\tau = 7.9\%$ ) gives poor performance, that is, reduced operating range, reduced energy coefficient and efficiency over the entire operating range.

- (4) Turbulence generator (TG) has nominal effects on the energy coefficient and efficiency of the compressor. However, the operating range of the compressor is substantially increased.
- (5) The sensitivity of energy coefficient from  $\tau = 5.1\%$  onwards is reduced for TG configurations.

## Nomenclature

$b$ :	Distance between the shroud and hub at the rotor exit (m)
$C_d$ :	Velocity in delivery duct (m/s)
$C_s$ :	Velocity in suction duct (m/s)
$d$ :	Rotor diameter (m)
$N$ :	Rotational speed of rotor (rpm)
$N_c$ :	Coupling power (Watt)
$N_{sh}$ :	Shape number = $N\sqrt{V/W^{3/4}}$
$P_d$ :	Delivery pressure (Pa)
$P_s$ :	Suction pressure (Pa)
TG:	Turbulence generator placed on the casing at 15 mm upstream the inducer leading edge
TG*:	Turbulence generator placed on the casing at 30 mm upstream the inducer leading edge
TG**:	Turbulence generator placed on the hub at 30 mm upstream of the inducer leading edge
TG***:	Turbulence generator placed on the casing at 400 mm diameter
$t$ :	Rotor blade clearance (m)
$U$ :	Rotor tip speed = $(\pi dn/60)$ (m/s)
$V$ :	Volume flow rate ( $m^3/s$ )
$W$ :	Specific work ( $m^2/s^2$ )
$\phi$ :	Flow coefficient (defined in the text)
$\gamma$ :	Power coefficient (defined in the text)
$\eta$ :	Efficiency (defined in the text)
$\psi$ :	Energy coefficient (defined in the text)
$\rho$ :	Density of air ( $kg/m^3$ )
$\tau$ :	Tip clearance as a percentage of rotor blade height at exit = $(t/b_2) \times 100$ .

## Subscript

2: Tip.

## Acknowledgments

The authors would like to thank the faculty, technical staff and administrative staff, of Thermal Turbomachines Laboratory for their help and encouragement during the course of the present investigation.

## References

- [1] R. C. Pampreen, "Small turbomachinery compressor and fan aerodynamics," *Journal of Engineering for Power*, vol. 105, no. 2, pp. 251–256, 1983.
- [2] Y. Senoo and M. Ishida, "Deterioration of compressor performance due to tip clearance of centrifugal impellers," *Journal of Turbomachinery*, vol. 109, no. 1, pp. 55–61, 1987.
- [3] Y. Senoo, "Mechanics on the tip clearance loss of impeller blades," *Journal of Turbomachinery*, vol. 113, pp. 581–597, 1991.
- [4] M. Ishida, H. Ueki, and Y. Senoo, "Effect of blade tip configuration on tip clearance loss of a centrifugal blower," *Journal of Turbomachinery*, vol. 112, no. 1, pp. 14–18, 1990.
- [5] J. Tang, T. Turunen-Saaresti, and J. Larjola, "Use of partially shrouded impeller in a small centrifugal compressor," *Journal of Thermal Science*, vol. 17, no. 1, pp. 21–27, 2008.
- [6] A. Akturk and C. Camci, "Axial flow fan tip leakage flow control using tip platform extensions," *Journal of Fluids Engineering*, vol. 132, no. 5, Article ID 051109, 10 pages, 2010.
- [7] A. Akturk and C. Camci, "Tip clearance investigation of a ducted fan used in VTOL UAVs, part 1: baseline experiments and computational validation," in *Proceedings of the ASME Turbo Expo 2011*, 2011, Paper no. GT2011-46356.
- [8] A. Akturk and C. Camci, "Tip clearance investigation of a ducted fan used in VTOL UAVs, part 2: novel treatments via computational design and their experimental validation," in *Proceedings of the ASME Turbo Expo 2011*, 2011, Paper no. GT2011-46356.
- [9] F. Kameier and W. Neise, "Experimental study of tip clearance losses and noise in axial turbomachines and their reduction," *Journal of Turbomachinery*, vol. 119, no. 3, pp. 460–471, 1997.
- [10] N. Sitaram and R. Thakar, "Performance improvement of a low aspect ratio axial flow compressor by means of turbulence generator," *Journal of Aerospace Science and Technology*, vol. 59, no. 1, pp. 21–32, 2007.
- [11] N. Sitaram and B. Pandey, "Tip clearance effects on a centrifugal compressor," *Journal of The Aeronautical Society of India*, vol. 42, no. 4, pp. 309–315, 1990.
- [12] L. F. Schumann, D. A. Clark, and J. R. Wood, "Effect of area ratio on the performance of a 5.5:1 pressure ratio centrifugal impeller," *Journal of Turbomachinery*, vol. 109, no. 1, pp. 10–19, 1987.

## Research Article

# A Novel Approach to Evaluate the Benefits of Casing Treatment in Axial Compressors

Guillaume Legras,<sup>1</sup> Isabelle Trébinjac,<sup>1</sup> Nicolas Gourdain,<sup>2</sup>  
Xavier Ottavy,<sup>1</sup> and Lionel Castillon<sup>3</sup>

<sup>1</sup>LMFA, UMR 5509, Ecole Centrale de Lyon, UCB Lyon I and INSA, 69134 Ecully, France

<sup>2</sup>CERFACS, Computational Fluid Dynamics Team, 42 Avenue Gaspard Coriolis, 31057 Toulouse, France

<sup>3</sup>ONERA, Applied Aerodynamics Department, 8 Rue des Vertugadins, 92190 Meudon, France

Correspondence should be addressed to Guillaume Legras, guillaume.legras@gmail.com

Received 13 December 2011; Accepted 3 April 2012

Academic Editor: Cheng Xu

Copyright © 2012 Guillaume Legras et al. This is an open access article distributed under the Creative Commons Attribution License, which permits unrestricted use, distribution, and reproduction in any medium, provided the original work is properly cited.

Passive control devices based on casing treatments have already shown their capability to improve the flow stability in axial compressors. However, their optimization remains complex due to a partial understanding of the related physical mechanisms. In order to quantitatively assess the interaction between slots and the blade tip flow, the present paper develops a novel analysis methodology based on a control-volume approach located in the rotor tip region. This methodology may be used for analyzing the casing treatment based on both axi- and non-axisymmetric slots design. The second issue of the paper focuses on the application of the current approach to better understand the effects of axi- and non-axisymmetric grooves in three different axial compressors which differ by the flow regime (subsonic/transonic) and the smooth casing shape (cylindrical/concave). Numerical simulations are performed, and results of the current approach with and without casing treatments are compared.

## 1. Introduction

Today, it is mandatory for compressor designers to improve performance in terms of efficiency and operating range characterized by the stall margin at low mass flow rate. One of the main difficulties encountered in this process is that compressor stall is not always controlled through normal aerodynamic design. Thus stall prevention techniques must be used, and one promising technology known to bring substantial stability for tip critical compressor rotor is casing treatment (CT) [1]. This passive control device consists of slots within the rotor casing and presents various types of geometries: circumferential grooves [2–9], non-axisymmetric slot-type CT [10–14] and self-recirculating flow channels [15–17], and honeycomb [18]. Hathaway [19] provides an extensive overview of the research studies over the last 50 years that attempt to uncover the physics behind the improvement in stall margin.

However, this understanding is still not complete since experimental measurements in the near casing region are elaborate. Moreover, postprocessing numerical results using

2D or 3D views hardly allow a quantification and can cause in some cases a misunderstanding of the flow mechanisms. Therefore, CT design requires analysis methods that need to be as easy as possible to handle for aeroengine designers. In this context, Shabbir and Adamczyk [3] proposed an approach based on a budget analysis of the steady axial momentum equation close to the rotor casing. This methodology provides further insight into the flow mechanisms relevant to compressor stability systems. In fact, their paper shows the approach is innovative to quantitatively ascertain the influence of a design on the near casing flow and provides guidance on groove design along the axial direction. However, the Shabbir and Adamczyk methodology is restrained to the knowledge of changes in the balance of the steady axial momentum equation while CT interaction with the main flow is strongly complex (tridimensional and unsteady), thus requiring information coming from each of the Navier Stokes equations.

The current paper aims at further understanding and quantitatively diagnosing complex flow mechanisms such as those induced by CT. First, the paper described an extended

Shabbir and Adamczyk model (ESA model) that calculates the budget analysis of the Navier-Stokes set of (un)steady equations. Then, the model is used to investigate the flow mechanisms induced by CT in three different axial compressors. The idea is here to have a large test range in order to study the correlation between CT and the flow regime (subsonic and transonic), CT and the original smooth wall (SW) geometry (cylindrical or conical), and finally the main difference between axi- and non-axisymmetric CT. Results are based on numerical 3D calculations. In order to apprehend this novel approach, the control-volume analysis is hereafter limited to the axial momentum equation.

## 2. Flow Analysis Methodology

**2.1. Equations.** A control volume fixed in time and located in the near casing flow is retained. This will provide a quantitative understanding of the relevant fluid mechanisms associated with SW and CT configurations. Thus, the balance between the various terms which appear in the Navier-Stokes equations is analyzed based on its finite volume formulation. For simplicity reasons, the equations are considered in the relative rotor frame and in cylindrical coordinates. Using the divergence theorem, the Navier-Stokes equations in integral form can be written as follows:

$$V \int_{\partial t} \frac{\partial \mathbf{Q}}{\partial t} = - \oint_{\partial \Omega} [\mathbf{B}dA_r + \mathbf{C}dA_\theta + \mathbf{D}dA_z] + \mathbf{V}\mathbf{T}, \quad (1)$$

where  $A_r$ ,  $A_\theta$ , and  $A_z$  are the projection areas of the control volume,  $V$  the constant volume of the control domain,  $\mathbf{Q}$  the conservative variables,  $\mathbf{B}$ ,  $\mathbf{C}$ , and  $\mathbf{D}$  vectors resulting from the development of the advective and diffusive fluxes, and  $\mathbf{T}$  the forces per unit volume (usually named source terms). These vectors are recalled in (2). The stresses in (2) include both viscous and Reynolds stresses. In the same manner, the heat flux takes into account the heat flux and the enthalpy turbulent diffusion flux. This last term and the Reynolds stresses are both approximated by an eddy viscosity model:

$$\mathbf{Q} = \begin{bmatrix} \rho \\ \rho W_r \\ \rho W_\theta \\ \rho W_z \\ \rho E_r \end{bmatrix},$$

$$\mathbf{B} = \begin{bmatrix} \rho W_r \\ (\rho W_r^2 + P_s) - \tau_{rr} \\ \rho W_\theta W_r - \tau_{r\theta} \\ \rho W_z W_r - \tau_{rz} \\ (\rho E_r + P_s - \tau_{rr}) W_r - (W_\theta \tau_{r\theta} + W_z \tau_{rz} + q_r) \end{bmatrix},$$

$$\mathbf{C} = \begin{bmatrix} \rho W_\theta \\ \rho W_r W_\theta - \tau_{r\theta} \\ (\rho W_\theta^2 + P_s) - \tau_{\theta\theta} \\ \rho W_z W_\theta - \tau_{z\theta} \\ (\rho E_r + P_s - \tau_{\theta\theta}) W_\theta - (W_r \tau_{r\theta} + W_z \tau_{z\theta} + q_\theta) \end{bmatrix},$$

$$\mathbf{D} = \begin{bmatrix} \rho W_z \\ \rho W_r W_z - \tau_{rz} \\ \rho W_\theta W_z - \tau_{\theta z} \\ (\rho W_z^2 + P_s) - \tau_{zz} \\ (\rho E_r + P_s - \tau_{zz}) W_z - (W_r \tau_{rz} + W_\theta \tau_{z\theta} + q_z) \end{bmatrix},$$

$$\mathbf{T} = \begin{bmatrix} 0 \\ \frac{\rho W_\theta^2 - P_s - \tau_{\theta\theta}}{r} + 2\rho\omega W_\theta + \rho\omega^2 r \\ \frac{\rho W_\theta W_r - \tau_{r\theta}}{r} - 2\rho\omega W_r \\ 0 \\ \rho\omega^2 r W_\theta \end{bmatrix}. \quad (2)$$

**2.2. Numerical Resolution.** Since the objective is to understand the balance of the various terms using numerical CFD results, the semidiscretised in space for uncoupled time/space integration formulation of (1) is considered. This procedure corresponds to the finite volume method. For an individual basic hexahedral cell, this formulation is written as follows:

$$\frac{\partial \mathbf{Q}}{\partial t} = - \frac{1}{V} \left[ \sum_{l=1}^6 \mathbf{F} \cdot \mathbf{N}_{\Sigma_l} - \mathbf{V}\mathbf{T} \right] = - \frac{1}{V} \mathbf{R}(\mathbf{Q}), \quad (3)$$

where  $l$  designates the  $l$ th face bounding the cell,  $\mathbf{F}$  the numerical approximation of the exact flux (including the below tensors  $\mathbf{B}$ ,  $\mathbf{C}$ , and  $\mathbf{D}$ ),  $\mathbf{N}_{\Sigma_l}$  the external (nonunit) normal to the face  $\Sigma_l = [A_{rl}, A_{\theta l}, A_{zl}]^T$ , and  $\mathbf{R}$  the numerical modelling residual of variable  $\mathbf{Q}$ .

In order to access the information of all individual terms, a computation postprocessing tool has been developed. Since the volume does not depend on time, the source terms  $\mathbf{T}$  can be directly determined using (2). Concerning the time derivative terms, the choice is done to determine those terms at instant  $n$  by computing the opposite of the numerical modelling residual at the same instant:

$$V \frac{\partial \mathbf{Q}_n}{\partial t} = -\mathbf{R}(\mathbf{Q}_n). \quad (4)$$

Therefore, only the convective fluxes have to be computed (here with a 2nd-order centered Jameson scheme [21]).

Since most CFD codes solve the Navier-Stokes equations in the cartesian reference frame, a specific treatment was done to recover terms of (2) in cylindrical coordinates. To do so, the fluxes constitutive of terms in (2) are build up through projections of the cartesian fluxes into the cylindrical reference frame. This strategy, instead of applying a cylindrical spatial scheme, permits to ensure the same numerical modelling residual than that in the cartesian equations. Equation (5) presents the transformation matrix  $P$  for rotation by an angle of  $\theta$  over the longitudinal direction (i.e.,  $z$ ). Equation (6) recalls the expressions for projections from cartesian to cylindrical coordinates of the face areas  $\mathbf{A}$ , the relative

velocity vector  $\mathbf{W}$ , the stress tensor  $\boldsymbol{\tau}$ , and the heat flux vector  $\mathbf{q}$ :

$$P = \begin{bmatrix} \cos \theta & -\sin \theta & 0 \\ \sin \theta & \cos \theta & 0 \\ 0 & 0 & 1 \end{bmatrix} \quad (5)$$

$$\begin{aligned} \mathbf{A}_{r\theta z} &= P^{-T} \cdot \mathbf{A}_{xyz}, & \mathbf{W}_{r\theta z} &= P^{-T} \cdot \mathbf{W}_{xyz}, \\ \boldsymbol{\tau}_{r\theta z} &= P^{-T} \cdot \boldsymbol{\tau}_{xyz} \cdot P, & \mathbf{q}_{r\theta z} &= P^{-T} \cdot \mathbf{q}_{xyz}. \end{aligned} \quad (6)$$

For sake of clarity, the nomenclature used by Shabbir and Adamczyk [3] is chosen. The operator  $\Delta(\cdot) = \sum_{i=1}^6(\cdot)$  is introduced and characterizes the balance of flux on an individual basic cell. For example, the term  $\Delta(\rho W_z W_r A_r)$  appearing in the axial momentum equation corresponds to the transport of the axial momentum across the radial faces of a basic grid cell.

The objective is to understand the balance of the various terms by using data on a mesh grid. Thus, it is obvious that the control volume retained is based on this mesh. In consequence, the current approach is extended to a control volume composed of multiple grid cells. The operator  $\sum_r \sum_\theta \sum_z(\cdot) = \sum_{r,\theta,z}(\cdot)$  is introduced and realizes the cumulative sum on each individual grid cell. For example, the unsteady axial momentum equation can be written as follows:

$$\begin{aligned} & \sum_{r,\theta,z} \Delta(\rho W_z W_r A_r) + \sum_{r,\theta,z} \Delta(\rho W_z W_\theta A_\theta) + \sum_{r,\theta,z} \Delta(\rho W_z^2 A_z) \\ & + \sum_{r,\theta,z} \Delta(P_s A_z) + \sum_{r,\theta,z} (F_{\lambda_2}) + \sum_{r,\theta,z} (F_{\lambda_4}) - \sum_{r,\theta,z} \Delta(\tau_{rz} A_r) \\ & - \sum_{r,\theta,z} \Delta(\tau_{\theta z} A_\theta) - \sum_{r,\theta,z} \Delta(\tau_{zz} A_z) \\ & = R(\rho W_z) = V \frac{\partial \rho W_z}{\partial t}, \end{aligned} \quad (7)$$

where  $F_{\lambda_2}$  and  $F_{\lambda_4}$  correspond, respectively, to the 2nd and 4th numerical scalar artificial dissipation fluxes. These have been added to the equation due to the use of the 2nd-order centered Jameson scheme [21] in the numerical simulations. Therefore, the novel method allows the quantification of artificial dissipation fluxes on the balance of the axial momentum equation. Moreover, it is possible to localize regions and flow structures where these fluxes are active. Finally, notice that each term of (7) is homogeneous to a force per unit volume ( $[\text{kg} \cdot \text{m}^{-2} \cdot \text{s}^{-1}]$ ).

### 2.3. Application of the ESA Model

**2.3.1. On Steady Flows.** In the case of steady flow problems, time derivative terms are null leading to a balance of the advective and viscous fluxes and forces per volume unit. In practice, the precision of this equilibrium depends on the value of the numerical residual  $\mathbf{R}$ . For numerical data, it tends to reach zero at convergence according to the machines' precision. Equation (3) can be simplified as follows:

$$\mathbf{R}(\mathbf{Q}) \approx 0 \iff \sum_{i=1}^6 \mathbf{F} \cdot \mathbf{N}_{\Sigma_i} - V \mathbf{T}_\Omega \approx 0. \quad (8)$$

**2.3.2. On Unsteady Flows.** Concerning unsteady flow problems, time derivative terms need to be determined since they can strongly impact the equilibrium of the equations. Those are taken equal to  $-\mathbf{R}(\mathbf{Q})$ , which is consistent only if the result analyzed is a time-consistent solution (usually a periodic solution).

The current approach can be applied both on unsteady and time-averaged solution allowing access of specific information of the numerical modelling residual. In fact, assuming that any flow variable  $\mathbf{Q}$  can be decomposed into its mean term  $\overline{\mathbf{Q}}$  plus its deterministic component  $\mathbf{Q}'$  (stochastic component  $\mathbf{Q}''$  is neglected), that is,  $\mathbf{Q} = \overline{\mathbf{Q}} + \mathbf{Q}'$ , and by replacing each variable in (3), the residual operator can be written as

$$\overline{\mathbf{R}(\mathbf{Q})} = \mathbf{R}(\overline{\mathbf{Q}}) + \overline{\mathbf{R}(\mathbf{Q}')} = 0, \quad (9)$$

where  $\overline{\mathbf{R}(\mathbf{Q})}$  denotes the time-averaged balance of equation and tends to zero since the unsteady problem is periodic in time.  $\mathbf{R}(\overline{\mathbf{Q}})$  designates the residual applied to the time-averaged flow field.  $\overline{\mathbf{R}(\mathbf{Q}'')}$  indicates the time-averaged effect of the unsteadiness (also called lumped deterministic source terms by Ratzlaff et al. [23]).

## 3. Description of the Investigated Axial Compressors

In order to understand the CT effects on axial compressors features, three axial compressors are numerically investigated with and without CT: NASA Rotor 37 [24, 25], CREATE [26], and CBUA [22, 27]. They differ by the geometry of the smooth casing (cylindrical versus noncylindrical), the flow regime (subsonic versus transonic), and the CT geometry incorporated (circumferential grooves or slot-type CT). These differences are resumed in Table 1. The following paragraphs further describe the design features of these three compressors.

**3.1. NASA Rotor 37.** The well-known transonic experimental compressor NASA Rotor 37 (Figure 1) was designed and tested at the NASA Lewis Research Center [24, 25]. The main characteristics are recalled in Table 2. More details about the compressor design, extensive results, and comparisons of numerical and experimental data may be found in the following references: Suder and Celestina [28], Chima [29], Denton [30], and Dunham [20]. The NASA Rotor 37 has been chosen since it is known for the occurrence of the blade tip located rotating stall phenomena at operating close to surge [31]. Note that the original configuration experimentally tested does not include any CT (i.e., experimental data are only available for the SW configuration). The implementation of casing grooves is only investigated through numerical simulations.

The CT geometry is taken from Legras et al. [8] and consists of 6 circumferential slots (Figure 5(a)). Each groove is 3 mm wide (10.9% of rotor tip axial chord) with a gap of 1.5 mm between each cavity. The height-to-width ratio is 0.7 : 1. The first groove starts at around  $x/C = 5\%$  of the tip chord upstream of the rotor tip leading edge. Concerning the

TABLE 1: Differences between the axial compressors investigated.

		Investigated compressors		
		NASA Rotor 37	CREATE S1-R2	CBUAA
Geometry of the casing	Cylindrical	—	X	X
	Noncylindrical	X	—	—
Geometry of CT	Circumferential	X	X	—
	Slot type	—	—	X
Type of regime	Subsonic	—	X	—
	Transonic	X	—	X

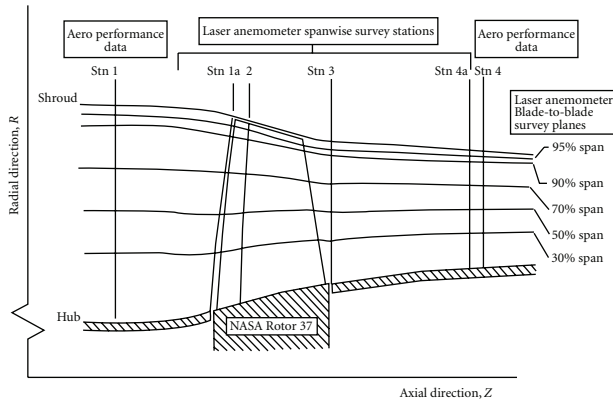


FIGURE 1: Cross-section of the NASA Rotor 37 [28].

TABLE 2: Design features of the NASA Rotor 37 [20].

Number of blades	36
Tip radius at leading edge	252 mm
Aspect ratio	1.19
Hub-tip radius ratio	0.70
Tip solidity	1.288
Tip clearance height	0.356 mm
Rotation speed	17188.7 rpm
Tip speed	457 m/s
Total pressure ratio	2.106
Adiabatic efficiency	0.877
Design mass flow	20.188 kg·s <sup>-1</sup>
Choked mass flow	20.93 ± 0.14 kg·s <sup>-1</sup>

design, the objective was not to optimize the CT geometry but to reach a comprehensive description of the change in flow properties generated by the grooves. Therefore, it was found interesting to investigate the impact of a slot that surmounts the blade tip leading edge, even if its usefulness is not obvious.

**3.2. Multistage Compressor CREATE.** CREATE (Compresseur de Recherche pour l'Etude des Effets Aérodynamiques et Technologiques, Figure 2) is a research 3.5-stage axial compressor designed by SNECMA and tested at the Ecole Centrale de Lyon in LMFA research laboratory. This subsonic compressor is dedicated to aerothermal and aerodynamic

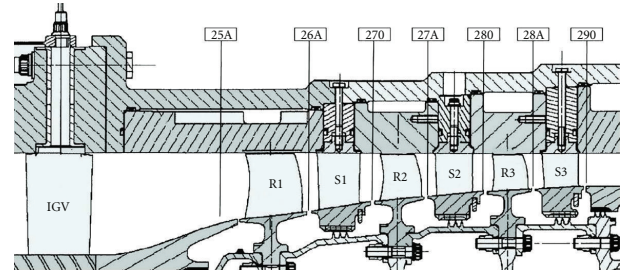


FIGURE 2: Cross-section of the CREATE high-pressure compressor and measurement planes.

TABLE 3: Design features of CREATE.

Cylindrical outer casing diameter	0.52 m
Rotation speed	11543 rpm
Tip rotor speed	313 m·s <sup>-1</sup>

TABLE 4: Number of blades of CREATE rows.

Row	IGV	R1	S1	R2	S2	R3	S3
Number of blades per row (for $2\pi$ )	32	64	96	80	112	80	128
Number of blades for $2\pi/16$	2	4	6	5	7	5	8

studies. Its geometry and rotation speed are representative of high-pressure compressor median-rear blocks of modern turbojet engine. Its design features are recalled in Tables 3 and 4. More details about the compressor design can be found in Touyeras and Villain [26]. Thanks to the large amount of measurements, this experimental compressor has been the subject of different research works focused on rotor/stator interactions [32, 33] and CFD methods calibration and improvement [34–36].

It was numerically seen at nominal speed that the stability of the untreated casing compressor is limited by the tip clearance effects on stages 2 and 3 [36]. As a result, it was chosen to implement on both stages a CT in the form of five axisymmetric grooves of equal width and equally distributed in the axial direction. Details of the design study can be found in Perrot et al. [4]. Note that, for confidentiality reasons, slots dimensions are not mentioned, and the following results are normalized. However, for the purpose of the current study, the CT flow analysis is only focused on the grooves implemented in the R2 rotor row. Furthermore, notice that the numerical results are based on Legras et al. [37].

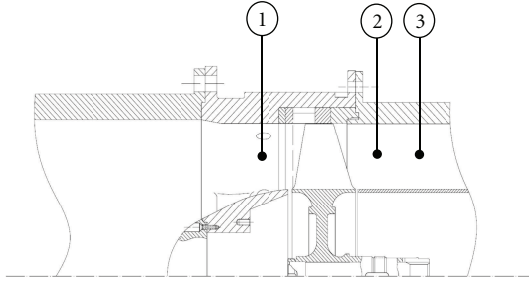


FIGURE 3: Cross-section view of the test section [22].

TABLE 5: Design features of the CBUAA [22].

Blade number	17
Tip diameter	355.8 mm
Design speed	22000 rpm
Hub-to-tip ratio	0.565
Aspect ratio	0.956
Mass flow at design point	13.4 kg·s <sup>-1</sup>
Total pressure ratio at design speed	1.6 (stage)
Adiabatic efficiency at design speed	0.88 (stage)
Relative Mach number of tip rotor speed	1.404

Performances are obtained on the overall configuration R1-S3, whereas the CTs implemented in R2 are investigated using modelisation of the S1-R2 configuration.

**3.3. CBUAA Compressor Test Case.** The Compressor of the Beijing University of Aeronautics & Astronautics (CBUAA) is a single-stage transonic axial compressor (Figure 3). A brief description of the test rotor can be seen in Table 5. In the experiment, the stator is placed far downstream of test rotor; thus the isolated rotor environment can be established. Experimental and numerical studies of the test case can be found in Lin et al. [22] and Ning and Xu [27].

The slot-type CT is illustrated in Figure 4 [22, 27]. The total slot number is 153 (9 times the blade number). The slots are skewed to have a 45 degrees angle so that their openings face the pressure side of the blades. The axial length of the slots is 79% of the blade tip axial chord (with 39% exposed to the blade tip). The ratio of the open area of the slots to the casing annulus area is 0.8. The radial depth of the slots is 9 mm. Moreover, the CT has a recess chamber and its radial depth is 9 mm.

## 4. Compressors Modelisation

**4.1. Description of the Numerical Methods.** All numerical simulations are carried out using the *elsA* software developed by ONERA and CERFACS [38]. The code solves the Favre-Reynolds-averaged Navier-Stokes equations on multi-block structured meshes using a cell-centered finite-volume approach. It also allows the use of the Chimera method dedicated to modelize complex geometries typically generated by technological effects [39]. Thus, the Chimera method is here used to model the CT.

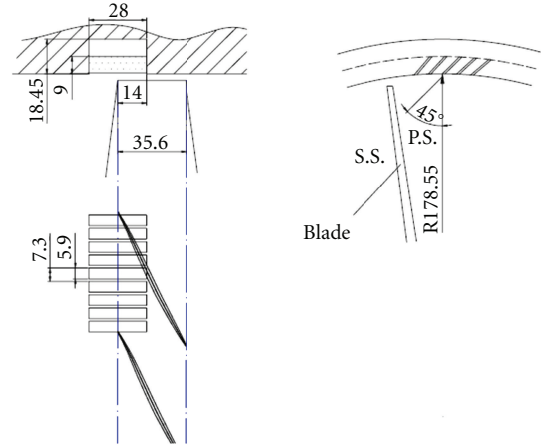


FIGURE 4: Sketch of the CBUAA slot-type casing treatment [22].

Computations were run with a 2nd-order centered Jameson scheme [21] for the estimation of convective fluxes. The time marching is performed by an efficient implicit time integration scheme based on the backward Euler scheme and a scalar lower-upper (lu) symmetric successive overrelaxation (SSOR) method. Concerning the numerical approach, it differs depending on the investigated compressor case (see Table 6).

For the NASA Rotor 37 configuration, circumferential grooves are axisymmetric. They can be considered as a continuing circumferential modification of the casing and then be computed similarly to SW configuration in a conventional steady-state approach.

Concerning the CREATE S1-R2 configuration, the use of an unsteady approach with phase-lagged boundary conditions at the rows' interfaces and on the periodic boundaries enables to consider only one single-blade passage for each row [40, 41].

For CBUAA case with slot-type CT, simulations used an unsteady overset grids' method coupled with a phase-lagged condition at the interface between rotor and CT slot Chimera blocks [42]. This procedure reduces the computational domain to one single-blade passage and one CT slot.

The turbulence is modeled by the two-equation model  $k - \omega$  proposed by Wilcox [43] for both the NASA Rotor 37 and the CBUAA, and the two-equation model of  $k - \epsilon$  low-Reynolds of Launder-Sharma for the CREATE case. The flow is assumed to be fully turbulent since the mean Reynolds number based on the blade chord is approximately  $5 \cdot 10^6$ .

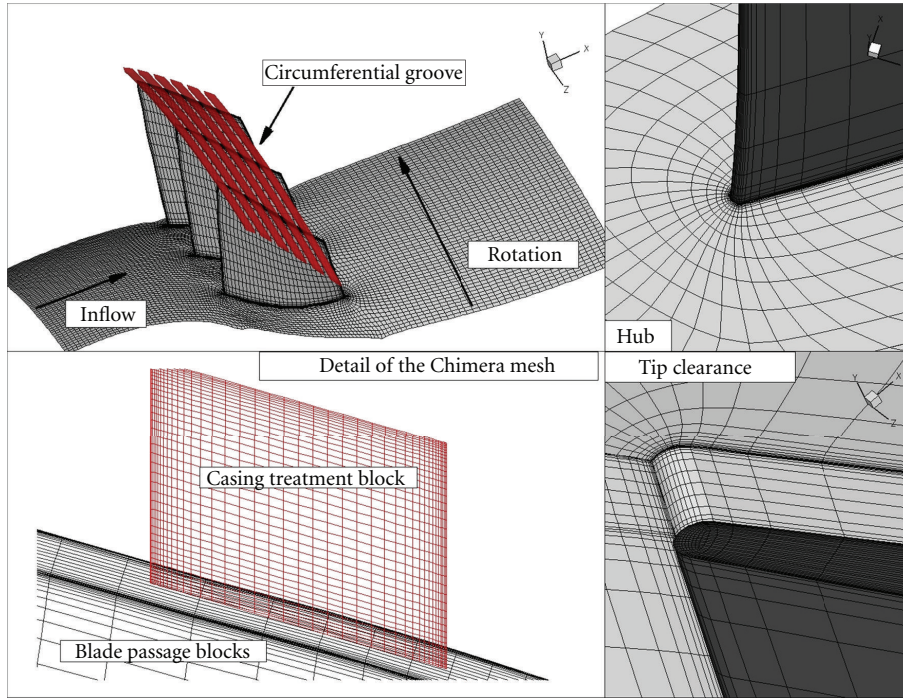
Numerical validation and other modelling details are given, respectively, for

- (i) the NASA Rotor 37 in Legras et al. [8, 9],
- (ii) the CREATE case in Legras et al. [37],
- (iii) the CBUAA in Legras et al. [44], Castillon and Legras [42].

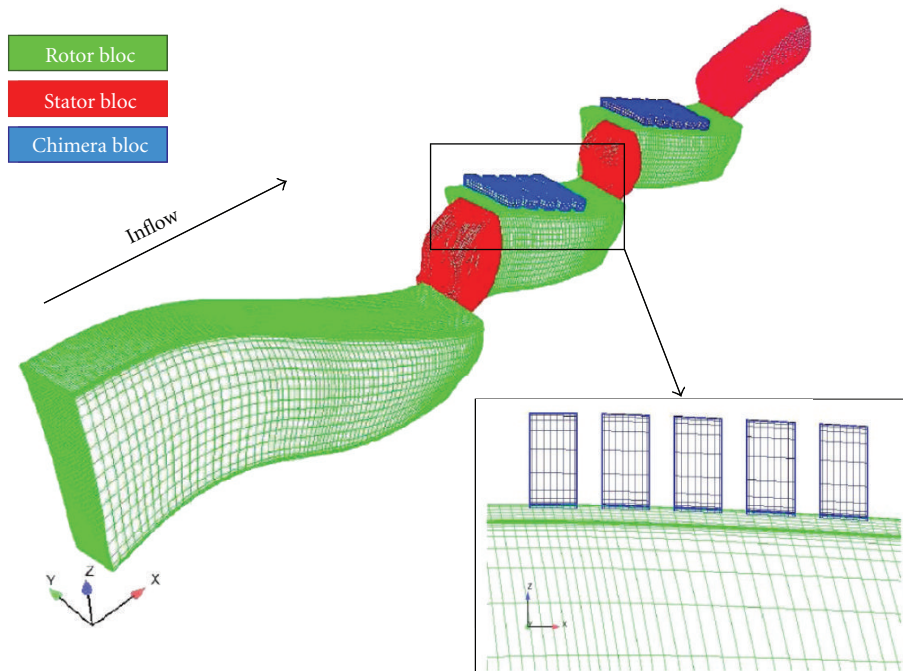
**4.2. Meshing Strategies.** For all compressors, the flow domain is discretized with a low-Reynolds multiblock structured

TABLE 6: Numerical approaches performed according to the compressor investigated.

Numerical approaches	Investigated compressors		
	NASA Rotor 37 axi. CT	CREATE S1-R2 axi. CT	CBUAA non axi. CT
Steady	X	—	—
Unsteady (phase-lagged)	—	X	X



(a) NASA Rotor 37



(b) CREATE

FIGURE 5: Chimera meshes used for modelling circumferential CT.

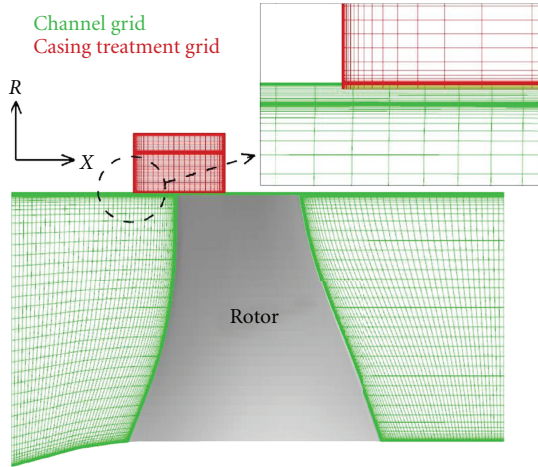


FIGURE 6: Chimera mesh used for modelling the slot-type CT of the CBUAA case.

approach. Each SW configuration counts approximately a total of 1.2–1.5 million grid points. The meshes are clustered towards the solid boundaries in order to reach the resolution requirement of  $y^+ \approx 1$  (the size of the first layer is approximately  $1 \mu\text{m}$ ). They are characterized by 89 grid points in the spanwise direction. The tip leakage region is discretized using a “O-H” grid topology with 25 points in the radial direction.

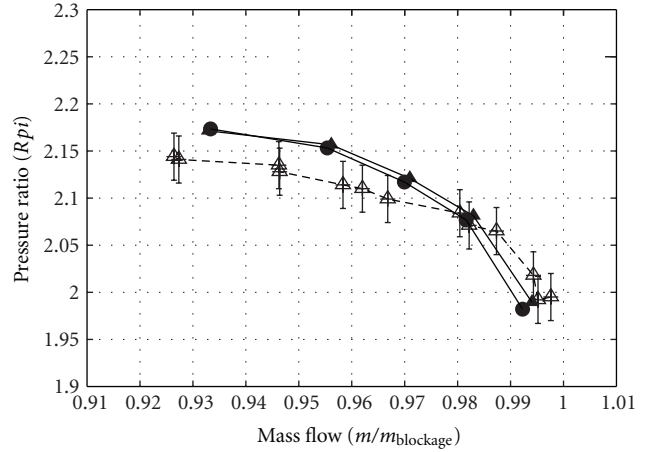
Concerning the CT configurations, they are based on the SW meshes at which “H” Chimera blocks modelling the casing grooves have been added (Figures 5 and 6).

### 5. Overall Performances

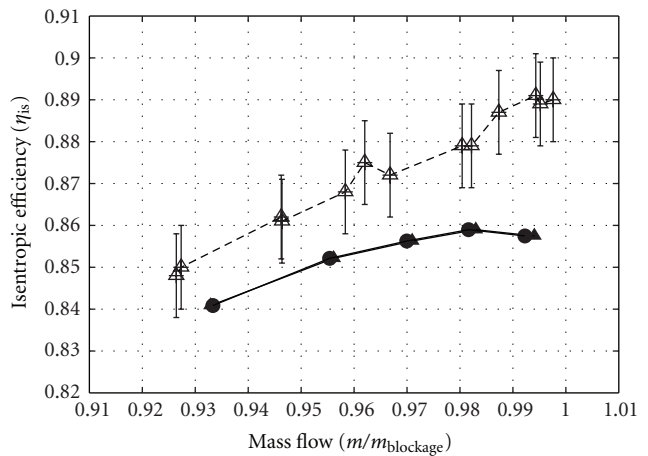
Figures 7, 8, and 9 present the measured and calculated performances at design speed, respectively, for the NASA Rotor 37, CREATE R1-S3 configuration, and CBUAA.

**5.1. Results of the NASA Rotor 37.** In Figure 7, the mass flow rates are normalized by the experimental choked mass flow ( $20.93 \text{ kg}\cdot\text{s}^{-1}$ ). The pressure ratio-mass flow curves show a fairly good agreement between numerical and experimental results for the SW configuration. However, the efficiency curve resulting from the simulation is clearly shifted which leads to underestimate the efficiency whatever the mass flow.

The numerical results of the CT configuration show only slight differences with the SW case in terms of performance (Figure 7). As observed by Legras et al. [8, 9], those small differences are all the more surprising that important radial flow exchanges occur between the 2nd and the 4th slots and the main flow. It is interesting to note that nearly all numerical studies that investigate CT for the NASA Rotor 37 present a relative insensitivity of the slots on the performance (circumferential grooves [45–47]; semicircular slots [31]). The application of the current methodology applied on the near casing flow region can be useful to ascertain the flow mechanisms, to quantify the fluxes and finally to understand



(a) Pressure rise



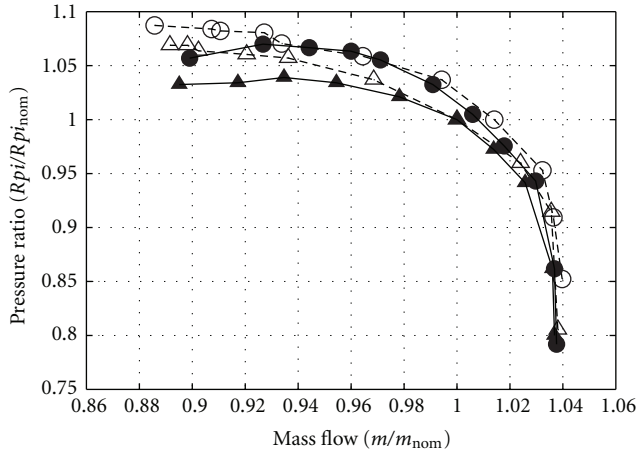
(b) Isentropic efficiency

FIGURE 7: Predicted NASA Rotor 37 characteristics at design speed.

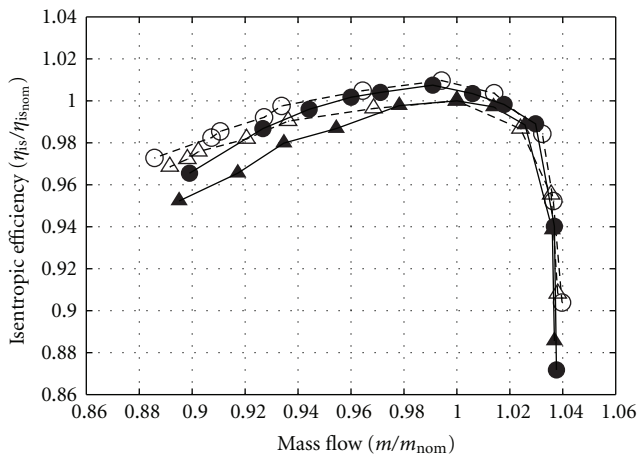
why the implementation of CT is nonefficient in the NASA Rotor 37.

**5.2. Results of the CREATE R1-S3 Configuration.** Overall performances presented in Figure 8 are normalized by the SW values at nominal operating conditions. Experimental uncertainties are 0.46%, 0.17%, and 0.32%, respectively, for the mass flow rate, the pressure ratio, and the isentropic efficiency. Concerning the steady numerical results, the limit of stability is estimated considering the last converged calculation.

Results in Figure 8 show that the shapes of the pressure rise and isentropic efficiency curves are correctly represented by the simulations. The main information of Figure 8 is that the numerical simulation is able to predict the trend observed in the measurement that CT improves performances compared to the SW case. The relative shifts in performance between both cases at design operating condition speed are



(a) Pressure rise



(b) Isentropic efficiency

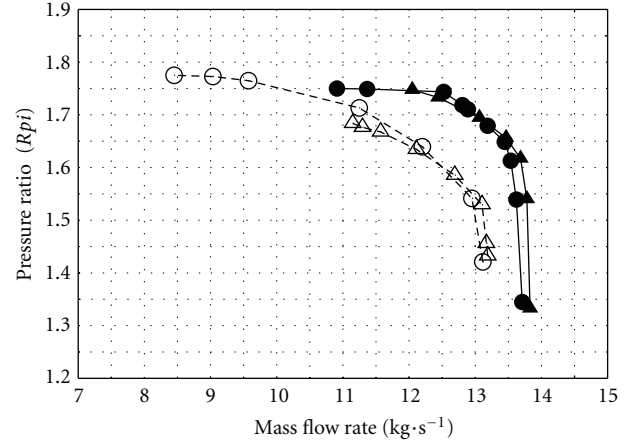
- △- Experimental: smooth wall
- Experimental: casing treatment
- ▲- Simulation: smooth wall
- Simulation: casing treatment

FIGURE 8: CREATE characteristics relative to nominal operating point (experimental versus numerical simulations).

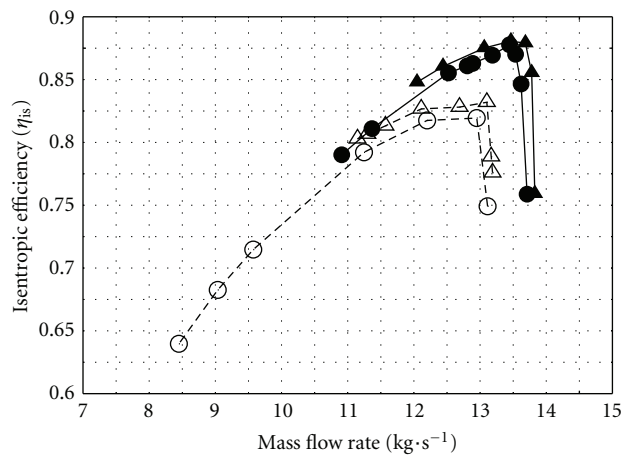
approximately  $\Delta\eta_{is,max} = +1\%$ ,  $\Delta Rpi_{max} = +2\%$ . For the steady simulations of the whole compressor being validated, let us analyze the unsteady calculations of the S1-R2 configuration.

Moreover, Legras et al. [37] present local flow comparisons between CFD results and LDA measurements done in the rotor tip clearance and inside the CT of CREATE compressor. They proved that the CFD model correctly predicts the main characteristics of the flow in this region and particularly the rotor tip vortex, the flow inside the CT, and the flow interactions between the CT and the throughflow (i.e., radial flow exchanges).

**5.3. Results of the CBUAA.** Rotor characteristics of both SW and CT configurations obtained at 98% speed by the experiment [22] and predicted by unsteady simulations are



(a) Pressure rise



(b) Isentropic efficiency

- △- Experimental: smooth wall
- Experimental: casing treatment
- ▲- Simulation: smooth wall
- Simulation: casing treatment

FIGURE 9: CBUAA characteristics at design speed (experimental versus numerical simulations).

compared in Figure 9. The numerical curves shapes are in fairly good agreement with the measurements. However, numerical characteristics are shifted due to a larger mass flow rate at choked conditions than the measured value (as predicted by Lin et al. [22] and Ning and Xu [27]). Simulations overestimate total pressure as well as efficiency magnitudes. The stable operating range of the SW configuration is correctly predicted. Concerning CT case, simulations clearly underestimate the operating range due to the onset of stall point at higher mass flow rate than the experiment. Finally, the calculated efficiency curves of the CT configuration show lower magnitude than the SW case one in the SW operating range, whereas the magnitude of the total pressure CT curve is similar. These differences have also been observed by other authors who numerically investigated the present test case [22, 27].

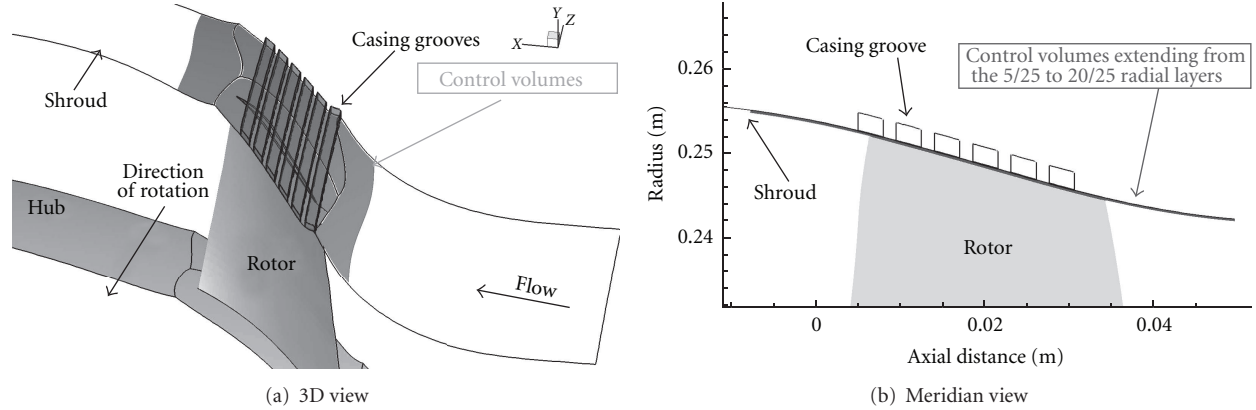


FIGURE 10: Views of the control volume located the NASA Rotor 37 tip clearance.

**5.4. Discussion of the Effect of CT Design on Overall Performances.** The comparison of the three compressors performances indicates that the implementation of axisymmetric CT induces a low stall margin improvement and no penalty in compressor efficiency. On the contrary, non-axisymmetric CT greatly improves the stall margin but reduces the compressor efficiency. This observation suggests that the more the CT is efficient to enhance stall margin, the more the compressor is subject to a decrease of its efficiency. This observation is in agreement with results observed in the literature by Hathaway [19].

Finally, based on the comparisons between experimental and numerical results, it was considered that the numerical models are able to reveal the overall flow mechanisms occurring near the outer casing. This is essential for the objective of the present work aiming at understanding the local influence of CT slots.

## 6. CT Flow Mechanisms Analysis according to the ESA Model

This section is dedicated to the analysis of the flow interaction between rotor and CT at the last SW stable operating point. To do so, the ESA model is used to get further insight into the understanding of the phenomenon. In practical terms, a control volume analysis is here performed on the blade tip flow and comparisons between SW and CT configurations are done.

**6.1. Equation Analyzed.** As it has been observed in previous studies, the CT interaction with the blade tip flow is mainly tridimensional and unsteady. In order to handle the results interpretation, the scope of the CT flow mechanisms' study is restrained to the analysis of the balance of the axial momentum (7). Thus, results in terms of axial forces acting on the blade tip flow are expected. This equation is chosen since it describes the global flow across the rotor channel, specially its pressure rise.

Here, we notice that the CFD computations presented before has been performed with steady as well as unsteady approaches. Thus, for the NASA Rotor 37, steady

axial momentum balance have been computed. On the contrary, for the CREATE and CBUAA cases, instantaneous axial momentum balances have been obtained for instants equally spread over a respective known temporal period:

- (i) for CREATE, 25 instants equally spread over one upstream stator blade S1 passing temporal period ( $T_{S1}$ );
- (ii) for CBUAA, 17 instants spread over one CT slot passing temporal period ( $T_{CT}$ ).

For these two last compressors, the contribution of the time derivative term  $\partial \rho W_z / \partial t$  can be computed, which cannot be done for NASA Rotor 37. In order to permit comparisons between the three compressors, CREATE and CBUAA instantaneous axial momentum balances are time-averaged on their respective temporal periods. In other words, NASA steady axial momentum balance is here compared to CREATE and CBUAA time-averaged axial momentum balances.

**6.2. Definition of the Control Volume.** For all configurations, the control volume surrounds the rotor blade tip flow field as shown in Figure 10. It is circumferentially delimited by the rotor blade pitch, axially extended just upstream and downstream of the rotor blade tip, and radially bounded by the 5th/25 to the 20th/25 grid layers modelling the rotor tip clearance. Therefore, due to the Chimera technique in the grooved configurations, the control volume is not attached to the shroud. In fact, the two last radial layers normal to the casing are used for interpolation between grooves and the blade passage blocks. These are not taken into account in the control volume since they can mislead the Navier-Stokes equations equilibrium.

**6.3. Global Flow Mechanisms Acting on the Near Casing Flow.** Results of the axial momentum balance for the SW and CT configurations are presented, respectively, for NASA Rotor 37 in Figure 11, CREATE in Figure 12, and CBUAA in Figure 13. This kind of representation, as histograms, provides a macroscopic view of the different axial forces acting on the control volumes (i.e., the near casing flow). As a consequence, one

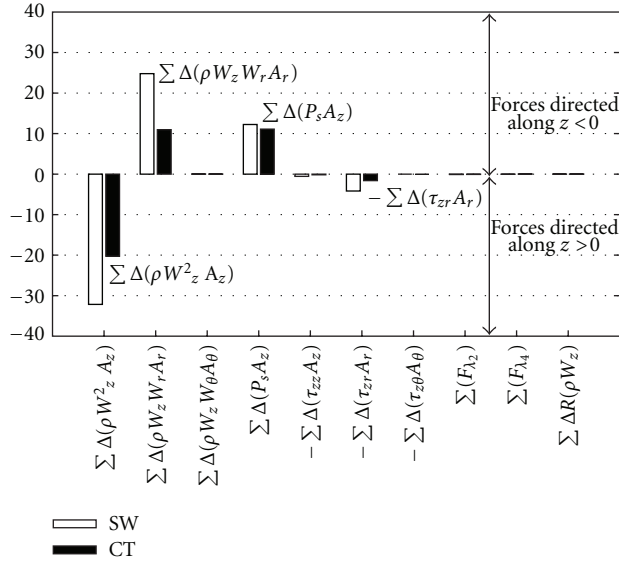


FIGURE 11: NASA Rotor 37 with and without CT: balance of the axial momentum equation.

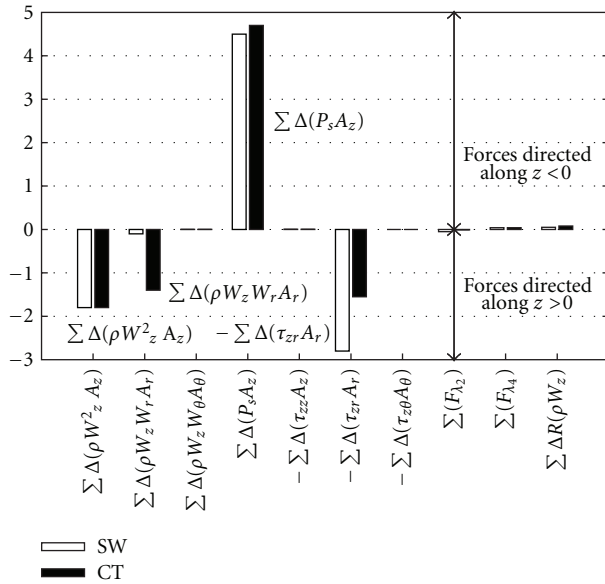


FIGURE 12: CREATE-R2 with and without CT: balance of the axial momentum equation.

has to take care of the results interpretation since histograms do not describe the local influence of CT. This will be further done in the next section titled “Longitudinal evolutions of the axial forces and CT contribution”.

Before discussing the physical analysis, it is instructive to comment on the magnitude of the numerical terms of the balance. Results show that the numerical modelling residuals  $R(\rho W_z)$  tend to zero leading to a good precision of the balance of the equation. For the CREATE and CBUAA cases, it signifies that the time-averaged temporal derivative term (i.e.,  $= -\bar{R}(\rho W_z)$ ) obtained from unsteady simulations

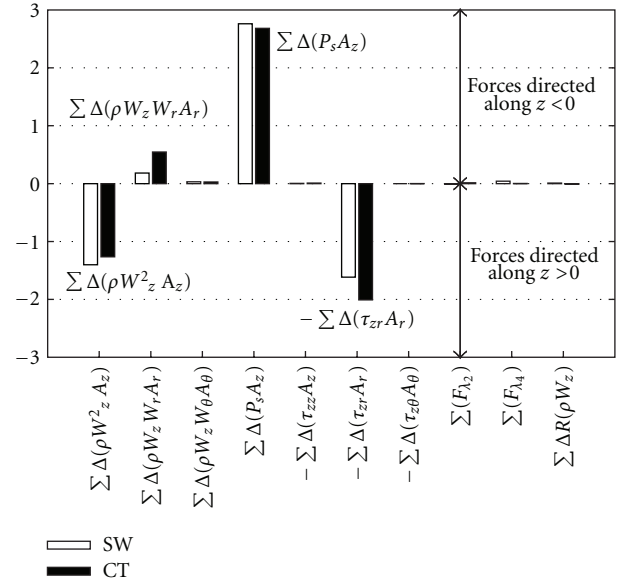


FIGURE 13: CBUAA with and without CT: balance of the axial momentum equation.

converges to zero. This observation lends support that the unsteady calculations correctly reach a time-periodic state. Moreover, it can be observed that scalar artificial viscosity fluxes ( $F_{\lambda_2}$  and  $F_{\lambda_4}$ ) are insignificant in spite of the presence of a strong shock wave located in the blade tip region of the NASA Rotor 37 and the CBUAA.

### 6.3.1. SW Results

*General Overview.* For all SW configurations, results highlight the presence of four main axial forces being applied on the control volume:

- (i) the axial pressure force  $\sum \Delta(P_s A_z)$  that corresponds to the axial flow pressure rise across the rotor.
- (ii) The axial force due to the transport of the axial momentum across the longitudinal faces  $\sum \Delta(\rho W_z^2 A_z)$ . This term is similar to a dynamic pressure force that acts on the same surfaces than the pressure force. Its value relates to the flow axial acceleration or deceleration. In fact, by simply differentiating the terms between the axial outlet and inlet of the control volume (i.e.,  $[(\rho W_z^2 A_z)_{\text{outlet}} - (\rho W_z^2 A_z)_{\text{inlet}}]$ ) and assuming that  $W_z$  is mainly positive in the volume (which is not locally true due to the presence of the tip leakage, casing boundary layer, ...), a negative (resp. positive) force corresponds to a deceleration (resp. acceleration) of the flow. The same reasoning can be done with  $W_z < 0$  that leads to the inverse conclusion. Results in Figures 11, 12, and 13 indicate that the incoming flow decelerates along the axial direction. This observation is coherent with the general aerodynamic of compressor since the casing boundary layer and the tip leakage flow

greatly influence the incoming flow. Furthermore, the term  $\sum \Delta(\rho W_z^2 A_z)$  gives information on the axial flow blockage occurring in the control volume.

- (iii) The axial shear force acting on the radial faces of the control volumes  $-\sum \Delta(\tau_{rz} A_r)$  induced by casing and blade tip boundary layers as well as the tip leakage flow.
- (iv) The axial force due to the transport of the axial momentum across the radial faces  $\sum \Delta(\rho W_z W_r A_r)$ . This term expresses the influence of the radial flow on the balance of axial forces. This force acts on the same faces than the axial shear force  $-\sum \Delta(\tau_{rz} A_r)$ . Thus, it is believed that a change of one of these forces can strongly influence the other.

All other terms are zero due to periodicity (forces acting on  $A_\theta$  faces) or to the radial thickness of the control volume. It is worth noticing that the forces applied on the near casing flow correspond to those observed in similar works done by Shabbir and Adamczyk [3].

These axial forces can be distinguished depending on whether they are acting in the same direction of the flow ( $z > 0$ ) or in opposite direction of the flow ( $z < 0$ ). This information is given by the sign of the terms. A sketch describing the nomenclature of the axial forces acting on the control volume is presented in Figure 22. The results show for all compressors some coherent trends:

- (i) the axial force due to  $\sum \Delta(P_s A_z)$  always acts in the opposite direction of the flow advance since the term is positive;
- (ii) the axial forces due to  $\sum \Delta(\rho W_z^2 A_z)$  and  $-\sum \Delta(\tau_{rz} A_r)$  always act in the same direction as the flow advance since the terms are negative.

This observation is consistent with the general aerodynamic of axial compressor. The casing boundary layer (represented by  $-\sum \Delta(\tau_{rz} A_r)$ ) and the upstream flow advance (described by  $\sum \Delta(\rho W_z^2 A_z)$ ) balance the adverse pressure gradient ( $\sum \Delta(P_s A_z)$ ) created by the axial compressor. If the boundary layer separates from the casing and/or if the flow advance is too low (like when the mass flow rate is too low), the pressure rise cannot be held, thus leading to an unstable operating flow condition.

The different compressors differ by the magnitude of these axial forces and the direction of the  $\sum \Delta(\rho W_z W_r A_r)$ .

*Influence of the Casing Geometry.* Figures 11, 12, and 13 clearly highlight the impact of the annulus shape (cylindrical versus conical). In fact, both CREATE and CBUAA compressors, which have a cylindrical casing, show similar results characterized by

- (i) same relative balance between  $\sum \Delta(P_s A_z)$  and the opposite axial forces  $\sum \Delta(\rho W_z^2 A_z)$  and  $-\sum \Delta(\tau_{rz} A_r)$ ,
- (ii) insignificant influence of  $\sum \Delta(\rho W_z W_r A_r)$ .

On the contrary, the NASA Rotor 37 that has a noncylindrical casing shows the occurrence of another axial force that is

due to  $\sum \Delta(\rho W_z W_r A_r)$ . This force comes to contribute with the adverse pressure force  $\sum \Delta(P_s A_z)$  to counteract the flow advance (i.e.,  $z < 0$ ). This result is clearly obvious since the conical casing forces the flow to have a radial velocity component  $W_r < 0$ . The near casing flow deflection is large enough to affect the balance of axial momentum, and it manifests itself through the axial force  $\sum \Delta(\rho W_z W_r A_r)$ .

*Influence of the Flow Regime.* The comparison between CREATE and CBUAA (Figures 12 and 13), which, respectively, works in subsonic and transonic flow regime, indicates no major difference in the axial momentum balance. Furthermore, the comparison between NASA Rotor 37 and CBUAA (Figures 11 and 13) proves that the shape of the rotor casing has a greater influence than the flow regime.

### 6.3.2. CT Results

*General Overview.* The results of the CT configurations in Figures 11, 12, and 13 show the same type of forces acting on the blade tip flow than SW cases. However, the influence of CT is here revealed by changes of the axial forces contribution.

For all compressors, the magnitude of pressure rise across the rotor  $\sum \Delta(P_s A_z)$  follows the predicted overall performances (see Figures 7, 8, and 9).

Due to the radial flow exchanges between the grooves and the throughflow (see [9, 37, 44] for images of the flow exchanges), CT is expected to contribute to balance the axial momentum equation with additional terms. As previously assumed in the SW analysis, the radial flow exchanges might influence the axial momentum equation through the force  $\sum \Delta(\rho W_z W_r A_r)$ . In fact, results are in agreement with this hypothesis. They clearly show that the main impact of the CT, whether it is axisymmetric or not, is revealed by the changes of  $\sum \Delta(\rho W_z W_r A_r)$  and the viscous force  $-\sum \Delta(\tau_{rz} A_r)$  due to the casing boundary layer. As previously announced, these two forces might influence each other since they both act on the same faces of the control volume. In fact, results reveal that the axial force  $\sum \Delta(\rho W_z W_r A_r)$  changes proportionally to  $-\sum \Delta(\tau_{rz} A_r)$ . These observations can be interpreted as follows: the radial fluid exchanges between the CT slots and the rotor channel tend to replace the casing boundary layer in its role to balance the adverse pressure gradient. This suggests that the  $W_r$  magnitude is a key point to the CT flow mechanisms. If the reasoning is pushed further, one explanation of the CT efficiency to improve the stall margin might come from its capability to perform an axial force due to the radial flow exchanges (through the axial force  $\sum \Delta(\rho W_z W_r A_r)$ ) more robust to the adverse pressure gradient than the casing boundary layer (through the axial force  $-\sum \Delta(\tau_{rz} A_r)$ ). Moreover, since the shear axial force can induce a loss of efficiency, the use of radial flow exchanges as an alternative to casing boundary layer effect is very interesting in order to increase the global efficiency of the compressor rotor. As a consequence, the main difference between axisymmetric and non-axisymmetric CT can be evaluated depending on the  $W_r$  evolution.

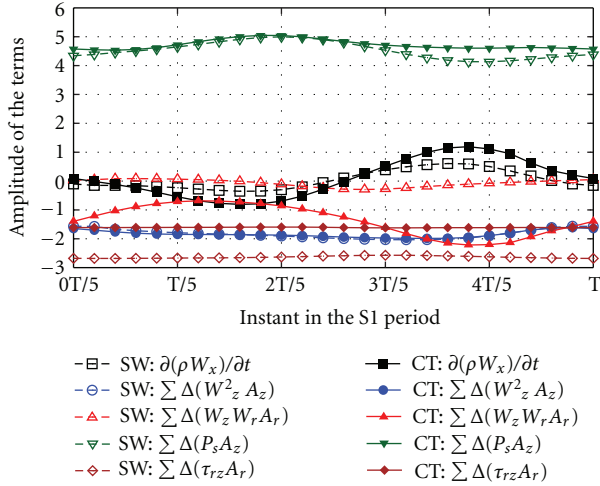


FIGURE 14: CREATE-R2 with and without CT: temporal evolution of the main terms of the unsteady axial momentum equation.

The results of the NASA Rotor 37 (Figure 11) and CREATE (Figure 12) indicate that circumferential CT contribute with additional axial force  $\sum \Delta(\rho W_z W_r A_r) < 0$  acting on the flow advance. As expected, it is the effect of the radial flow exchanges and this observation is in agreement with results of Shabbir and Adamczyk [3]. This adding term  $\sum \Delta(\rho W_z W_r A_r) < 0$  is accompanied with a proportional decrease of the viscous axial force  $-\sum \Delta(\tau_{rz} A_r)$ . It can be relied to the slight gain in efficiency observed in CREATE performances (Figure 8). As a matter of fact, the main role of axisymmetric CT is to turn or drive the force  $\sum \Delta(\rho W_z W_r A_r)$  more along the main flow direction, that is,  $z > 0$ . This is consistent with the general conclusions that previous studies have found that the reverse tip leakage flow through the tip gap got pushed into the grooves by the re-injecting flow (in main flow direction) from the grooves.

On the contrary, the CBUAA slot-type CT contributes by additional force  $\sum \Delta(\rho W_z W_r A_r) > 0$  acting in opposite direction to the flow as well as  $\sum \Delta(P_s A_z)$  (Figure 13). Moreover, the viscous axial force  $-\sum \Delta(\tau_{rz} A_r)$  has increased proportionally, thus explaining the slight decrease in efficiency observed in CBUAA performances (Figure 9). This first result reveals that slot-type CT behaves in a different manner than circumferential CT. However, as mentioned below histograms present a global and not a local influence of the CT. For this particular CT geometry, a local analysis has to be done to further understand the flow mechanisms as it will be seen in the next paragraphs.

For both axi- and non-axisymmetric grooves, the balance change is made possible through the modification of the radial velocity  $W_r$  induced by flow exchanges between grooves and the throughflow. It further supports that  $W_r$  is quite important for the flow stabilization in the tip region. This observation has to be confirmed by the local analysis of the CT flow mechanisms.

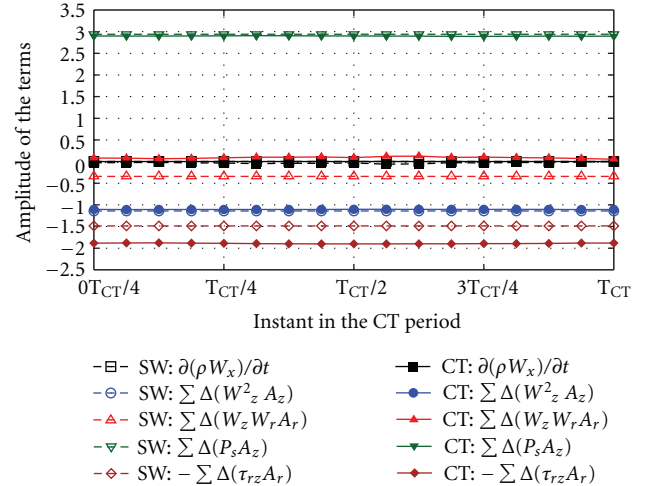


FIGURE 15: CBUAA with and without CT: temporal evolution of the main terms of the unsteady axial momentum equation.

**6.3.3. Unsteady Flow Mechanisms.** Figures 14 and 15 present, respectively, for CREATE and CBUAA the temporal evolution of the unsteady axial momentum balance. This analysis allows us to gain a quantitative and qualitative knowledge of the contribution of the time derivative term  $\partial \rho W_z / \partial t$ .

**Results of the CREATE-R2.** For the CREATE case, unsteady results are presented over the upstream stator S1 passing temporal period. Plots in Figure 14 show a sinusoidal time-dependent evolution of the time-derivative term influenced by the stator S1 blade passage frequency  $T_{S1}$ . Its time-averaged value tends to zero, in agreement with results shown in Figure 12. Concerning its temporal fluctuations, amplitudes are particularly pronounced for the CT case with higher values of a factor 2 compared to the SW. Moreover, results show that  $\partial \rho W_z / \partial t$  amplitudes are mainly driven by those of  $\sum \Delta(P_s A_z)$  in the SW case and those of  $\sum \Delta(\rho W_z W_r A_r)$  in the CT case. In fact, CT deadens the magnitude of the  $\sum \Delta(P_s A_z)$  fluctuations by a factor 2 which is believed to greatly enhance the flow stability (because the pressure gradient opposes the flow). The increase in  $\sum \Delta(\rho W_z W_r A_r)$  fluctuation, which drives the time-dependent term, proves that groove mechanisms strongly respond to upstream flow unsteadiness.

**Results of the CBUAA.** Concerning the CBUAA case, unsteady results are presented over the CT slot passing temporal period  $T_{CT}$ . Plots in Figure 15 indicate that all terms present a “quasi-steady” behaviour, supporting that unsteadiness of the CT interaction with the throughflow is insignificant. This observation is especially confirmed by the zero magnitude over  $T_{CT}$  of the time-derivative term  $\partial \rho W_z / \partial t$ . This “quasi-steady” behaviour has already been observed by Lin et al. [22], and Ning and Xu [27]. Indeed, the unsteady time scale of the discrete treatment slots is therefore considerably small compared to that of the blade passage [27]; thus the

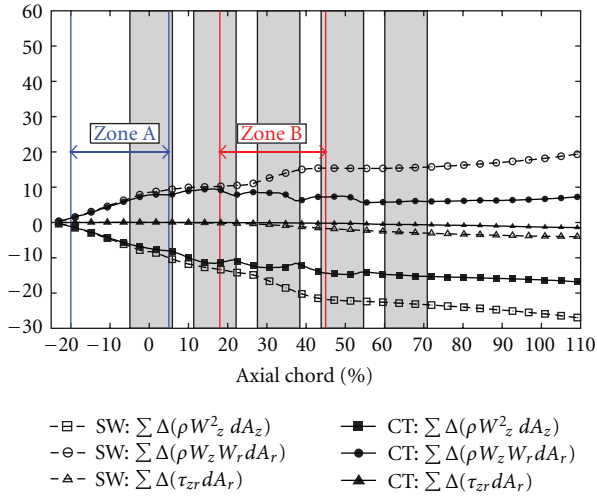


FIGURE 16: NASA Rotor 37 with and without CT: cumulative sum in the axial direction of the principal terms involved in the axial momentum equation.

unsteadiness of blade passage is weak. One reason to this phenomena might come from the ratio between the slot area and the area between the individual slots (which is very small here). Despite the high temporal resolution of the CT slot passing temporal period ( $T_{CT} = 170$  iterations), this particular test case fails to meet expectations in terms of analysis of unsteady flow interaction between the CT slots and the rotor channel. However, the effort is now focused on the analysis of local changes of the axial momentum balance in order to get more qualitative and quantitative information on the contribution of the CT slots.

**6.4. Longitudinal Evolutions of the Axial Forces and CT Contribution.** Since axial forces due to  $-\sum \Delta(\tau_{rz} A_r)$ ,  $\sum \Delta(\rho W_z W_r A_r)$ , and  $\sum \Delta(\rho W_z^2 A_z)$  highlight the change between SW and CT cases, it is interesting to investigate their respective axial evolution to further understand the flow interaction between CT and the throughflow. Figures 16 and 18 present the cumulative sum along the axial direction of these terms, respectively, for the NASA Rotor 37 and CBUAA. Figure 17 recalled from Legras et al. [37] the cumulative sum for the CREATE compressor of both steady and unsteady axial momentum balances. In the current study, only the unsteady curves are analyzed. Further comments on the difference between the steady and unsteady results are discussed in Legras et al. [37]. These diagrams provide information on the region where flow is highly constrained and on individual grooves contribution. The shaded bands denote the axial location of the casing grooves.

**6.4.1. SW Results.** Results of all SW configurations show that the efforts evolve in amplitude in a nonlinear manner along the axial direction.

The curve of viscous term  $-\Delta(\tau_{rz} A_r)$  begins to grow near the leading edge. To relate these trends to the flow physics, Figure 19(a) presents at the mid-height of the CBUAA rotor tip gap, the flow field of  $-\Delta(\tau_{rz} A_r)$ . It can be observed that the growth of  $-\Delta(\tau_{rz} A_r)$  can be relied firstly to the tip leakage vortex (referred as region A in Figure 19(a)) and secondly to the interaction of the detached shock with the shroud boundary layers (in a less pronounced manner).

Concerning the curve of the term  $\Delta(\rho W_z^2 A_z)$ , it begins to grow in negative value before the blade leading edge for the NASA Rotor 37 and CBUAA cases. Contour plots of  $\Delta(\rho W_z^2 A_z)$  in the CBUAA rotor tip gap presented. Figure 20(a) reveals that this growing trend is linked to the flow acceleration before the blade detached shock. Next, the curve slightly increases in positive values. This observation relates to the incoming flow deceleration due to its interaction with the tip leakage flow. Further downstream in the blade channel, the curve increases in negative values due to the presence of the tip leakage flow.

The curve of term  $\Delta(\rho W_z W_r A_r)$  axially evolves in “quasi-” opposite magnitude of  $\Delta(\rho W_z^2 A_z)$  curve. In fact,  $W_r$  acts here as a “coefficient of amplification.” This observation is confirmed by Figure 21(a), where contour plots are very similar to those of  $\Delta(\rho W_z^2 A_z)$  in Figure 20(a).

To resume, the SW results highlight strong axial force magnitude due to the tip leakage flow and, when a detached blade shock exists, due to the interaction between leakage flow and blade passage shock. However, the detached blade shock has a lower influence in term of force magnitude than the tip leakage flow. It explains why the axial momentum balances of CREATE (subsonic regime) and CBUAA (transonic regime) are very similar. Concerning the difference of  $\Delta(\rho W_z W_r A_r)$  and  $\Delta(\rho W_z^2 A_z)$  between NASA Rotor 37 and CBUAA, it can clearly be explained by the casing shape. In fact, the rapid growth of  $\Delta(\rho W_z W_r A_r)$  and  $\Delta(\rho W_z^2 A_z)$  curves in NASA Rotor 37 corresponds to the location of the greatest slope of the casing form.

**6.4.2. CT Results.** Results of the CT configurations clearly highlight the local contribution of the slots.

For both axi- and non-axisymmetric CT, the curve shapes of the viscous term  $-\Delta(\tau_{rz} A_r)$  are very similar to those of the SW cases, except that CT delays further downstream the beginning of the growth rate. Since this term can be relied to the tip leakage flow, this observation can be explained by an attenuation of the spread of the leakage flow perpendicular to the blade. This is confirmed when comparing Figures 19(a) and 19(b). Moreover, referring to the CBUAA histograms in Figure 13, CT configuration shows higher magnitude of viscous term  $-\Delta(\tau_{rz} A_r)$ . In fact, contour plots in Figure 19(b) indicate the presence of a second region of high viscous axial force denoted B and located along the rear part of the CT slots. As seen by Legras et al. [44], this part of the slot is responsible for flow bleeding, whereas at the front part the recirculated flow is reinjected into the throughflow. This observation suggests that the flow bleeding mechanism induces strong shear layer that can

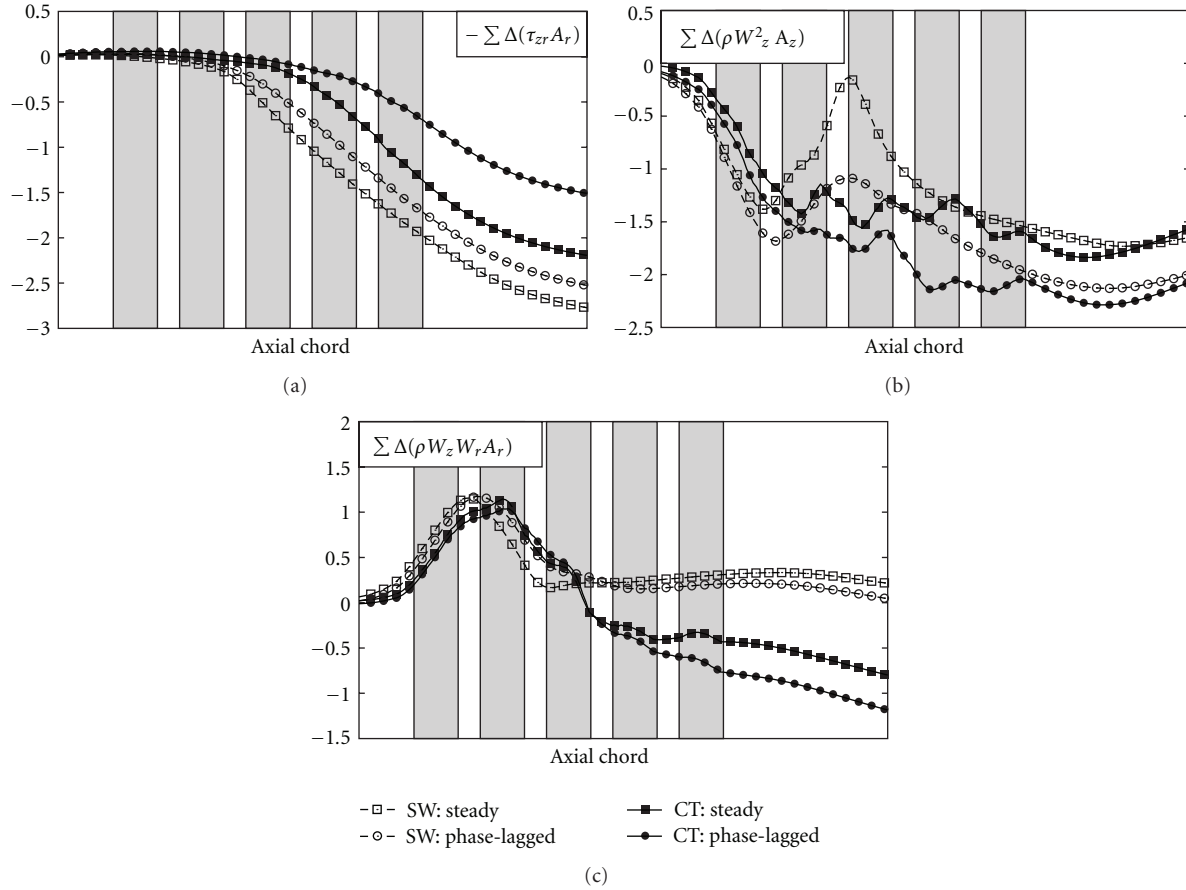


FIGURE 17: CREATE-R2 with and without CT: cumulative sum in the axial direction of the principal terms involved in the axial momentum equation [37].

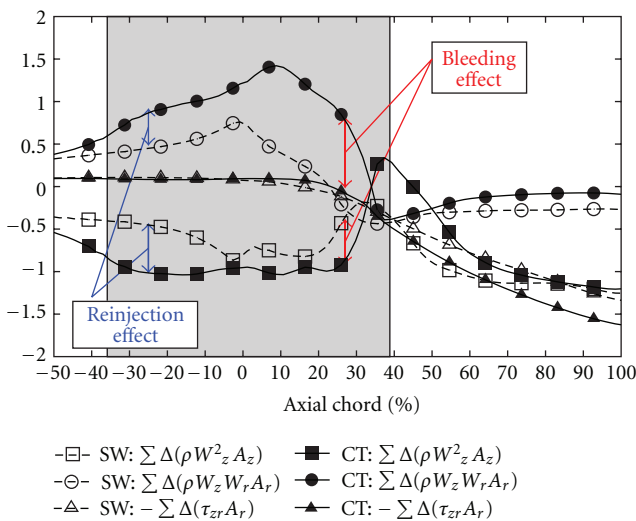


FIGURE 18: CBUAA with and without CT: cumulative sum in the axial direction of the principal terms involved in the axial momentum equation.

increase viscous losses, thus explaining the efficiency losses observed with the use of the slot-type CT.

The CT effects are even more highlighted by the curve of  $\Delta(\rho W_z W_r A_r)$ . In fact, one can notice that axisymmetric CTs in NASA Rotor 37 and CREATE cases create an axial force  $\Delta(\rho W_z W_r A_r) < 0$  in opposite direction to the flow advance. This explains the change observed in the previous histograms (Figures 11 and 12). This creation of axial force  $\Delta(\rho W_z W_r A_r) < 0$  can be relied to the bleeding effect of the grooves since  $W_r > 0$  has been observed in previous studies [9, 37]. Moreover, this kind of analysis permits to identify the groove effectiveness depending on its capability to create this previous axial force, thus a bleeding effect. For the NASA Rotor 37, results show that the 2nd, 3rd, and 4th grooves are useful at the last stable point numerically seen for SW configuration. For the CREATE, Legras et al. [37] conclude that the 3rd groove is efficient at the last stable point numerically seen for SW configuration.

Concerning the CBUAA slot-type CT, the bleeding effect along the rear part of the CT slots creates an axial force  $\sum \Delta(\rho W_z W_r A_r) < 0$  directed along the flow advance. This observation is confirmed by Figure 21(a) and is referred as

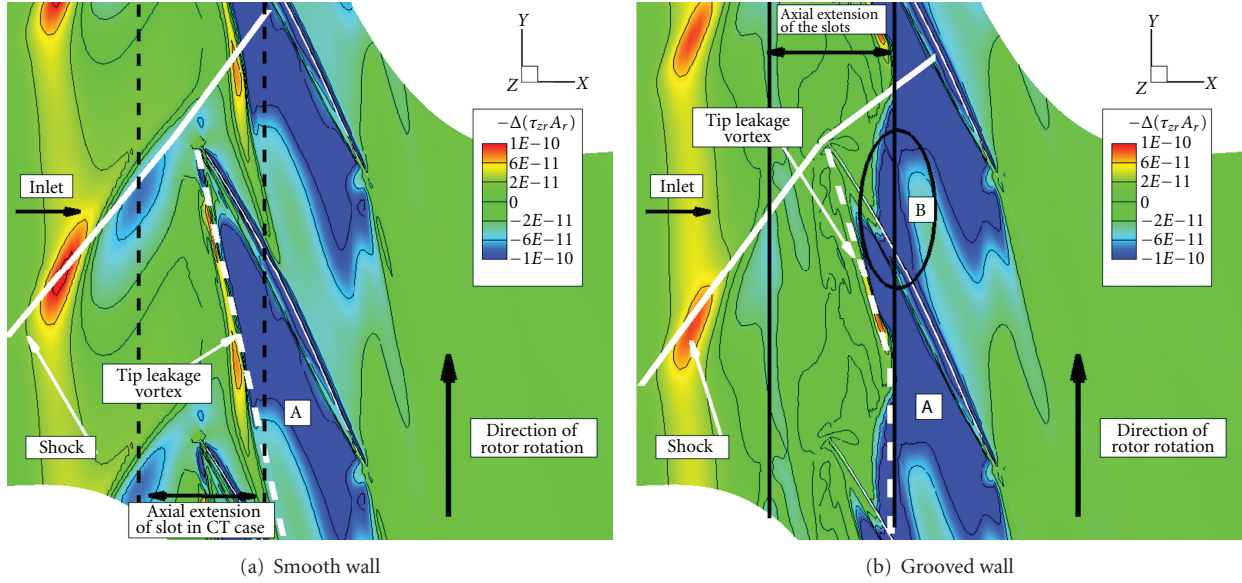


FIGURE 19: CBUAA: Flow field denoted at midgap by negative values of  $-\Delta(\tau_{zr}A_r)$ .

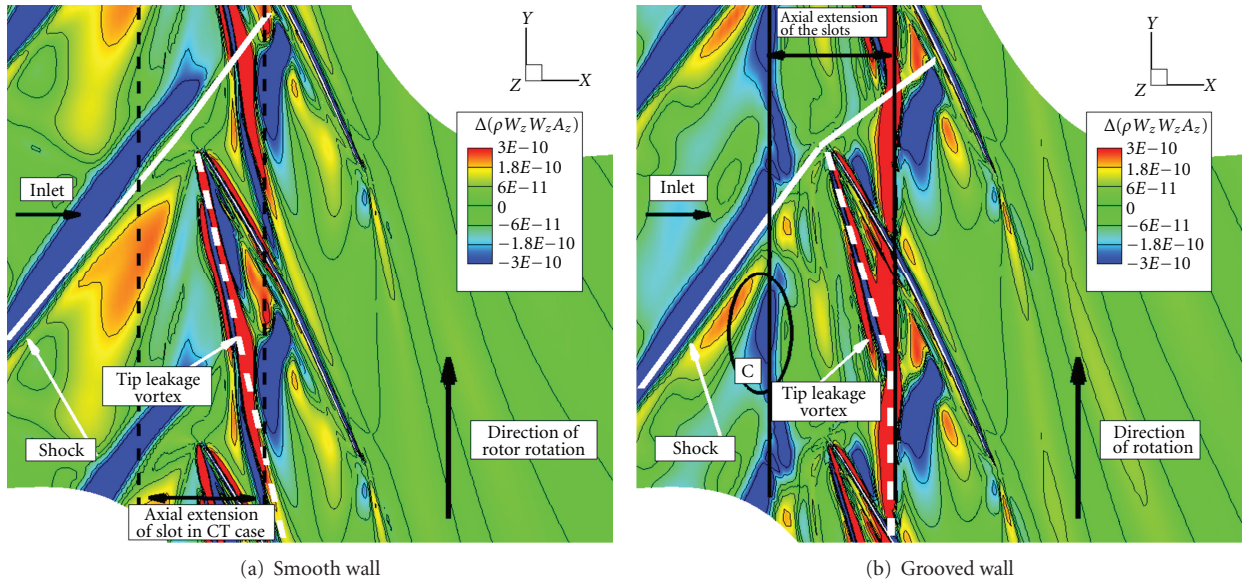


FIGURE 20: CBUAA: Flow field denoted at midgap by negative values of  $\Delta(\rho W_z^2 A_z)$ .

zone D. As a matter of fact, the bleeding mechanisms of slot-type CT have a relatively similar effect than observed with circumferential CT. This is consistent with the general conclusions that previous studies have found that the reverse tip leakage flow through the tip gap got pushed into the grooves by the reinjecting flow (in main flow direction) from the grooves. On the contrary, the flow blowing mechanism along the front part of the CT induces axial force of  $\sum \Delta(\rho W_z W_r A_r) > 0$  acting in opposite direction to the flow advance (referred as zone C in Figure 21(a)). In fact, the reinjected flow tends to radially deviate the incoming flow.

Concerning the term of  $\Delta(\rho W_z^2 A_z)$ , curves mainly evolve in opposite magnitude to the term  $\sum \Delta(\rho W_z W_r A_r)$ . Moreover, results of CBUAA with slot-type CT indicate that the blowing mechanism at the CT front part creates an axial force  $\Delta(\rho W_z^2 A_z) < 0$  in the direction to the flow advance (see Figure 20(b), zone C). This observation suggests that the near casing flow is further accelerated. This is consistent with previous studies that the reinjected flow energizes the near casing flow. On the contrary, the flow bleeding mechanism creates an axial force  $\Delta(\rho W_z^2 A_z) > 0$  in the opposite direction to the flow advance. This is consistent since the near

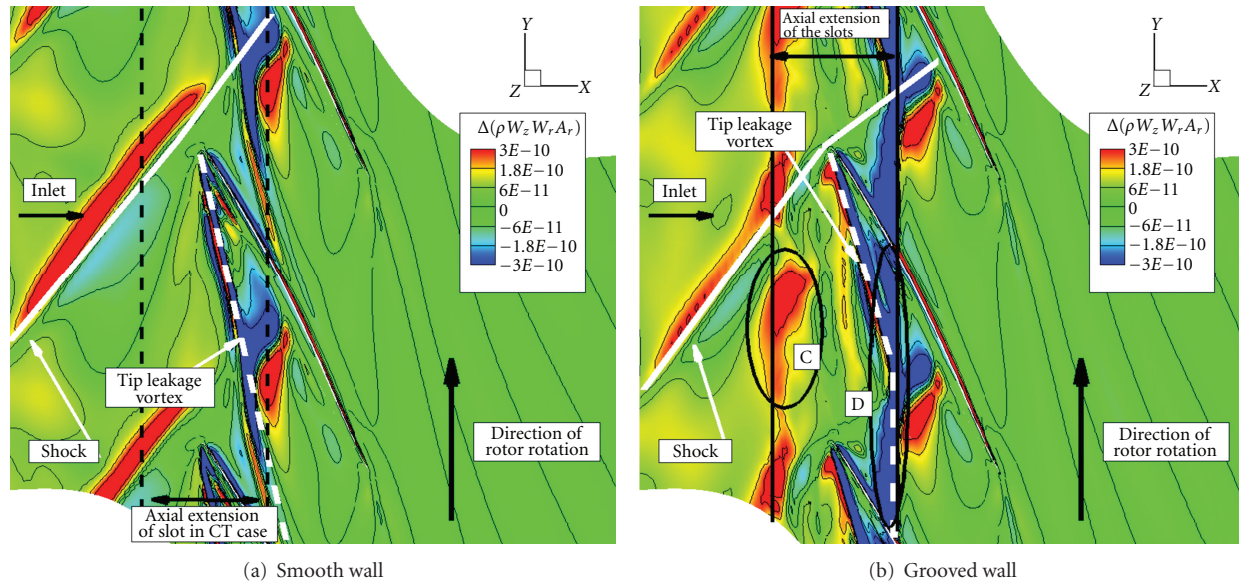


FIGURE 21: CBUAA: Flow field denoted at midgap by negative values of  $\Delta(\rho W_z W_r A_r)$ .

casing flow bled lost its axial velocity in order to be radially deflected into the CT slots.

**6.5. Recommendation on the Useful Interpretation of the CT Flow Mechanisms Using the ESA Model.** The analysis of the slot-type CT of the CBUAA compressor shows the limitation of the use of the histograms as a tool to investigate CT flow mechanisms. In fact, the histograms present a global overview of the forces being applied on a rotor tip control volume. They tend to “smooth” the local effect of CT flow mechanisms (mainly both bleeding and blowing mechanisms). For an analysis of axisymmetric CT, histograms can be useful, whereas for slot-type CT the histograms prove to be not sufficient. Thus, one has to take care of the interpretation of the histograms. The main interest of the model comes from the analysis of the longitudinal evolutions of the axial forces since it permits to reveal the local CT flow mechanisms as well as the CT individual grooves’ contribution. So, it is recommended to perform both global and local analysis using the ESA model in order to further understand the flow mechanisms induced by CT.

## 7. Conclusion

This paper has presented a generalized method of the Shabbir and Adamczyk approach for uncovering the flow mechanisms induced by casing treatment (CT) using CFD numerical simulations. Compared to Shabbir’s approach, this method permits to analyze any CT geometry, thanks to a budget analysis of each of the Navier-Stokes (un)steady momentum equations. In the current paper, only the equilibrium of the axial momentum equations is analyzed since it describes the global flow across the rotor channel, specially its

pressure rise. The novel method has been used to investigate the flow interaction between axi and non-axisymmetric CT and the throughflow for three different axial compressors. They differ by the flow regime (subsonic/transonic), the untreated casing shape (cylindrical/conical), and the CT implemented (axi-/non axisymmetric CT).

The comparison of the three compressors indicates that axisymmetric CT is characterized by its flow bleeding effect that creates an axial force  $\Delta(\rho W_z W_r A_r) < 0$ . It is shown that the benefit of this force on the flow stability is more dependant on the casing shape than the flow regime. Concerning slot-type CT, it is characterized by both a bleeding effect at the rear part, which creates an axial force  $\Delta(\rho W_z W_r A_r) < 0$ , and a blowing effect at the front part that energizes the near casing flow by creating axial force  $\Delta(\rho W_z^2 A_z) < 0$ . However, its strong bleeding effect is responsible of additional viscous losses explaining the efficiency losses observed with the use of slot-type CT. These conclusions are rather difficult to be stated from the only histograms. Thus, it is strongly recommended to focus on the axial distribution of the axial forces to further understand the interaction between the CT and the flow. Furthermore, since both axi- and non-axisymmetric CT create an axial force  $\Delta(\rho W_z W_r A_r) < 0$ , it lends support that the radial velocity component  $W_r$  is of a main interest for the stability of the tip flow.

The current analysis methodology proved its potential to help in the designing of CT. However, there are still many questions on the understanding of the CT mechanisms that the model can answer. The main perspectives concern

- (i) the analysis of tangential momentum: since the tangential force is the main force of compressors, it could be interesting to investigate the influence of CT,

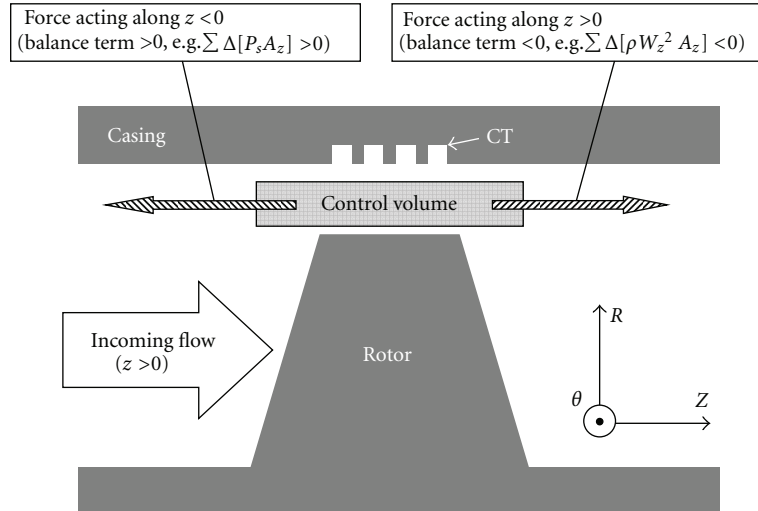


FIGURE 22: Nomenclature and sketch of the axial forces acting on a control volume located in the rotor tip clearance.

- (ii) the analysis of the balance at part speed,
- (iii) the resolution of the momentum equation in the streamline reference frame rather than cylindrical.

Finally, it can also be easily used to uncover the flow mechanisms in order to design a large panel of flow passive control devices: film cooling, and boundary layer aspiration in the turbomachinery field as well as for aircraft or helicopter applications.

## Nomenclature

### Symbols

<b>A:</b>	Surface area of a grid cell = $[A_r, A_\theta, A_z]^T$
$E_r$ :	Relative energy
$F_{cen}$ :	Centrifugal force
$F_{cor}$ :	Coriolis force
$F_{\lambda_{2,4}}$ :	2nd- and 4th-order numerical scalar artificial dissipation fluxes
$\dot{m}$ :	Mass flow rate
$P_s$ :	Static pressure
<b>q:</b>	Heat flux vector = $[q_r, q_\theta, q_z]^T$
<b>Q:</b>	Conservative variable
<b>R:</b>	Numerical modelling residual
$R$ :	Number of rotor row
$Rpi$ :	Total-to-total pressure ratio
$r, \theta, z$ :	Cylindrical coordinates
$S$ :	Number of stator row
$t$ :	Time

<b>V:</b>	Volume of the control domain
<b>V:</b>	Absolute velocity = $[V_r, V_\theta, V_z]^T$
<b>W:</b>	Relative velocity = $[W_r, W_\theta, W_z]^T$ .

### Greek Letters

$\eta_{is}$ :	Isentropic efficiency
$\gamma$ :	Specific heat ratio
$\mu$ :	Molecular dynamic viscosity
$\omega$ :	Rotation speed
$\rho$ :	Density
$\tau$ :	Sum of the viscous and turbulence stress tensor.

### Abbreviation

CBUAA:	Compressor of the Beijing University of Aeronautics & Astronautics
CT:	Casing treatment
ESA:	Extended Shabbir and Adamczyk model
SW:	Smooth wall.

## Acknowledgments

The authors are grateful to Snecma, SAFRAN Group, for permission to publish results. Special thanks to LMFA and the CERFACS-CFD team for their computational facilities as well as for their availability for discussions concerning numerical methods and physical analysis. The authors are also grateful to the *elsA* software team (ONERA).

## References

- [1] E. M. Greitzer, J. P. Nikkanen, D. E. Haddad, R. S. Mazzawy, and H. D. Joslyn, "Fundamental criterion for the application of rotor casing treatment," *Journal of Fluids Engineering*, vol. 101, no. 2, pp. 237–243, 1979.
- [2] D. C. Rabe and C. Hah, "Application of casing circumferential grooves for improved stall margin in a transonic axial compressor," in *Proceedings of the ASME Turbo Expo: Turbomachinery*, paper GT2002-30641, pp. 1141–1153, June 2002.
- [3] A. Shabbir and J. J. Adamczyk, "Flow mechanism for stall margin improvement due to circumferential casing grooves on axial compressors," *Journal of Turbomachinery*, vol. 127, no. 4, pp. 708–717, 2005.
- [4] V. Perrot, A. Touyeras, and G. Lucien, "Detailed cfd analysis of a grooved casing treatment on an axial subsonic compressor," in *Proceedings of the 7th European Turbomachinery Conference*, 2007.
- [5] M. W. Müller, H. P. Schiffer, and C. Hah, "Effect of circumferential grooves on the aerodynamic performance of an axial single-stage transonic compressor," in *Proceedings of the ASME Turbo Expo*, paper GT2007-27365, pp. 115–124, May 2007.
- [6] M. W. Müller, C. Biela, and H. P. Schiffer, "Interaction of rotor and casing treatment flow in an axial single-stage transonic compressor with circumferential grooves," in *Proceedings of the ASME Turbo Expo*, paper GT2008-50135, pp. 67–78, June 2008.
- [7] T. Houghton and I. Day, "Enhancing the stability of subsonic compressors using casing grooves," in *Proceedings of the ASME Turbo Expo*, paper GT2009-59210, pp. 39–48, June 2009.
- [8] G. Legras, N. Gourdain, and I. Trébinjac, "Numerical analysis of the tip leakage flow field in a transonic axial compressor with circumferential casing treatment," *Journal of Thermal Science*, vol. 19, no. 3, pp. 198–205, 2010.
- [9] G. Legras, N. Gourdain, and I. Trébinjac, "Extended methodology for analysing the flow mechanisms induced by casing treatment in compressor," in *Proceedings of the 9th of European Turbomachinery Conference*, 2011.
- [10] I. Wilke and H. P. Kau, "A numerical investigation of the flow mechanisms in a high pressure compressor front stage with axial slots," *Journal of Turbomachinery*, vol. 126, no. 3, pp. 339–349, 2004.
- [11] I. Wilke, H. P. Kau, and G. Brignole, "Numerically aided design of a high-efficient casing treatment for a transonic compressor," in *Proceedings of the ASME Turbo Expo*, paper GT2005-68993, pp. 353–364, Reno, Nev, USA, June 2005.
- [12] N. Gourdain and F. Leboeuf, "Unsteady simulation of an axial compressor stage with casing and blade passive treatments," *Journal of Turbomachinery*, vol. 131, no. 2, pp. 1–12, 2009.
- [13] M. Vogues, R. Schnell, C. Willert, R. Monig, M. W. Müller, and C. Zscherp, "Investigation of blade tip interaction with casing treatment in a transonic compressor. Part I: Particle image velocimetry," *ASME Journal of Turbomachinery*, vol. 133, no. 1, Article ID 011007, 2011.
- [14] R. Schnell, M. Voges, R. Mönig, M. W. Müller, and C. Zscherp, "Investigation of blade tip interaction with casing treatment in a transonic compressor-part II: numerical results," *Journal of Turbomachinery*, vol. 133, no. 1, Article ID 011008, 2011.
- [15] M. D. Hathaway, "Self-recirculating casing treatment concept for enhanced compressor performance," in *Proceedings of the ASME Turbo Expo: Turbomachinery*, paper GT-2002-30368, pp. 411–420, June 2002.
- [16] H. Yang, D. Nuernberger, E. Nicke, and A. Weber, "Numerical Investigation of Casing Treatment Mechanisms with a Conservative Mixed-Cell Approach," in *ASME Turbo Expo*, paper GT2003-38483, pp. 961–974, June 2003.
- [17] A. J. Strazisar, M. M. Bright, S. Thorp, D. E. Culley, and K. L. Suder, "Compressor stall control through endwall recirculation," in *Proceedings of the ASME Turbo Expo*, paper GT2004-54295, pp. 655–667, June 2004.
- [18] N. Gourdain, X. Ottavy, and F. Wlassow, "Effect of Tip Clearance Dimensions and Control of Unsteady Flows in a Multi-Stage High Pressure Compressor," *Journal of Turbomachinery*. In press.
- [19] M. D. Hathaway, "Passive endwall treatments for enhancing stability," VKI LS 2006-06 on Advances in Axial Compressor Aerodynamics, 2007.
- [20] J. Dunham, "CFD validation for propulsion system components (la validation CFD des organes des propulseurs)," Tech. Rep. number ISBN 92-836-1075-X, AGARD Advisory Report 355, 1998.
- [21] A. Jameson, R. F. Schmidt, and E. Turkel, "Numerical Solutions of the Euler equations by finite volume methods using Runge-Kutta time stepping," AIAA paper AIAA-81-1259, 1981.
- [22] F. Lin, F. Ning, and H. Liu, "Aerodynamics of compressor casing treatment part I : experiment and time-accurate numerical simulation," in *Proceedings of the ASME Turbo Expo*, paper GT2008-51541, pp. 731–743, June 2008.
- [23] J. Ratzlaff, P. D. Orkwis, C. Noll, and G. Steuber, "Analysis of lumped deterministic source terms and their sub-components in a stage 1 high pressure turbine rotor," in *Proceedings of the ASME Turbo Expo*, paper GT2008-51473, pp. 2693–2703, June 2008.
- [24] L. Reid and R. Moore, "Design and overall performance of four highly loaded high-speed inlet stages for 19 an advanced high pressure ratio core compressor," Tech. Rep. TP 1337, NASA Lewis Research Center, 1978.
- [25] R. D. Moore and L. Reid, "Performance of single-stage axial-flow transonic compressor with rotor and stator aspect ratios of 1.19 and 1.26, respectively, and with design pressure ratio of 2.05," *NASA Technical Paper*, no. 1659, 1980.
- [26] A. Touyeras and M. Villain, "Aerodynamic design and test result analysis of a three stage research compressor," in *Proceedings of the ASME Turbo Expo*, paper GT2004-53940, pp. 589–597, June 2004.
- [27] F. Ning and L. Xu, "Aerodynamics of compressor casing treatment Part II: a quasi-steady model for casing treatment flows," in *Proceedings of the ASME Turbo Expo*, paper GT2008-51542, pp. 745–755, June 2008.
- [28] K. L. Suder and M. L. Celestina, "Experimental and computational investigation of the tip clearance flow in a transonic axial compressor rotor," *Journal of Turbomachinery*, vol. 118, no. 2, pp. 218–229, 1996.
- [29] R. V. Chima, "Calculation of tip clearance effects in a transonic compressor rotor," *Journal of Turbomachinery*, vol. 120, no. 1, pp. 131–140, 1998.
- [30] J. D. Denton, "Lessons from rotor 37," in *Proceedings of the 3rd International Symposium on Experimental and Computational Aerothermodynamics of Internal Flows (ISAI'96)*, 1996.
- [31] Wilke I., *Verdichterstabilisierung mit passiven Gehäusestrukturen—eine numerische analyse*, Ph.D. thesis, Technischen Universität München, 2005.
- [32] D. Arnaud, X. Ottavy, and A. Vouillarmet, "Experimental investigation of the rotor-stator interactions, within a high speed, multi-stage, axial compressor part 1—Experimental

- facilities and results,” in *Proceedings of the ASME Turbo Expo*, paper GT2004-53764, pp. 903–914, June 2004.
- [33] D. Arnaud, X. Ottavy, and A. Vouillarmet, “Experimental investigation of the rotor-stator interactions within a high-speed, multi-stage, axial compressor. Part 2. Modal analysis of the interactions,” in *2004 ASME Turbo Expo*, pp. 915–924, aut, June 2004.
- [34] V. Sharma, M. Schvallinger, J. Marty et al., “Turbulence modelling effects on off-design predictions for a multistage compressor,” in *Proceedings of the 18th International Symposium on Air Breathing Engines (ISABE’07)*, p. 1183, 2007.
- [35] J. Marty, G. Cottin, and B. Aupoix, “Turbulence modelling and transition to turbulence effects for a high pressure multistage compression,” in *Proceedings of the 8th European Turbomachinery Conference*, 2009.
- [36] N. Gourdain, X. Ottavy, and A. Vouillarmet, “Experimental and numerical investigation of unsteady flows in a high speed three stages compressor,” in *Proceedings of the 8th European Turbomachinery Conference*, 2009.
- [37] G. Legras, N. Gourdain, I. Trébinjac, and X. Ottavy, “Analysis of Unsteadiness on Casing Treatment Mechanisms in an Axial Compressor,” in *Proceedings of the ASME Turbo Expo*, ASME paper GT2011-46806, 2011.
- [38] L. Cambier and J. P. Veuillot, “Status of the elsA CFD software for flow simulation and multidisciplinary applications,” in *Proceedings of the 46th AIAA Aerospace Sciences Meeting and Exhibit*, January 2008.
- [39] L. Castillon, S. Péron, and C. Benoit, “Numerical simulations of technological effects encountered on turbomachinery configurations with the chimera technique,” in *Proceedings of the 27th Congress of the International Council of the Aeronautical Sciences (ICAS’10)*, paper 088, 2010.
- [40] J. I. Erdos, E. Alzner, and W. McNally, “Numerical solution of periodic transonic flow through a fan stage,” *AIAA Journal*, vol. 15, no. 11, pp. 1559–1568, 1977.
- [41] G. A. Gerolymos, G. J. Michon, and J. Neubauer, “Analysis and application of chorochronic periodicity in turbomachinery rotor/stator interaction computations,” *Journal of Propulsion and Power*, vol. 18, no. 6, pp. 1139–1152, 2002.
- [42] L. Castillon and G. Legras, “An unsteady overset grid method for the simulation of compressors with non circumferential casing treatments,” in *Proceedings of the 20th International Symposium on Air Breathing Engines (ISABE’11)*, 2011.
- [43] D. C. Wilcox, “Reassessment of the scale-determining equation for advanced turbulence models,” *AIAA Journal*, vol. 26, no. 11, pp. 1299–1310, 1988.
- [44] G. Legras, L. Castillon, I. Trébinjac, and N. Gourdain, “Flow mechanisms induced by non-axisymmetric casing treatment in a transonic axial compressor,” in *Proceedings of the 10th International Symposium on Experimental and Computational Aerothermodynamics of Internal Flows (ISAI’11)*, 2011.
- [45] B. H. Beheshti, J. A. Teixeira, P. C. Ivey, K. Ghorbanian, and B. Farhanieh, “Parametric study of tip clearance—casing treatment on performance and stability of a transonic axial compressor,” *Journal of Turbomachinery*, vol. 126, no. 4, pp. 527–535, 2004.
- [46] C. Haixin, F. Song, and X. Huang, “CFD Investigation on Tip Leakage Flow and Casing Treatment of a Transonic Compressor,” in *Proceedings of the 17th International Symposium on Air Breathing Engine*, 2005.
- [47] H. Xudong, C. Haixin, and F. Song, “CFD Investigation on the circumferential grooves casing treatment of transonic compressor,” in *Proceedings of the ASME Turbo Expo*, paper GT2008-51107, pp. 581–588, June 2008.

## Research Article

# Reciprocating Compressor 1D Thermofluid Dynamic Simulation: Problems and Comparison with Experimental Data

A. Gimelli,<sup>1</sup> A. Rapicano,<sup>1</sup> F. Barba,<sup>2</sup> and O. Pennacchia<sup>1</sup>

<sup>1</sup>Dipartimento di Meccanica ed Energetica (DiME), Università Degli Studi di Napoli Federico II, 80125 Napoli, Italy

<sup>2</sup>Facoltà di Ingegneria, Università Degli Studi di Napoli Federico II, 80125 Napoli, Italy

Correspondence should be addressed to A. Gimelli, gimelli@unina.it

Received 9 February 2012; Revised 27 March 2012; Accepted 31 March 2012

Academic Editor: Ryo Amano

Copyright © 2012 A. Gimelli et al. This is an open access article distributed under the Creative Commons Attribution License, which permits unrestricted use, distribution, and reproduction in any medium, provided the original work is properly cited.

The authors here extend a 0D-1D thermofluid dynamic simulation approach to describe the phenomena internal to the volumetric machines, reproducing pressure waves' propagation in the ducts. This paper reports the first analysis of these phenomena in a reciprocating compressor. The first part presents a detailed experimental analysis of an open-type reciprocating compressor equipped with internal sensors. The second part describes a 0D-1D thermofluid dynamic simulation of the compressor. Comparison of computed and measured values of discharge mass flow rate shows a good agreement between results for compression ratio  $\beta < 5$ . Then, to improve the model fitting at higher pressures, a new scheme has been developed to predict the blow-by through the ring pack volumes. This model is based on a series of volumes and links which simulate the rings' motions inside the grooves, while the ring dynamics are imposed using data from the literature about blow-by in internal combustion engines. The validation is obtained comparing experimental and computing data of the two cylinder engine blowby. After the validation, a new comparison of mass flow rate on the compressor shows a better fitting of the curves at higher compression ratio.

## 1. Introduction

*1.1. Background.* Volumetric compressors, alternative and rotary, represent an element of large utilities in the domestic field as in industrial applications, in particular, the refrigeration cycle [1, 2]. In today's world, energy optimization is of the utmost importance, therefore, it is crucial to find tools which can support the planning phase to increase the efficiency of these machines. Imagine, that approximately 11% of the produced electrical energy today is destined to power domestic refrigeration [3]. Reported in this paper is a method for the simulation of 0D-1D fluid-dynamic phenomena which occurs in the volumetric machines, noting the results from a study of problems linked to volumetric reciprocating engine, that in the future will be extended also to rotary. For years, the most widely used and reliable approach was the empirical one [4], because of the complexity of physical phenomena that takes place in the thermal machines. This occurs because the functioning at full performance of a volumetric compressor is not stationary but periodic; equations that govern the mass

transport in the pipelines are not linear, so they cannot be resolved through an analytic method. However, the development of computing potential and of theoretical-numeric methods suggest a new approach, based on the use of fluid-dynamic models. These models are divided into a different kind of sophistication. Depending on the user's needs, there are semiempirical models, whose equations are studied on the results of a focused experimentation [3], simplified analytics models, quite common in the industrial field [2] as they describe the compressor overall. Finally, there are more thorough models [4–6], governed by differential not stationary equations linked to the individual volumes in which the machine is divided. The thorough models are very important in the research field as they allow us to study many phenomena which take place inside the machine. For example, it was proved that the pressure waves that travel through the discharge pipes, governed also by the dynamics of automatic or controlled valves [7, 8], are a major source of noise radiation from reciprocating compressors. The detection of these parameters which govern these pulsations can lead to the development of instruments which could

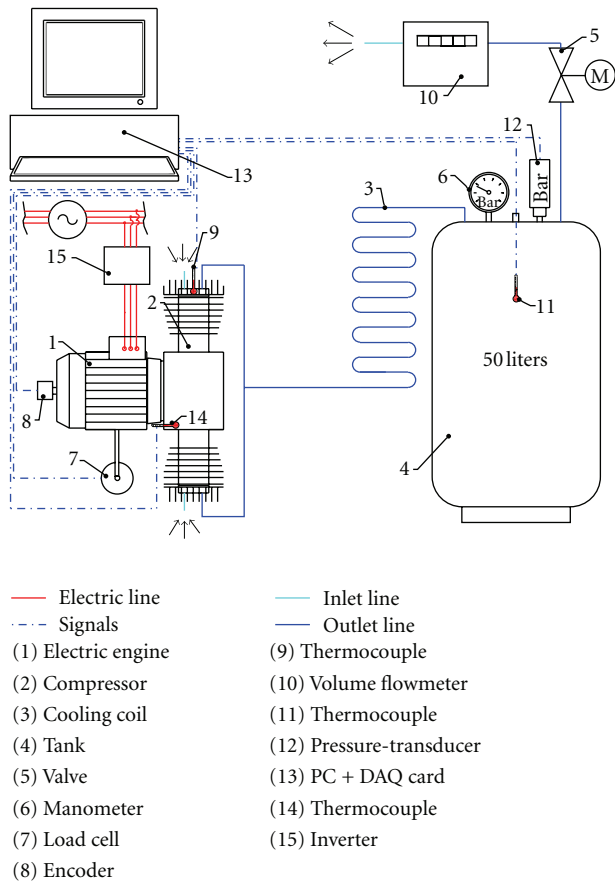


FIGURE 1: Test bed layout.

reduce this noise radiation. Thanks to this kind of approach, a substantial reduction of cost and development time can be obtained, allowing in just a short time a sensitivity analysis to the many functional and structural parameters showing the best solutions to be tested experimentally.

*1.2. Targets of the Thermo-fluid Dynamic Simulation.* In this perspective, during the last two decades [6, 9–25], a 0D-1D fluid-dynamic simulation software was developed at DiME for the alternative internal combustion engine. Based on the resolution of flow equations in the pipes out of the cylinders, adopting a one-dimensional schematization, while the capacity in variable volume condition (the cylinder) is resolved through a zero-dimensional approach, it was considered that variables do not change on a spatial coordinate, but they are only a function of time. Through the use of this tool, in the first part of this work, a new scheme for the simulation of a V-twin compressor was proposed, starting from the knowledge of the construction features of the machine. In particular, the layout of a test bed was reproduced, on which the stationary tests were carried out, having provided the average values of pressure, temperature, and airflow at the outlet. The comparison between the experimental and simulated values has allowed a first check of the results to be obtained. Then, the “blow-by” has been studied, which is the phenomenon of gas leakage

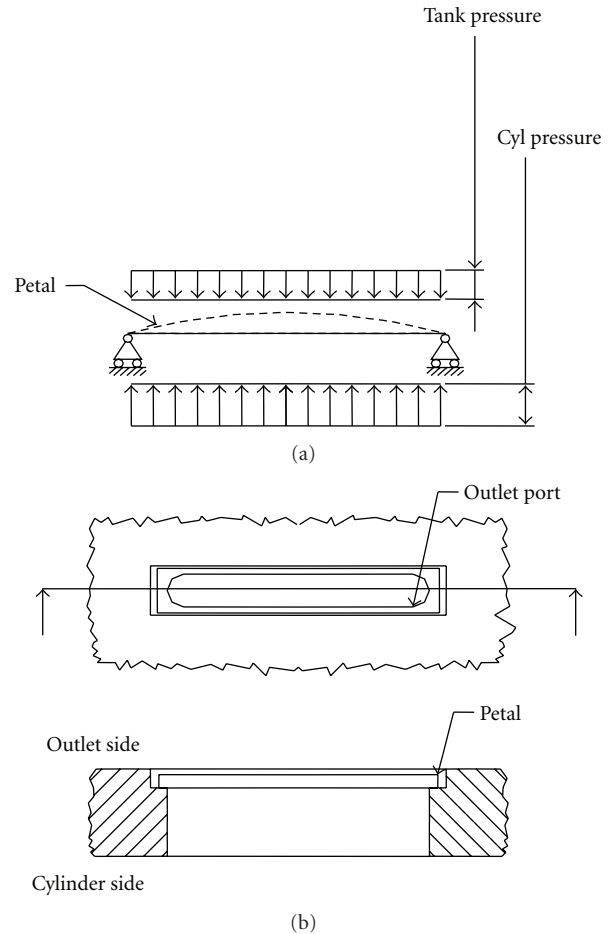


FIGURE 2: (a) Reed valve deflection, (b) outlet valve.

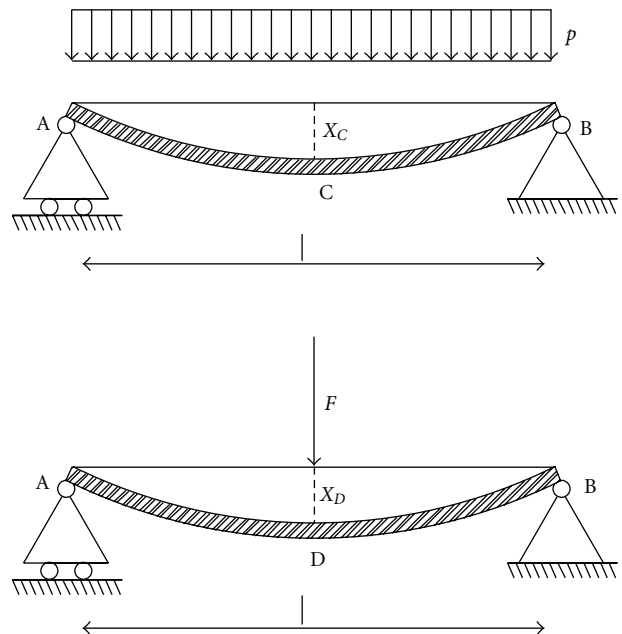


FIGURE 3: Deflection of a simply supported beam under uniformly distributed and concentrated load.

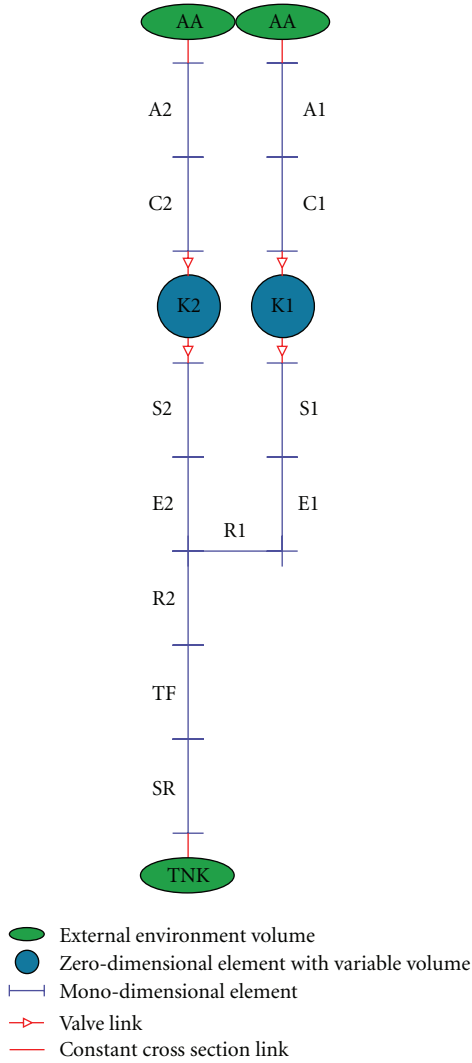


FIGURE 4: Geometric layout of the compressor.

that takes place between the compression chamber and the crankcase as a result of the clearance between piston, cylinder liner, and rings. To this end, starting from [8] and from the current knowledge about the rings dynamic inside the internal combustion engine [26], a model for the simulation of “blow-by” inside the compressors has been implemented. The targets to achieve here were as follows:

- (i) to improve the predictability of the 0D-1D model introducing a scheme which considers the leakage in cylinders in the volumetric compressors,
- (ii) to provide an indicative framework of the fluid dynamic phenomena which take place inside the piston sealing system, also in relation to the segments dynamic,
- (iii) to suggest a new approach to volumetric machine simulation taking into account the leakage phenomena that is not negligible, especially in the rotary machines.

## 2. Experimental Setup

The compressor which is the object of this theoretical and experimental analysis is a FIAC V254, a twin reciprocating v-unit with its total displacement being  $165 \text{ cm}^3$ . Figure 1 represents the layout of the equipment with which the tests were made. The compressor (2) is moved by a three-phase asynchronous electric motor (1) of 2.2 kW lead to the nominal speed of 1500 rpm through an inverter (15). Motor and compressor are connected by a flexible coupling. The compressor feeds a 50 liter tank (4).

A cooling coil (3) is placed between the compressor and the tank to cool down the air mass flow before it reaches the tank. Downstream of the heat exchanger is placed in a manual lamination valve (5) which is necessary both to perform constant pressure tests and to empty the tank at the end of the session. After which the lamination valve is placed in a volumetric flowmeter (10). In Table 1, data are collected in 10 stationary tests, with each test featuring a constant pressure in the tank [27].

## 3. Numerical Models: The Code

A computer code recently developed by DiME researchers has been employed, for the evaluation of component matching and estimation of the in-cylinder and in-pipe processes [6, 9–25]. The code, being of a modular type, can easily handle different engine configurations (i.e., single or multicylinder compression-ignition engines [13–15], two-stroke spark-ignition engines [6, 10, 11, 19, 24], such as four strokes, either aspirated or supercharged [18, 20, 22, 23], etc.). Moreover, three-dimensional models in the cylinder have been integrated such as the KIVA [15–17, 22, 24], to evaluate the 3D phenomena in a transient state.

*0D Model.* A filling and emptying technique is adopted for calculating the time-varying conditions inside variable volume devices (i.e., cylinders, displacement compressors, etc.) The general formulation of the governing equations for mass and energy balance within a control volume is shown below. Particular care was paid to the determination of gas properties: The mass equation has been split into three equations (1), (2), and (3), which, respectively, take into account the total mass balance and those of residual and fuel mass fractions:

$$\dot{m} = \dot{m}_f^{\text{inj}} + \sum_i \dot{m}_i^{\text{vlv}}, \quad \dot{m} = \dot{m}_a + \dot{m}_r + \dot{m}_f, \quad (1)$$

$$\dot{m}_r = \sum_i \dot{m}_{r,i}^{\text{vlv}} + \dot{m}_f^{\text{cmb}} \left( \frac{1 + f_{\text{st}}}{f_{\text{st}}} \right), \quad (2)$$

$$\dot{x}_r = \frac{1}{m} (\dot{m}_r - x_r \dot{m}), \quad x_r = \frac{m_r}{m},$$

$$\dot{m}_f = \dot{m}_f^{\text{inj}} + \sum_i \dot{m}_{f,i}^{\text{vlv}} - \dot{m}_f^{\text{cmb}}, \quad (3)$$

$$\dot{x}_f = \frac{1}{m} (\dot{m}_f - x_f \dot{m}), \quad x_f = \frac{m_f}{m}.$$

TABLE 1: Experimental data.

Test number	$p_{\text{amb}}$ (bar)	$T_{\text{amb}}$ (K)	$n$ (rpm)	$P_{\text{tnk}}$ (bar)	$T_{\text{oil}}$ (K)
9	1.017	299	1487	9.998	340
8	1.017	299	1498	9.019	331
7	1.017	299	1495	8.010	340
6	1.017	299	1493	7.024	337
5	1.017	299	1494	6.019	335
4	1.017	299	1504	5.045	331
3	1.017	299	1497	3.994	328
2	1.017	299	1495	2.998	324
1	1.017	299	1506	2.017	321
0	1.017	299	1506	1.199	318

The energy equation was properly rearranged with a correct gas mixture property calculation:

$$\dot{T} = \frac{(1/m) \left[ -p\dot{V} - \dot{Q}_w + \dot{m}_f^{\text{inj}} h_f^{(o)} + \sum_i \dot{m}_i h_i^{\text{lv}} - \dot{e}m - m(\partial e/\partial x_r)\dot{x}_r \right] - \left( (p/A_p)(\partial e/\partial p) \right) (\dot{m}/m - \dot{V}/V + ((1/R)(\partial R/\partial x_r))\dot{x}_r)}{c_v + (p/T)(A_T/A_p)(\partial e/\partial p)}, \quad (4)$$

$$\left( \text{being } A_p = 1 - \frac{p}{R} \frac{\partial R}{\partial p}; A_T = 1 + \frac{T}{R} \frac{\partial R}{\partial T} \right), \quad p = \frac{mRT}{V}. \quad (5)$$

The system of equations (1)–(5), written for each control volume, is solved at each time step by a fourth-order Runge-Kutta scheme. The same technique is employed for a preliminary evaluation of conditions inside intake and exhaust systems.

The system of equations, written for each control volume, is solved at each time step by a fourth-order Runge-Kutta scheme.

*1D Flow Model.* As widely described in the quoted papers, this model is based on a one-dimensional unsteady compressible flow through external ducts, therefore, being able to characterize the wave propagation which controls the filling of each cylinder. The mass, momentum, and energy balance equations in conservative form (6) are solved with the TVD method [9, 28]. The terms  $\rho$ ,  $u$ ,  $p$ ,  $E = c_v T + u^2/2$ ,  $H = c_p T + u^2/2$  in the equation system (6) are, respectively, density, velocity, pressure, energy, and total enthalpy per mass unit.

Further balance equations for the chemical species and  $x_r$  and  $x_f$ , which indicate the mass fractions of exhaust gas and fuel, are written to evaluate the gas mixture when the aspiration valve closes. The system is solved by using a “thermodynamic state” table for the simulated gas, this table is included in the software.

The vector of source terms,  $\mathbf{S}$ , takes into account the effects of the variable section  $\Omega$  of the duct ( $\alpha = (1/\Omega)(d\Omega/dt)$ ), the influence of friction ( $f$ ), and the heat

exchange ( $q$ ) as described in [6]:

$$\mathbf{U}_t + [\mathbf{F}(\mathbf{U})]_x = \mathbf{S}, \quad (6)$$

$$\mathbf{U} = \begin{Bmatrix} \rho \\ \rho u \\ \rho E \\ \rho x_r \\ \rho x_f \end{Bmatrix}, \quad \mathbf{F} = \begin{Bmatrix} \rho u \\ \rho u^2 + p \\ \rho u H \\ \rho u x_r \\ \rho u x_f \end{Bmatrix}, \quad (7)$$

$$\mathbf{S} = - \begin{Bmatrix} \rho u \alpha \\ \rho u^2 (\alpha + 2f/Du/|u|) \\ \rho u H \alpha - 4 \frac{q}{D} \\ \rho u x_r \alpha \\ \rho u x_f \alpha \end{Bmatrix}.$$

*Dynamic Reed Valve Model.* In order to predict the behavior of the machine also under different operating conditions, the code has to be able to perform a complete simulation of the system based only on geometric parameters. Inter alia, a flow model through the reed valves, has been developed, whereby the scheme is quite simple. The valves are placed on the inlet and outlet pipes, where the pressure difference generates a deflection, as a simply supported beam loaded with uniformly distributed load (Figure 2(a)).

Their deflection allows the gas to flow in or out.

For instance, let us consider the outlet valve (Figures 2(a) and 2(b)): the crankcase pressure pushes on one side of the valve, while the discharge pipe pressure acts in the opposite direction. As long as the discharge pipe pressure exceeds the pressure in the crankcase, the reed valve provides

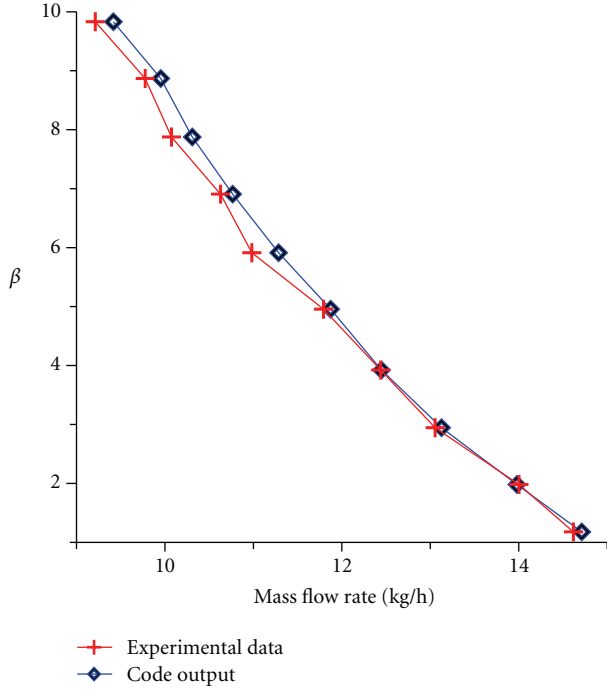


FIGURE 5: Comparison between numeric and experimental characteristic curves.

the sealing between the two volumes. When the crankcase pressure exceeds that in the discharge pipe, the valve deflects giving a certain cross-sectional flow area.

As mentioned above, the reed valve is seen as simply a supported beam loaded with uniformly distributed load, proportional to the total pressure difference between the crankcase and the pipe and to the width “ $d$ ” of the reed valve:

$$q = (p_{01} - p_{02}) \cdot d. \quad (8)$$

Therefore, the dynamic behavior of the reed valve can be simulated as a mass-spring-damper system, whose differential equation is

$$m \frac{d^2x}{dt^2} + \sigma \frac{dx}{dt} + kx = F, \quad (9)$$

where  $m$  is the reed petal mass;  $x$  is the instantaneous displacement;  $\sigma$  is the damping coefficient;  $k$  is the equivalent stiffness;  $F$  is the concentrate load which gives the same deflection of the distributed load.

By solving (9) and at the same time the thermodynamic equations of 1D flow, the deflection is calculated and so the instantaneous cross-section area to estimate the mass flow in the machine.

It is important to specify that, in the case of the considered compressor, the petal deflection is limited by two steel brackets which allow a maximum lift of 2 mm. The equivalent stiffness  $k$  can be estimated by imposing the same deflection between the two schemes in (Figure 3), being  $X_D$  the deflection caused by a concentrated load  $F = kx$ .

At last, the result is  $k = 48(EI/l^3)$ . In the absence of experimental data, a constant flow coefficient has been

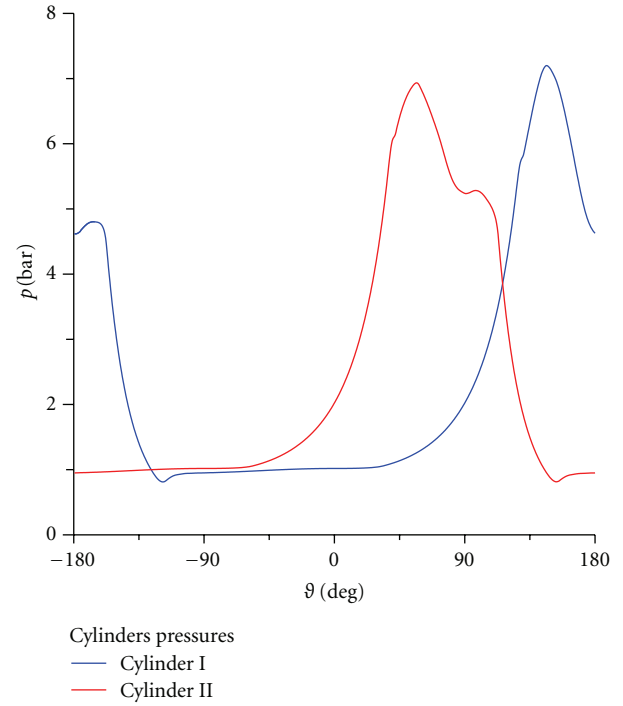


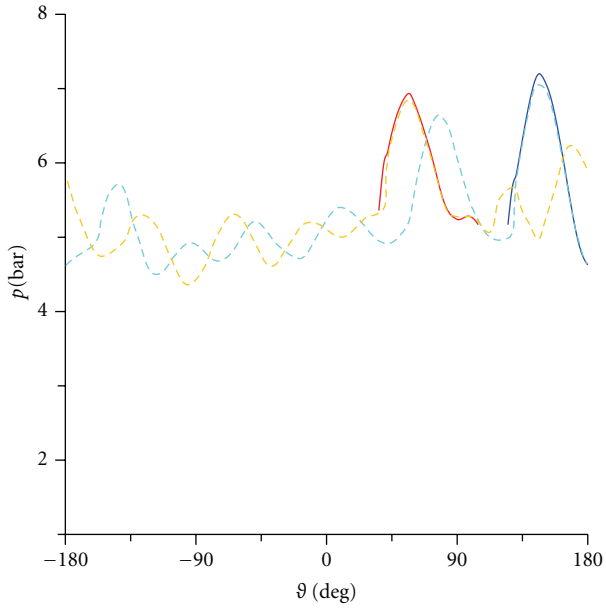
FIGURE 6: Pressure in the cylinders at  $\beta = 5$ .

used in all load conditions. The flux is considered isentropic until the restricted section, then isobaric downstream of the valve. The pressure in the throat is obtained by the mass flow balance between the cylinder and the adjacent pipe. A thorough validation of such a submodel is difficult to perform due to experimental complications, however, an indirect validation has been made by confronting the actual mass flow rate displaced by the compressor and the one determined by the code. The satisfying correspondence reached justifies the use of this submodel.

*Boundary Conditions.* The numerical simulation of the flow in a reciprocating engine duct is characterized by time-varying boundary conditions, in terms of both valve flow areas and thermodynamic properties inside the neighboring devices. In addition, a proper flow calculation at the end stations ensures a correct evaluation of the in-cylinder conditions during the gas exchange phases. The solution of end boundaries is performed by solving the typical compatibility equations along mach and path lines for a flow entering or exiting the duct.

A classical quasisteady approximation was assumed as to ensure the consistency with the flow through the intake and exhaust valves, which take place under either subsonic or sonic flow conditions.

*Input of the Code and Solutions.* To perform a simulation, the code requires in input a series of volumes, which represent the machine setup, their geometries, and initial conditions: each element is connected to other elements or to the external environment through links which can be constant



Discharge pressure  
 — Cyl. I during discharge      - - - Discharge pipe cyl. I  
 — Cyl. II during discharge      - - - Discharge pipe cyl. II

FIGURE 7: Pressure in the discharge pipes at  $\beta = 5$ .

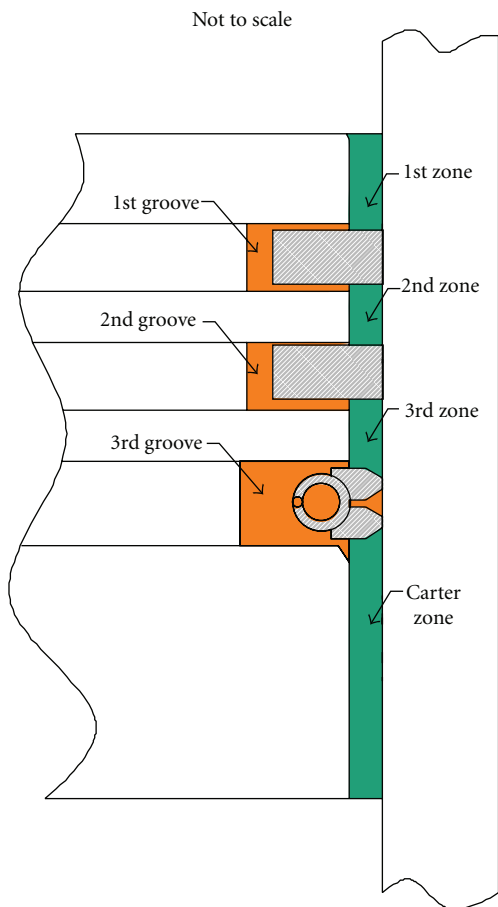


FIGURE 8: PRL system subdivision.

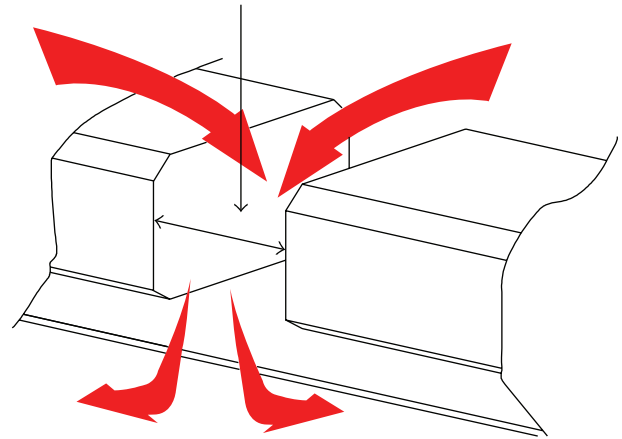


FIGURE 9: Ring gap.

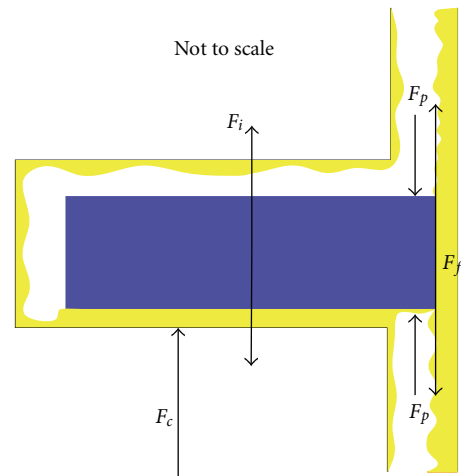


FIGURE 10: Axial forces on the segment.

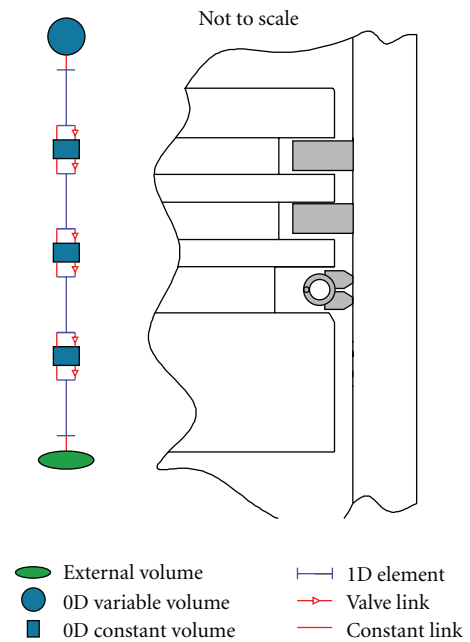


FIGURE 11: 0D-1D PRL scheme.

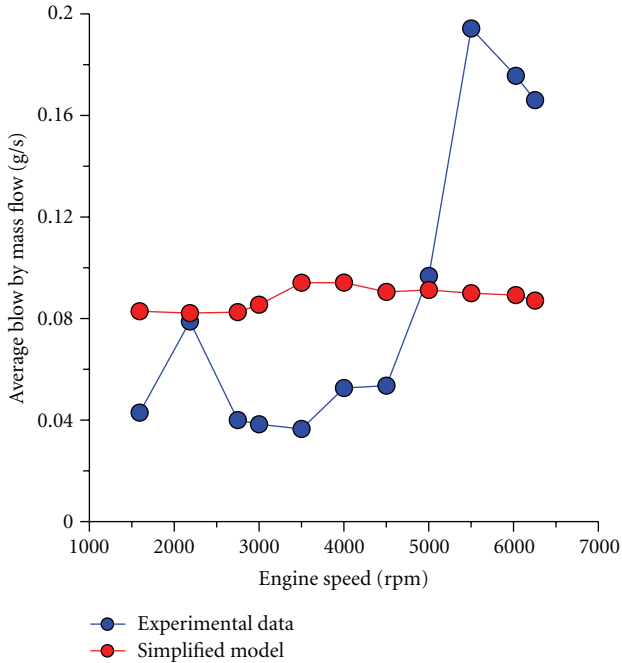


FIGURE 12: Experimental-simplified model Blow-by comparison.

cross section, ports, or valves (automatic or controlled). The boundary volumes are linked to sets which are at fixed thermodynamic conditions (e.g., ambient conditions). As results, the code provides, in arrays, both instantaneous and medium values of the thermodynamic parameters in each volume.

**3.1. 0D-1D Compressor Scheme and Comparison with Experimental Data.** Once the test-bed layout and the ducts geometries are known, it is possible to create a 0D-1D scheme (Figure 4) in input to the code: the inlet pipes are connected to the external environment set AA, while the duct SS is connected to a set in the same conditions of the holding tank TNK. On the discharge line, R1 and E2 converge in R2 bringing together the flows coming from the two cylinders.

A thermofluid-dynamic simulation of the 10 stationary tests in Table 1 was performed by the code, and in Figure 5 it is shown as a comparison between the numeric characteristic curve (blue line) and the experimental one (red line). The  $x$ -axis is associated to the mass flow rate (both measured and predicted) in the SR volume, the  $y$ -axis to the compression ratio ( $\beta = p_{TNK}/p_{AA}$ ).

The characteristic is predicted pretty well, the curves (Figure 5) seem to overlap with a slight divergence for  $\beta > 5$ , this problem is possibly due to the leaks of the valves and the piston rings in the real case.

In Figure 6, displayed are the predicted pressure diagrams in the two cylinders, and it shows that in the discharge phase of the cycle, pressure is highly variable because of the pressure waves that propagate along the discharge line as observed from the pressure curves of the discharge pipes (dashed lines, Figure 7).

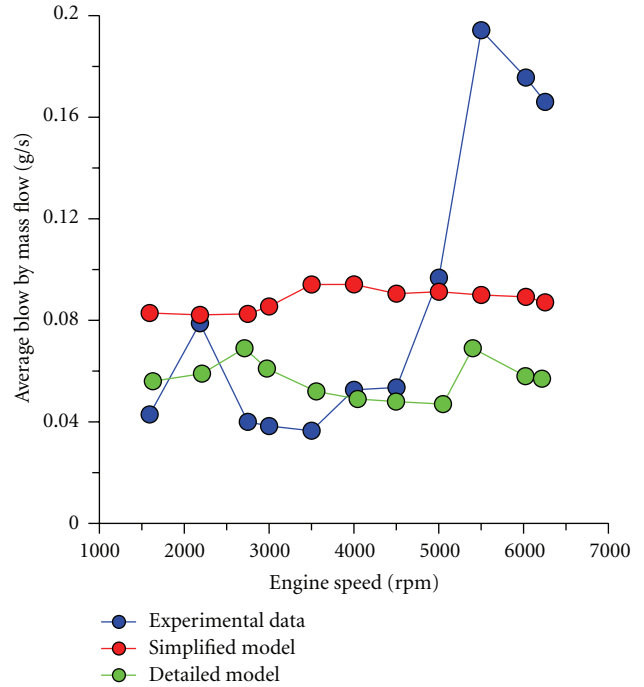


FIGURE 13: Blow-by models comparison.

As already mentioned, the compressor is a twin V-unit, and this means that the discharges of the cylinders take place with an interval of  $90^\circ$  (Figure 6).

It is clear that this phenomenon forces the compressor to reach pressures way higher (about 7 bar cycle II, about 7.2 bar cycle I) of the medium discharge pressure (about 5.3 bar in S1 and S2 ducts).

The liaison between the two cycles is clear, observing in Figure 7 how the discharge phase of cylinder II generates a pressure wave (peak at about  $80^\circ$  of light blue-dashed line) that affects the pressure during the discharge phase in cylinder I. This occurs due to the discharge happening in a volume at highly variable pressure. The same effects are more attenuated for cylinder II as there is more time since the closure of cylinder I discharge, which allows the pressure waves to dump.

This analysis shows how, by this modeling approach, it is possible to properly design the pipes upstream and downstream the compressor in order to reduce the pressure waves that, beside requiring more power from the electric engine, decrease the mass flow rate, and cause an increase in the noise during operation.

#### 4. Blow-By

In order to improve the accuracy of the modeling approach, it was considered to weigh the gas leakage due to an imperfect sealing which took place between the piston and cylinder, this phenomenon in literature is termed "blow-by" [26].

The piston sealing system consists essentially of segments, also known as piston rings; these are open metal flattened rings, and they have two main functions: to provide

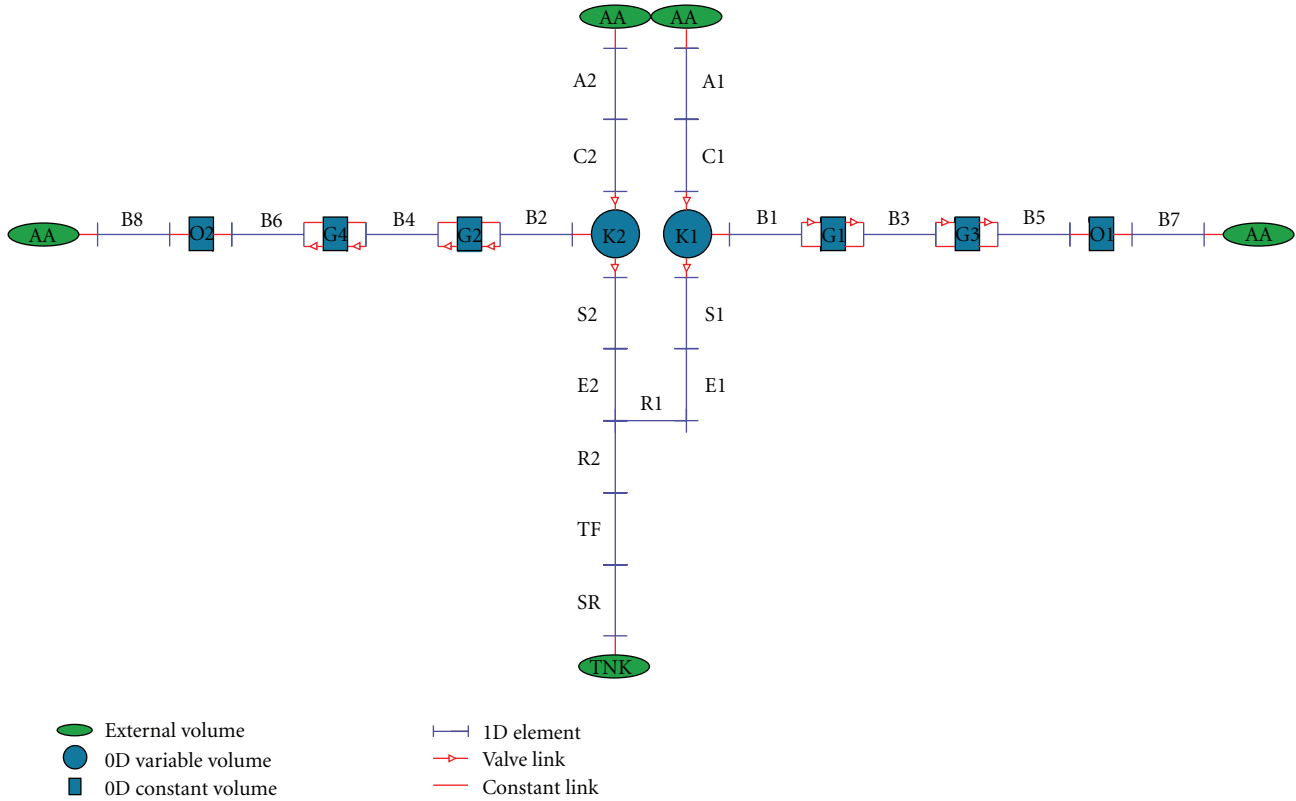


FIGURE 14: Final 0D-1D scheme for the compressor with blow-by volumes.

a certain tightness in the compression chamber, minimizing energy losses to regulate and level the lubricant distribution on the cylinder liner, minimizing both consumption and friction losses. The Piston-Ring-Liner system (PRL) can be split into different volumes identified by their relative position beside the sealing segments: the first zone, near the head of the piston; the second and third zones, located under the two rings; the crankcase zone, placed between the OCR and the crankcase; the first, second grooves and the OCR groove, which are the volumes placed behind the segments (Figure 8).

To report this subdivision within a scheme that can be interpreted by the code used, equivalent volumes and capacities are identified and they have been implemented within the machine framework. As already mentioned, two kinds of volume can be identified in the PRL system:

- (i) the “zones” that are the annular pipes identified by the clearance between the piston diameter and the cylinder shell,
- (ii) the “grooves” that are the volumes identified by the distance between the inner surface of a ring and the bottom of the piston groove.

Please note that in this work secondary movements of the piston are not taken into account for the identification of the flow sections, which cause a section variance moment by moment during a cycle. Due to the “zones” having an annular section, it was identified in having an equivalent

diameter and a corrective coefficient of the friction factor  $f$ , so it was possible to match the pressure drops in the pipe with the real pressure drop [29].

If the section is not circular, the equivalent hydraulic diameter has to be used; this new diameter is obtained by the equation:

$$D_{eq} = \frac{4 \cdot A}{P}. \quad (10)$$

So, for annular section pipes [29]:

$$D_{eq} = D_e - D_i. \quad (11)$$

For annular section pipes, the correction coefficient of the friction factor may be considered [29],

$$c_f = \frac{f_{annular}}{f_{circular}} = 1.05. \quad (12)$$

Regarding the “ring gap,” there are very complex phenomena taking place, as flows from two zones and from the inside of the groove cross themselves, as well as the relative shift of the segment that can cause an accumulation of lubricant in the hole.

Since the purpose of this work is not the particular analysis of the flow through the gap, a simplified model was chosen: in Figure 9, illustrated is the gap geometry and the gas flow between one zone to another through the interspaces.

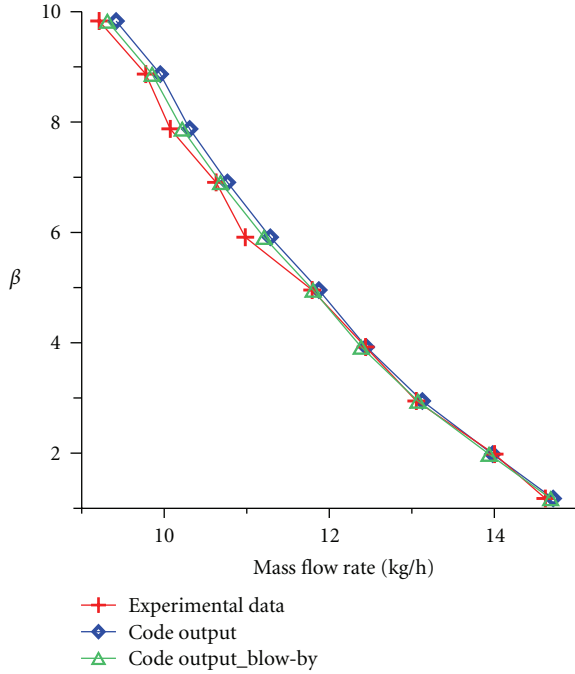


FIGURE 15: Characteristic curves comparison.

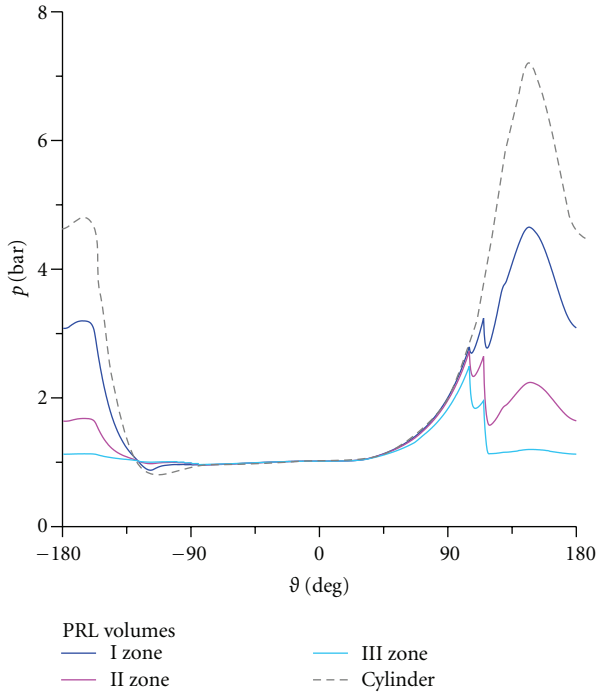


FIGURE 16: Pressure analysis in PRL volumes,  $\beta = 5$ , stable model.

The pressure inside the gap is assumed equal to the pressure inside the groove, while the gas flow that passes through the gap can be expressed by the isentropic flow equations through an orifice, and so it was decided to include this element in the geometric scheme as a port between the groove and the linked zones [30]. The flow through the

gap sets the pressure difference which is established between different zones, and therefore, also affects the ring dynamic.

**4.1. Ring Dynamics inside the Grooves.** The gas flow is closely related to the rings dynamic, it works like a port that opens only when it is separated from both walls of the groove. It is a prohibitive work predicting the opening without any experimental feedback, just thinking that three components of a segment with relative displacement can be identified: axial, radial, and angular. Each one is caused by a system of forces which vary moment by moment. This paper, with the limits of a one-dimensional model, has been concentrated on the axial displacement. Axial forces acting on a segment during a cycle are identified as follows (Figure 10):

- (i)  $F_p$ : gas and oil pressure above and below the segment;
- (ii)  $F_f$ : friction between cylinder liner and piston;
- (iii)  $F_i$ : inertia due to the piston alternative motion;
- (iv)  $F_c$ : contact force between segment side and groove.

These forces resultant cause the relative axial displacement of the segment inside the groove [31].

Starting from the wider literature about “blow-by” in internal combustion engines, to find an analogy in the rings dynamic, it is possible to hypothesize the two displacement models for the rings:

- (i) Stable Model: all segments displacement follows the oscillating masses inertia force trend;
- (ii) Flutter Model: forces resultant during compression final phase change sign several times, causing irregular oscillations of the segment inside the groove.

These two models are used to hypothesize and impose the shift law of the “valve ports” described in the subsequent paragraph.

**4.2. PRL System Summery and 0D-1D Schemes.** At this point, a synthesis of the PRL system was reached, consisting of an ensemble of zero and one-dimensional volumes. Zones, according to the assumptions made previously, are annular section pipes, to represent as good as possible the grooves it was chosen, instead, a zero-dimensional capacity, linked to the adjacent volumes through two different kinds of section:

- (i) a variable section due to the segment axial displacement, which as said before, can be represented by some “controlled valve” port type that has to be set with the more appropriated shift law;
- (ii) a constant section port which represents not only the flow through the ring gap, but also the poor seal between shell and segments, due to an uneven surface.

In addition, to take into account dissipative phenomena that happens in the flow through the gap, a fixed flow factor is imposed to the constant section link.

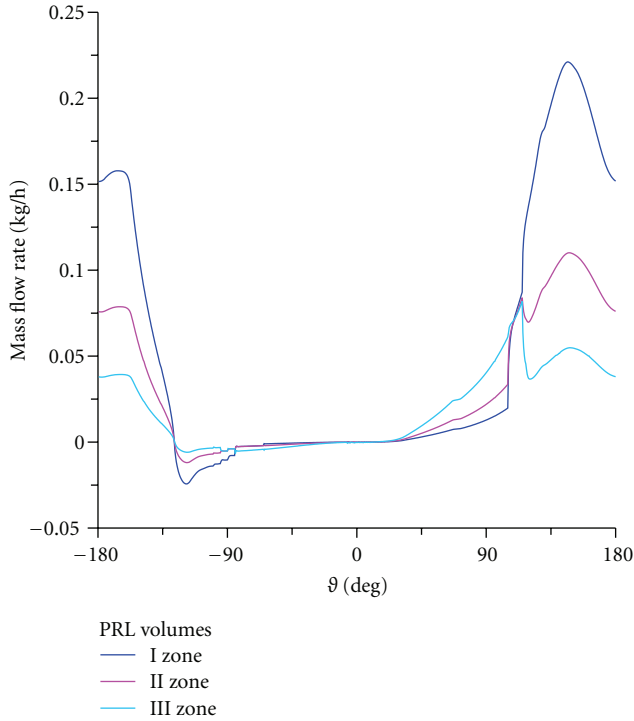
FIGURE 17: blow-by flow rate in PRL volumes,  $\beta = 5$ , stable model.

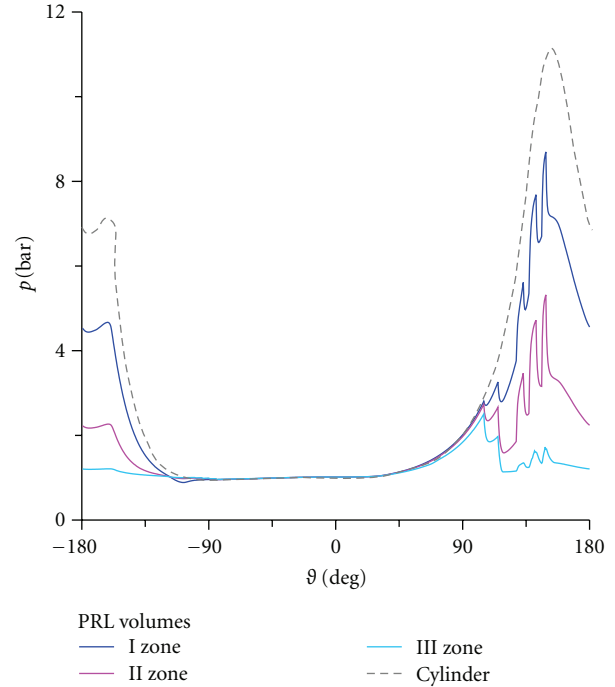
TABLE 2: Features of the analyzed engine.

Engine type	Twin 4T
Cylinder number	2
Displacement	908 cm <sup>3</sup>
Stroke/Bore/Conn. Rod length	(86/82/133.55) mm
Compression ratio	11

**4.3. PRL Scheme Validation.** To validate the PRL scheme of the “blow-by” just described, several schemes have been tested for a 4-stroke two-cylinder engine (Table 2) on which experimental data was reported in relation to the “blow-by” flow rate. First of all, the PRL circuit of “blow-by” was schemed by a single 1D pipe with a circular section, its diameter was considered to be the average of the quadratic diameters to receive the experimental flow rate of “blow-by.” The comparison between the experimental flow rate and the data taken thanks to the simplified scheme characterized by a single 1D pipe and constant diameter equal to the medium quadratic is shown in Figure 12.

From the diagram in Figure 12, it is possible to notice how the model gives, obviously, an average value of the “blow-by” flow rate coherent enough with experimental data, but not so indicative for each single loading rate.

This is proof that the rings dynamic role is essential to predict the “blow-by” flow rate. So, it was realized a detailed PRL system scheme according to the logic described for the compressor in the previous paragraph and illustrated in Figure 11. This scheme has been realized by having data of the geometry of the piston, cylinder, piston rings, and the hot coupling between cylinder and piston.

FIGURE 18: Pressure in PRL volumes,  $\beta = 8$ , flutter model.

The rings motion in their own grooves was imposed, according to the stable model, by two symmetric shift laws interpolated on 720 degrees of the crank angle, based on the above-mentioned stable model: the piston rings motion have been imposed according to experimental measurement reported in [26].

The blow-by mass flow rate obtained thanks to the PRL scheme in relation of rpm is shown in Figure 13 (red line); although it seems that the detailed scheme does not offer better results than the simplified one, note that the input of the first is only the PRL geometry, while the simplified scheme needs experimental data.

By comparing (in Figure 13) the (red line) with the experimental data (blue line), it can be noted that the flow rate is well predicted till 4500 rpm; over this rpm probably the flutter phenomenon intervenes [26], which should influence seriously the “blow-by” flow rate. It is in the authors intention to realize in the next work a piston rings dynamic model, so it can be verified if the flow rate rise over 4500 rpm is due to flutter phenomenon.

## 5. Blow-By Model for a Compressor

After the analysis conducted on the alternative internal combustion engine, the detailed PRL scheme (Figure 11) with imposed piston rings dynamic, adherent to the stable model, was considered sufficiently predictive to conduct some analysis on the “blow-by” phenomenon effects on the compressor characteristic curve. Here, in Figure 14 is shown the complete 0D-1D scheme used by the code to simulate the normal compressor displacement (to the TNK set) and the leakage through the ring pack system (to lateral AA sets).

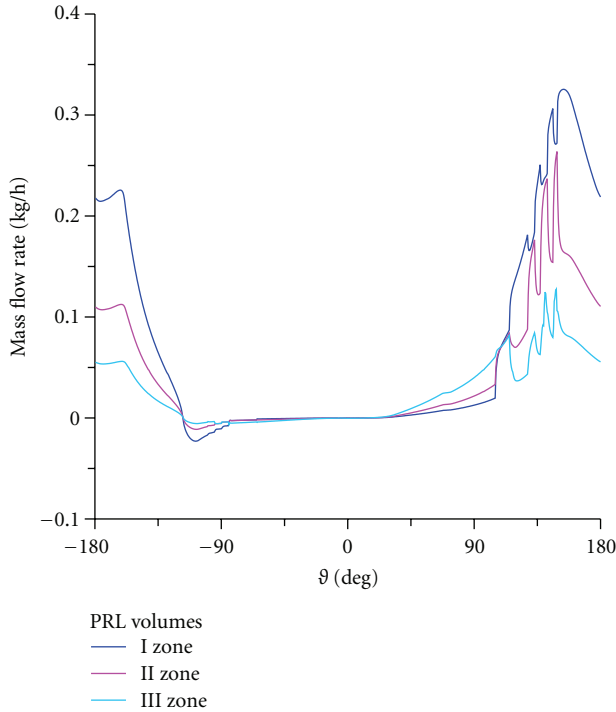


FIGURE 19: Mass flow rate in PRL volumes,  $\beta = 8$ , flutter model.

In Figure 15, the obtained characteristic considering the effect of the “blow-by” in the compressor (light green line) is compared with the characteristic previously obtained without introducing the “blow-by” scheme. The results show that the curves are practically coincident till  $\beta = 5$ , which means that the phenomenon is practically irrelevant when the compressor works with low compression ratios. For higher values, instead, the characteristic obtained simulating the “blow-by” phenomenon in the compressor maintains a slope nearly coincidental with the experimental curve, better explaining the real machine behavior.

In Figure 16, the pressure trends in the cylinder and in the zones of the PRL system, called “grooves” that is in the piston rings accommodation, are reported. In Figure 11, the instant pressure in these zones follows the inside cylinder pressure trend, reaching, however, peaks necessarily smaller.

As mentioned previously, this is due to a strongly influenced flow rates as a result of the ring gap, which in spite of the strong losses, realizes a continuous link between the compression chamber and the zones between piston and cylinder. As we move from the cylinder to the crankcase, the pressure curves tend to assume the value of ambient pressure, which is the condition (assumed uniform) in the crankcase. In coincidence of the segments displacement (approx. 112 degree, in Figure 16), there is a pressure drop due to the opening of superior and inferior channels of each groove, generating a flow rate peak (Figure 17). Compression occurs during the opening of the passage through the piston rings, with a displacement toward the segment upper edge.

In Figure 17, it is also observed that there are some cycle phases where there is a reverse “blow-by” (about 135 degree).

In particular, at the end of the expansion phase, when the first zone is at a pressure higher than the compression chamber, part of the gas reflows till the pressure difference vanishes. A similar argument is also valid for the intermediate zones, which along whole the intake phase are affected by a reversal of the “blow-by” flow even if it is minimum.

From Figure 16, it also observed that there are large intervals where, between the cylinder and the various zones and between themselves, wide  $\Delta p$  are generated, which could generate forces opposite to inertia force on the segment, leading to the flutter phenomenon.

Now, it is possible to perform an interesting analysis of the parameters in PRL volumes in case of ring flutter. A series of fluctuations has been hypothesized for the first ring during the pressure raise in the case of  $\beta = 8$ . In Figure 18, where the fluctuations take place, a pressure drop can be observed, especially in the first two zones.

As can be seen in Figure 19, the blow-by mass flow rate has no more this peak in one single point, but there are several peaks which take place in the exact same time that the ring flutters. This phenomenon shows that the blow-by is highly influenced by the ring dynamics, and in particular way if the ring is not stable during the cycle.

## 6. Conclusions

This work has been developed to improve the accuracy of the simulation of the CFD phenomenon in the volumetric machines. A 1D procedure is proposed and validated with the experimental data taken from a volumetric alternative compressor. In addition, a PRL system scheme was implemented for the “blow-by” simulation. This scheme, based on the “stable” dynamic imposed to the segments, has enabled an improvement in the characteristic reproduction of the compressor, besides; it was possible to carry out a first CFD analysis inside the cavity between the cylinder and piston. In light of the encouraging results obtained, it is considered appropriate that a development of a predictive dynamic model of the segment displacement to be implemented on the 0D-1D simulation software, so it will improve the model prediction in all operation conditions.

## Acronyms

- 0D: Zero-dimensional
- 1D: One-dimensional
- TVD: Total variation diminishing
- PRL: Volumes between piston ring and liner
- OCR: Oil control ring.

## Nomenclature

### Latin

- $p_{amb}$ : Ambient pressure
- $T_{amb}$ : Ambient temperature
- $p_{tnk}$ : Tank pressure
- $T_{oil}$ : Oil temperature
- $p_{01}$ : In-cylinder pressure on reed valve

$p_{02}$ : Outlet pressure on reed valve  
 $p_{\text{TNK}}$ : Tank pressure  
 $p_{\text{AA}}$ : Ambient pressure  
 $V_3$ : Cylinder top clearance  
 $V$ : Displacement volume  
 $D_{\text{eq}}$ : Equivalent hydraulic diameter  
 $f_{\text{annular}}$ : Annular cross-section friction factor  
 $f_{\text{circular}}$ : Circular cross-section friction factor.

### Greek

$\beta$ : Compression ratio  
 $\beta_{\text{MAX}}$ : Theoretical maximum compression ratio.

### References

- [1] S. A. Tassou and T. Q. Qureshi, "Comparative performance evaluation of positive displacement compressors in variable-speed refrigeration applications," *International Journal of Refrigeration*, vol. 21, no. 1, pp. 29–41, 1998.
- [2] E. Winandy, C. Saavedra O, and J. Lebrun, "Simplified modelling of an open-type reciprocating compressor," *International Journal of Thermal Sciences*, vol. 41, no. 2, pp. 183–192, 2002.
- [3] C. O. R. Negrão, R. H. Erthal, D. E. V. Andrade, and L. W. D. Silva, "A semi-empirical model for the unsteady-state simulation of reciprocating compressors for household refrigeration applications," *Applied Thermal Engineering*, vol. 31, no. 6-7, pp. 1114–1124, 2011.
- [4] C. D. Pérez-Segarra, J. Rigola, and A. Oliva, "Modeling and numerical simulation of the thermal and fluid dynamic behavior of hermetic reciprocating compressors—part 1: theoretical basis," *HVAC and R Research*, vol. 9, no. 2, pp. 215–235, 2003.
- [5] C. D. Pérez-Segarra, J. Rigola, and A. Olivaa, "Modeling and numerical simulation of the thermal and fluid dynamic behavior of hermetic reciprocating compressors-part 2: experimental investigation," *HVAC&R Research*, vol. 9, no. 2, pp. 237–249, 2003.
- [6] F. Bozza, M. Manna, and A. Pascarelli, "Un approccio misto 0-D/1-D per la simulazione di M.C.I. a 2 tempi," in *Atti del 49° Congresso Nazionale ATI*, vol. 2, pp. 1835–1847, SGE-Padova, Settembre 1994.
- [7] M. N. Srinivas and C. Padmanabhan, "Computationally efficient model for refrigeration compressor gas dynamics," *International Journal of Refrigeration*, vol. 25, no. 8, pp. 1083–1092, 2002.
- [8] D. Woollatt, "Factors affecting reciprocating compressor performance," *Hydrocarbon Processing*, vol. 72, no. 6, pp. 657–65, 1993.
- [9] M. Manna, *A three dimensional high resolution compressible flow solver*, Ph.D. thesis, Catholic University of Leuven—Von Karman Institute for Fluid Dynamics, 1992, also in Technical Note 180, VKI, 1992.
- [10] F. Bozza, R. Tuccillo, and D. deFalco, "A two-stroke engine model based on advanced simulation of fundamental processes," in *Proceedings of the International Off-Highway & Powerplant Congress & Exposition*, SAE Paper no. 952139, Milwaukee, Wis, USA.
- [11] Society of Automotive Engineers, *Design and Emissions of Small Two- and Four-Stroke Engines*, SAE SP-1112, Society of Automotive Engineers, 1995.
- [12] F. Bozza, M. C. Cameretti, and R. Tuccillo, "Numerical simulation of in-cylinder processes and duct flow in a light-duty diesel engine," in *Proceedings of the 4th International Symposium on Small Diesel Engines*, pp. 24–25, Varsavia, Poland, pubblicato su *Journal of Polish Cimac*, vol. 2, no. 1, pp. 51–66, 1996.
- [13] F. Bozza, A. Senatore, R. Tuccillo, and A. Gimelli, "Caratterizzazione sperimentale e teorica del funzionamento di un motore diesel di concezione avanzata," *Rivista—ATA—Associazione Tecnica dell'Automobile*, pp. 117–129, 1997.
- [14] F. Bozza, M. C. Cameretti, A. Senatore, and R. Tuccillo, "Experimental investigation and numerical modelling of an advanced turbocharged D.I. diesel engine," in *Proceedings of the SAE International Congress & Exhibition*, SAE Paper no. 970057, pp. 19–31, February 1997, pubblicato anche sul volume "Engine Modeling", SAE SP-1255, 1997.
- [15] F. Bozza, M. C. Cameretti, A. Senatore, and R. Tuccillo, "A flow and a combustion model for NOx emission evaluation in a turbocharged diesel engine," in *Proceedings of the 3rd International Conference on Internal Combustion Engines: Experiments and Modeling (ICE '97)*, pp. 153–162, Capri, Italy, Settembre 1997.
- [16] F. Bozza, M. C. Cameretti, and R. Tuccillo, "Numerical simulation of transient behaviour of an EGR equipped turbocharged engine," in *Proceedings of the 4th International Conference on Internal Combustion Engines: Experiments and Modeling (ICE '99)*, pp. 313–320, Capri, Italy, Settembre 1999.
- [17] F. Bozza, A. Senatore, and R. Tuccillo, "Integrated numerical-experimental method for the analysis of in-cylinder processes in an EGR equipped diesel engine," in *Proceedings of the Fall Technical Conference of the ASME Internal Combustion Engine Division*, pp. 16–20, Ann Arbor, Mich, USA, Ottobre 1999.
- [18] F. Bozza, A. Gimelli, and R. Tuccillo, "The control of a VVA-equipped SI engine operation by means of 1D simulation and mathematical optimization," in *Proceedings of the SAE International Congress & Exhibition*, vol. SP-1692 of SAE Paper no. 2002-01-1107, Detroit, Mich, USA, 2002, Published also in *SAE Transactions, Journal of Engines*, vol. 111, pp. 1790–1801, 2003.
- [19] F. Bozza and A. Gimelli, "A comprehensive 1D model for the simulation of a small-size two-stroke SI engine," in *Proceedings of the SAE World Congress & Exhibition on Modeling of SI and Diesel Engines*, vol. SP-1830 of SAE Paper no. 2004-01-0999, pp. 165–177, March 2004, Published also in the on the *SAE Transactions, Journal of Engines*, section 3, July 2005.
- [20] F. Bozza, A. Gimelli, V. Pianese, S. Martino, and R. Curion, "An acoustic design procedure for intake systems: 1D analysis and experimental validation," in *Proceedings of the SAE World Congress & Exhibition on Modeling of SI and Diesel Engines*, vol. SP-1867, pp. 139–147, March 2004, Published also in *Transactions Journal of Passenger Cars*, vol. .6, pp. 172–180, 2005.
- [21] D. Siano, F. E. Corcione, F. Bozza, A. Gimelli, and S. Manelli, "Characterization of the noise emitted by a single cylinder diesel engine: experimental activities and 1D simulation," in *Proceedings of the SAE Noise and Vibration Conference and Exhibition*, SAE Paper no. 2005-01-2483, Grand Traverse, Mich, USA, May 2005.
- [22] F. Bozza, A. Gimelli, R. Piazzesi, F. Fortunato, V. Pianese, and D. Siano, "The prediction of the performance and gasdynamic noise emitted by a medium-size spark-ignition engine by means of 1D and 3D analyses," in *Proceedings of the SAE World Congress & Exhibition on Modeling of SI and Diesel Engines*, vol.

- SP-2079 of SAE Paper no. 2007-01-0380, Detroit, Mich, USA, April 2007.
- [23] F. Bozza, A. Gimelli, L. Strazzullo, E. Torella, and C. Cascone, "Steady-state and transient operation simulation of a, "downsized" turbocharged SI engine," in *Proceedings of the SAE World Congress & Exhibition on Modeling of SI and Diesel Engines*, vol. SP-2079 of SAE Paper no. 2007-01-0381, Detroit, Mich, USA, April 2007.
- [24] F. Bozza, A. Gimelli, L. Andreassi, V. Rocco, and R. Scarcelli, "1D-3D analysis of the scavenging and combustion process in a gasoline and natural-gas fuelled two-stroke engine," in *Proceedings of the SAE World Congress & Exhibition on Modeling of SI and Diesel Engines*, SAE Paper no. 2008-01-1087, p. 303, Detroit, Mich, USA, April 2008, On SP-2156 (Modeling of SI and Diesel Engines, 2008), *Journal SAE Technical Paper*, pp. 303-316.
- [25] F. Bozza and A. Gimelli, "Unsteady 1D simulation of a turbocharger compressor," in *Proceedings of the SAE World Congress & Exhibition on Modeling of SI and Diesel Engines*, SAE Paper no. 2009-01-0308, pp. 67-76, Detroit, Mich, USA, April 2009, Also in *SAE International Journal of Engines*, vol. 2, pp. 189-198, October 2009.
- [26] T. Tian, *Modeling the performance of the piston ring-pack in internal combustion engines*, Ph.D. thesis, Massachusetts Institute of Technology, 1997.
- [27] O. Pennacchia, *Studio di compressori alternativi dotati di manovellismo non convenzionale*, Tesi di laurea in Ingegneria Meccanica, Università di Napoli Federico II, 2003.
- [28] A. Harten, "On a class of high resolution total variation stable finite difference schemes," *Journal of Computational Physics*, vol. 21, pp. 21-23, 1984.
- [29] D. S. Miller, *Internal Flow Systems*, 1990.
- [30] L. Liu, *Modeling the performance of the piston ring pack with consideration of non-axisymmetric characteristics of the power cylinder system in IC Engines*, Ph.D. thesis, Massachusetts Institute of Technology, 2005.
- [31] K. Jia, *A coupled model for ring dynamics, gas flow and oil flow through the ring grooves in IC engines*, Ph.D. thesis, Massachusetts Institute of Technology, 2009.